UiT The Arctic University of Norway

Faculty of Engineering Science and Technology

An applied investigation of viscosity–density fluid sensors based on torsional resonators

-

Daniel Brunner

A dissertation for the degree of Philosophiae Doctor, September 2020

An applied investigation of viscosity–density fluid sensors based on torsional resonators

By

Daniel Brunner

Thesis submitted in fulfilment of
the requirements for the degree of
PHILOSOPHIAE DOCTOR

(PhD)

Faculty of Engineering Science and Technology

UiT The Arctic University of Norway
N-9037 Tromsø

Norway
www.uit.no

ISBN: 978-82-7823-221-7

Abstract

Real-time viscosity and density measurements give insight into the status of many chemical and biochemical processes and allow for automated controls. In many applications, sensors that enable the real-time measurements of fluid properties use resonant elements. Such sensors measure induced changes in the element's resonance frequency and damping that can be related to the fluid properties. These sensors have been widely researched, though they are not yet commonly used in industrial processes.

This study investigates two resonant elements to measure the viscosity and density of Newtonian fluids. The first is a probe-style viscosity-density sensor, and the second is a non-intrusive tubular viscosity sensor. These two sensors were investigated using analytical, numerical, and experimental methods. In the analytical method, the sensors' resonance frequencies and bandwidths were predicted based on reduced-order models for both structure and fluid. In the numerical method, the interaction of the resonant element with the fluid was investigated by means of computational fluid dynamics (CFD). Experiments were conducted for validation, to evaluate the sensors' capabilities, and understand cross-sensitivity effects between viscosity and density.

The reduced-order (analytical) method was used to model the resonant elements of the sensors as mass-spring systems, describing their interaction with the fluid. For the probe style viscosity-density sensor, the resonant element was comprised of a two-mass and three-spring system. The tubular viscosity sensor was analyzed by means of a modal analysis by reducing it to a single mass-spring system, where only the first torsional mode was considered. The main advantage of the reduced-order model was that it provided insight into the working principle of the sensors without using complicated and computationally expensive numerical models.

CFD was used to understand the fluid behavior around the resonant element of the probe-style viscosity density sensor. The flow field was solved using CFD because the probe style viscosity-density sensor has a complex geometry, i.e., cylindrical tip with four radial fins where the flow phenomenon is too complex to be described analytically. The solution was validated for independence of discretization, i.e., mesh and numerical methods (finite element method via COMSOL® and finite volume method via ANSYS® CFX). Different boundary conditions, such as by a moving wall and changing the frame of reference, were used to generate similar effects. The resulting fluid forces from the CFD solution were coupled with the reduced-order (analytical) structural model to compute the change in resonance frequency and bandwidth.

A series of experiments were conducted under a range of well-defined conditions to validate the output of the models and test both sensors, namely the probe-style viscosity-density sensor and tubular viscosity sensor. For each condition, the experimentally measured bandwidth and resonance frequency were compared to the predictions of the models. Results from the experiments and models were found to be in good agreement. This led to successfully accounting for cross-sensitivities between viscosity, density, and temperature.

This work successfully modeled and validated the two different torsional resonant element sensors, namely the probe-style viscosity-density sensor and the tubular viscosity sensor against experiments. There are two key output parameters, i.e., resonance frequency and bandwidth. Using these parameters, it is possible to predict fluid viscosity and density. Overall, this work demonstrates the potential of numerical modeling for the development of torsional resonance sensors. These findings directly affect the development of the future generation of fluid viscosity and density sensors.

Keywords: viscosity sensor, density sensor, computational fluid dynamics, fluid–structure interaction, oscillation, resonator, reduced order modelling

Acknowledgments

This study was conducted at the Institute of Computational Physics at the ZHAW in Winterthur from 2017 to 2020 in collaboration with the Arctic University of Norway. This applied research project was done in collaboration with the Rheonics GmbH company. I extend my heartfelt gratitude to my supervisor Dr. Hassan Abbas Khawaja of the Arctic University of Norway who supported me with my writing, planning, and simulations.

I would also like to thank my family members, especially my wife Ashley, who supported me patiently throughout this journey. Dr. Gernot Boiger made this PhD possible by his unwavering support all the way. I thank Dr. Joe Goodbread for supervising all my experimental and design-related work and supporting the designing and building process of the new sensor. The interesting and insightful discussions we had on numerous subjects were very helpful. I am also grateful to Dr. Klaus Häusler, Dr. Sunil Kumar, Dr. Patrick Vogler, and Dr. Vijoya Sa for their support. Last, but not the least, I appreciate my colleagues at the Institute of Computational Physics at ZHAW for their insightful and enlightening discussions over coffee.

Table of Contents

Nomenclature x
List of Appended papers xii
1 Introduction 1
1.1 Research motivation 3
1.2 Problem statement 3
1.3 Research questions 4
1.4 Research objectives 4
2 Research Methodology 5
2.1 Analytical structural models 5
2.1.1 Single-degree-of-freedom system 5
2.1.2 System with multiple-degrees-of-freedom 8
2.1.3 Continuous resonator 10
2.2 Analytical and numerical fluid models 12
2.2.1 Fluid forces on a resonating body 12
2.2.2 In-plane oscillating plate 14
2.2.3 Torsional oscillating tube 15
2.2.4 Computational fluid dynamics 17
2.3 Experiments 20
2.3.1 Density measurement 20
2.3.2 Viscosity measurement 20
2.3.3 Identifying cross sensitivities 21
3 Results and Discussions 23
3.1 Paper I 23
3.2 Paper 2 26
3.3 Paper 3 30
3.4 Paper 4 33
3.5 Summary 37
4 Research Contributions and Future Work 39
4.1 Research contributions 39
4.2 Suggestions for future work 40
Works cited 41
Appendix 45
Paper I 47
Paper II 49
Paper III 51
Paper IV 53

Nomenclature

Symbols

A	rad	Angular deflection amplitude
c	Nm/rad	Torsional spring constant
$\boldsymbol{C}$	Nm/rad	Torsional spring matrix
c_i	$-$	Constants, where $_i$ is an integer
d	Nm/s	Damping factor
d_0	Nm/s	Damping factor, intrinsic damping
d_f	Nm/s	Damping factor, fluid damping
$\boldsymbol{D}$	Nm/s	Damping factor matrix
$\vec{e}_i$	$-$	Unity vector of torsional axis
f_0	Hz	Resonance frequency
$f_{0,air}$	Hz	Resonance frequency in air
F	Nm	Forcing term
$\hat{F}$	Nm	Forcing term amplitude
F_N	$1/s^2$	Normalized force term
G	Pa	Shear modulus
I_p	m^4	2nd moment of area
i^+	$-$	Parameter to describe the fluid density
J	kgm^2	2nd inertial mass
$\boldsymbol{J}$	kgm^2	2nd inertial mass matrix
J_f	kgm^2	2nd moment of inertia of fluid
J_0	kgm^2	2nd moment of inertia of the resonator
k	$-$	Wave number
L	m	Length
$M_{v,t}$	Nm	Viscosity-induced torque
$M_{p,t}$	Nm	Pressure-induced torque
M_v	Nm	Viscosity-induced torque amplitude
M_p	Nm	Pressure -induced torque amplitude
p	Pa	Pressure
r	m	Radial coordinate
$\vec{r}$	m	Distance vector from torsional axis ($\vec{e}_i$)
R	m	Radius
t	s	Time
u_x	m/s	Velocity in x-direction
u_α	rad/s	Azimuthal velocity
$\vec{u}$	m/s	Velocity field
x	m	x-location
X	$-$	Transfer function
z	m	z-coordinate

Greek symbols

$\Im$	$-$	Operator for the imaginary part of a complex number
$\Re$	$-$	Operator for the real part of a complex number
Γ	Hz	Bandwidth
Γ^+	kg/m^3	Parameter to describe the viscosity-density product
λ	$-$	Eigenvalue
τ_d	s	Logarithmic decrement
δ	m	Boundary-layer thickness
φ	rad	Angular deflection
$\hat{\varphi}$	rad	Angular deflection amplitude
φ_0	rad	Angular deflection at time $t = 0\ s$
φ_s	rad	Angular deflection, quasi-steady-state solution
$\hat{\vec{\varphi}}_m$	rad	Angular deflection vector
Ψ	rad	Angular deflection as a function of time and space
$\widehat{\Psi}$	rad	Modal function
ρ	kg/m^3	Fluid density
ρ_s	kg/m^3	Density of the resonator
η	Pas	Dynamic viscosity
ω	rad/s	Angular frequency
ω_0	rad/s	Angular resonance frequency
$\omega_{0,m}$	rad/s	Angular resonance frequency
$d\Omega_r$	m^2	Boundary of the resonator
$\vec{\Omega}$	rad	Rotation vector of the domain

Abbreviations

CFD	Computational Fluid Dynamics
ICP	Institute of Computational Physics
ZHAW	Zurich University of Applied Sciences
RQ	Research question
NIST	National Institute of Standards and Technology

List of Appended papers

Paper I J. Goodbread, D. Brunner, K. Häusler, S. Kumar, H, Khawaja, Viscosity–Density Sensor Based on Torsional Vibrations, Manuscript ready, 2020.

Paper II D. Brunner, J. Goodbread, K. Häusler, S. Kumar, G. Boiger, H. Khawaja, Modelling a Viscosity-Density Sensor Based on Small Amplitude Torsional Vibrations, Manuscript ready, 2020.

Paper III D. Brunner, H. Khawaja, M. Moatamedi, G. Boiger, CFD Modelling of Pressure and Shear Rate in Torsionally Vibrating Structures Using ANSYS CFX and COMSOL Multiphysics, International Journal Multiphysics, 2018, 12 (4), 349–358.

Paper IV D. Brunner, J. Goodbread, K. Häusler, S. Kumar, G. Boiger, H. Khawaja, Analysis of a Tubular Torsionally Resonating Viscosity-Density Sensor, MDPI Sensors, 2020, 20 (11), 3036. https://doi.org/10.3390/s20113036.

1 Introduction

In most chemical and biochemical processes, it is important to measure fluid properties, such as viscosity and density, because these properties can be used as indicators of the fluid's composition. Therefore, real-time monitoring of a fluid's viscosity and density enables better quality control of various processes. Traditional rheological laboratory instruments are large and delicate, and they measure by sampling. In comparison, resonant sensors are more compact, robust, and capable of being integrated into process lines. The working principle of a resonant sensor is that a resonating element is brought into contact with a fluid. The fluid changes the resonant element's resonance frequency and damps its oscillation. Both the shift in the resonance frequency and damping can be measured and related to the fluid's properties.

Most studies on resonator-based viscosity sensors focus on microelectromechanical systems. Jakoby et al. [1] reviewed literature on these miniaturized sensors and discussed their performances, benefits, and shortcomings. They identified many types of miniaturized sensors such as thickness–shear resonators, electromagnetic–acoustic resonators, vibrating bridge devices, double membrane devices, and micromachined plate devices.

Resonant sensors are applied in numerous areas ranging from monitoring the oil quality of engines [2] to measuring microsamples [3,4] and fluid properties in process lines [5]. Potential resonators in large robust industrial sensors include tuning forks [6,7], cylindrical torsional resonators [8–12], spiral springs [13], paddles [8], u-shaped wires [14], and tubular resonators [5,15–17]. Despite the wide variations in geometry, all sensors interact with the surrounding fluid, which alters the resonance frequency and the damping of the resonator. To measure fluid density, the oscillation of the resonator must produce a normal velocity component on its surface, causing mass displacement of the fluid. Transversely vibrating structures, such as tuning forks, reeds, and wires, were traditionally used to measure the fluid's density.

This thesis focuses on torsional resonators. Traditionally, torsional resonators are purely cylindrical; therefore, they do not create mass displacements that are required to measure density. Cylindrical resonant elements emit only shear waves, which predominantly create viscous damping. This damping affects both the resonance frequency and bandwidth of the resonator. Brack et al. [9,18,19] and Valtorta [20] analyzed both quantities, which enabled the measurement of effects such as viscoelasticity. It is also possible to measure the fluid density using torsional resonators if the oscillation has a normal velocity component on its surface. Torsional resonators are attractive because they are less prone to wall effects than transversely vibrating devices. Examples of torsional resonators include the symmetrical torsional resonator presented by Goodbread et al. [21,22] and the resonating paddle devised by Heinisch et al. [8].

Fuchs et al. [5] presented a process-integrated torsional resonance sensor,; they described a straight-tube coriolis sensor, in which an eccentric mass was attached to a transversely vibrating tube through which a fluid was flowing. The sensor was capable of measuring the fluid's viscosity, density and mass flowrate. Other flow-through sensors based on torsional resonators focused only on measuring the fluid's viscosity. Clara et al. [15] presented a torsional tubular resonator with flow-through capabilities; however, their sensor created a large obstruction to the flow because the inlets and outlets were perpendicular to the tube axis. This problem was overcome by Häusler et al. [16,17] and Fuchs et al. [5]. Häusler et al. [16,17] presented a tubular sensor to measure the viscosity of blood (see Figure 1). The sensor consisted of a small tube with an inner diameter of 2 mm in which the excited torsional mode was spatially restricted by two decoupling masses. With this system, they were able to measure the blood viscosity at different hematocrits.

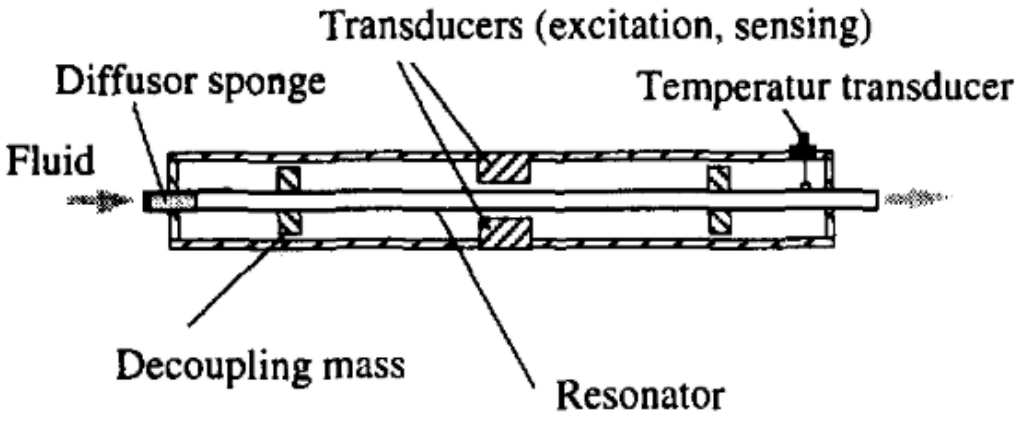

Figure 1: Tubular viscosity sensor [16]

To develop, calibrate, and gain insights into the working principle of these sensors, analytical and numerical models are required. In most cases, the sensors can be modeled based on a simplified, single-degree-of-freedom analytical model, such as a mass–spring system. This approach was generically described by Heinisch et al. [23], who applied a reduced-order model based on lumped elements to describe a resonator's behavior. The behavior of various resonant elements, such as cylindrical torsional resonators [8], tuning forks [13], torsional paddles [24], cantilevers [25], and microchannels [26], can be modeled using similar mass–spring models. In these models, the fluid interactions are typically described using separate damping and mass-loading terms. The mass-loading term increases the mass of the resonator, whereas the damping term damps the oscillation. The magnitude of the damping and mass-loading terms can be derived from the interaction of the resonant element with the fluid.

To date, most analytical work on fluid models for resonant elements has been done on either flat in-plane oscillating plates or cylindrical geometries. In-plane oscillating planes are most relevant for thickness–shear resonators. Sensors of this type comprise a quartz disk that is excited by means of the piezoelectric effect; the quartz disk emits only shear waves similar to cylindrical torsional resonators. Johannsmann [27] reviewed the fundamentals of quartz disks, which included several fluid models for in-plane oscillating plates (e.g., Newtonian, viscoelastic, and non-Newtonian fluids); the interactions of a shear wave with a thin film and the deposits and fluids stratified in layers were also considered. For non-flat geometries, such as torsional resonators, the mathematical models reviewed by Johannsmann [27] can be used if the radius of the cylinder is much larger than the length scale of the fluid (i.e., the boundary-layer thickness). In case the boundary thickness increases, the curvature of the cylinder or tube must be considered [28], [10,19], [12], [5].

For more complex geometries, analytical models become insufficient to describe either the viscous damping or the mass loading caused by the fluid. In such cases, the fluid–structure interactions can be solved numerically. Most numerical models are two dimensional because of the high computational requirements associated with full three-dimensional simulations. Mahmoodi [29] studied a torsional paddle using a two-dimensional fluid–structure interaction model. Reichel [30] presented a two-dimensional simulation to study different parameter sets of an oscillating rectangle and obtain the scaling properties for large sensors.

By coupling these analytical and numerical models, we can obtain valuable insights into resonator behaviors, which will help develop a new generation of sensors and reduce experimental work.

1.1 Research motivation

Mechanical resonators are compact robust sensors that have the potential to measure fluid properties in real time; these resonators have several advantages over the traditional rheological laboratory instruments. However, they are not yet commonly used in industrial processes for monitoring fluid properties, such as viscosity and density. Accurate numerical models have the potential to accelerate the development of industrial-grade sensors by reducing development time, and they can reduce the number of experiments required to characterize new sensors. In addition, it is possible to obtain a deeper understanding of the interactions between fluids and resonators from accurate numerical models than from experimental methods. Accurate numerical models can be used to disentangle the cross sensitivities of different fluid properties, such as viscosity and density, with respect to their effects on a sensor's behavior. Furthermore, numerical simulations enable model-based design optimization during the development of new generations of sensors.

1.2 Problem statement

This thesis was conducted in collaboration with the UiT the Arctic University of Norway, the ZHAW University of Applied Sciences in Winterthur, Switzerland and Rheonics GmbH, a spinoff company of the department of mechanical systems of the ETH Zurich. Rheonics GmbH specializes in building viscosity–density sensors based on torsional resonance, and their sensors are mainly used to measure fluid properties in industrial processes. This thesis aims to deepen the understanding of the working principle of their sensors and develop a new generation of non-intrusive sensors for the in-line monitoring of fluid viscosity. Two kinds of sensors are investigated in this research: the viscosity–density sensor and non-intrusive viscosity sensor.

To obtain a deeper understanding of these torsional resonators, we need models that fully describe the interactions between the fluid properties and the measured properties of the sensor. Such models have the potential to reduce the development time of new generations of sensors and enhance the calibration schemes. Therefore, a viscosity–density sensor based on torsional resonance is proposed; this sensor will be investigated experimentally and numerically. The sensor is shown in Figure 2.

Figure 2: Viscosity–density sensor, type SRD, Rheonics GmbH

Most existing sensors for the real-time monitoring of viscosity are probe style. However, it is helpful to have a non-intrusive sensor that does not obstruct the fluid flow. Flow obstructions can cause problems in various processes, and they pose the challenges of cleaning-in-place procedures. Thus, this study also aims to develop, build, and test a new non-intrusive viscosity sensor. The sensor development will be based on the models that allow an optimized design for the application of viscosity measurements. This sensor builds upon the design discussed by Häusler et al. [16,17], wherein a tube is used as the resonator

body (see Figure 1). The new sensor extends the applicability and can measure a wide range of fluid properties when a fluid passes through a sensor.

1.3 Research questions

The research goal of this thesis is to obtain a deeper understanding of the fluid–structure interactions of torsional resonators with emphasis on the application of the viscosity and density measurements. The research problem can be summarized in the following research questions (RQs):

I. What is the underlying physics of torsional resonators in the context of viscosity and density measurement applications?

II. Are reduced-order models suitable for coupling the flow simulations with resonator models?

III. How can computational fluid dynamics (CFD) be used to compute the flow field around a torsional oscillating structure?

IV. How can we compensate for the cross sensitivities among fluid viscosity, density, and temperature?

1.4 Research objectives

The above RQs lead to the following research objectives:

I. To understand the working principle of existing viscosity–density sensors.

II. To identify a suitable coupling method to connect the reduced-order models with both analytical and numerical flow field solutions.

III. To investigate the different methods for obtaining the solution using CFD to compute the vibration-induced flow around a structure.

IV. To investigate the effect of the fluid viscosity and density on the resonator sensor for developing enhanced viscosity and density prediction models.

2 Research Methodology

The basic working principle of any resonance sensor is that the resonator's properties, specifically its resonance frequency and bandwidth, change as the resonator interacts with the surrounding fluid. The change in bandwidth and resonance frequency can related to the fluid's viscosity and density. This relation can be described through models, which are discussed in general terms in this Section. When necessary, illustrative example are given using the two sensors studied here.

The model of either sensor consists of two components: the first is a structural model that describes the behavior of the resonator, whereas the second describes the fluid interaction. Section 2.1 describes a series of structural models which can be used to predict the resonance frequency and bandwidth of torsional resonators. Within this structural model, the fluid interaction is represented by coefficients. These coefficients depend on the flow around the resonator and are discussed in Section 2.2. The models are validated experimentally, as discussed in Section 2.3.

The tubular probe-style viscosity-sensor and viscosity-density sensor are described by different structural and fluid models. The tubular viscosity-sensor is described by a single-degree-of-freedom model (Section 2.1.1), which describes the behavior of the considered torsional mode (Section 2.1.3). The fluid interaction of this resonator is discussed in Section 2.2.1 and 2.2.3. The probe-style viscosity-density sensor is described by a 2-mass, 3-spring system. This approach is discussed in general terms, i.e. a multi-degree-of-freedom system, in Section 2.1.2. The coupling between fluid and structural model is discussed in section 2.2.1. The flow field around cylindrical part of the probe-style viscosity-density sensor is discussed in Section 2.2.2, whereas the numerical flow model based on CFD is discussed in Section 2.2.4. In this section, the probe-style viscosity-density sensor's cylindrical tip with 4 radial fins is provided as an example. The experimental methods are similar for both sensors.

2.1 Analytical structural models

In most cases, the resonator can be considered as a linear continuous system like to a tube or a beam. In most applications, the sensors are designed to operate in one mode. To describe the behavior of this mode with respect to its resonance frequency and bandwidth, a single-degree-of-freedom model can be used (see Section 2.1.1). For structures in which either multiple modes are relevant or the modes are changed by fluid interactions, we need models with multiple-degrees-of-freedom (see Section 2.1.2). Continuous systems with infinite degrees-of-freedom are discussed in Section 2.1.3, wherein each mode (i.e., degree-of-freedom) can be described by a single-degree-of-freedom system.

2.1.1 Single-degree-of-freedom system

A single-degree-of-freedom system is a damped mass–spring system that has only one resonance frequency. This single-degree-of-freedom system describes most resonators in which only one resonance frequency is considered:

$$J\frac{\partial^2\varphi}{\partial t^2} + d\frac{\partial\varphi}{\partial t} + c\varphi = F(t) \tag{2.1}$$

where φ is the angular deflection in time t; J is an inertial mass; c is the spring constant; d is the damping term; and $F(t)$ is the transient excitation force.

Note that the damping term d and inertial mass J depend on the fluid properties and the resonator. These parameters are discussed at length in Section 2.2.

In more general terms, the resonator can be described as follows:

$$J\frac{\partial^2\varphi}{\partial t^2} + 2D\omega_0\frac{\partial\varphi}{\partial t} + \omega_0^2\varphi = F_N(t) \tag{2.2}$$

where $D\ is$ the normalized damping term; ω_0 is the angular resonance frequency; $F_N(t)$ is the normalized forcing term, and f_0 is the resonance frequency, Eqs. (2.3) to (2.5).

$$D = \frac{d}{2\sqrt{cJ}} \tag{2.3}$$

$$\omega_0 = 2\pi f_0 = \sqrt{\frac{c}{J}} \tag{2.4}$$

$$F_N(t) = \frac{F(t)}{J} \tag{2.5}$$

The resonator's damping is typically expressed by a quality factor $Q = (2D)^{-1}$ or a bandwidth $\Gamma = f_0/Q$. The resonator system is under-damped if the normalized damping term D is less than 1. This is a necessary criterion when a resonator is used to measure the viscosity of a fluid. When the normalized damping factor $D = 1$, means critical damping. When the damping factor D is greater than one, the system does not oscillate but decays into its equilibrium state without overshooting, that is, oscillating.

If we assume that the force term $F(t) = 0$, then the fundamental solution is an exponentially decaying oscillation with a logarithmic decrement of $\tau_d = (D\omega_0)^{-1}$. Then, we have the following equality:

$$\varphi = \varphi_0 e^{i\omega_0 t} \tag{2.6}$$

where ω_0 is the angular resonance frequency; $i = \sqrt{-1}$; and φ_0 is the angular deflection at $t = 0\ s$. The complex part of the angular resonance frequency ω_0 describes the exponential decay, that is, the logarithmic decrement $\tau_d = 1/imag(\omega_0)$.

In case the force term is a harmonic, we have

$$F(t) = \hat{F}e^{i\omega t} \tag{2.7}$$

where $\hat{F}$ is the amplitude of the force function $F(t)$, and ω is the angular frequency. Then, after the transient effects caused by the initial condition have phased out, the system eventually yields the quasi–steady-state solution $\varphi_s(t)$ as follows:

$$\varphi_s(t) = \frac{\hat{F}e^{i\omega t}}{J(\omega_0^2 + 2iD\omega_0\omega - \omega^2)} \tag{2.8}$$

By convention, the transfer function X is the ratio between the quasi–steady-state angular deflection and the harmonic force term. By convention, this transfer function is formulated as follows:

$$X = \frac{\varphi_s(t)}{\hat{F}e^{i\omega t}} = \frac{1}{J(\omega_0^2 + 2iD\omega_0\omega - \omega^2)} \tag{2.9}$$

This transfer function X describes the amplification of the angular deflection and the phase shift with respect to the excitation. The amplification is defined by the Euclidean norm of X as

$$|X| = \frac{\hat{\varphi}_s}{\hat{F}} = \frac{1}{J}\sqrt{\frac{1}{(\omega_0^2 - \omega^2)^2 + (2D\omega_0\omega)^2}} \tag{2.10}$$

where $\hat{\varphi}_s$ is the amplitude of the term $\varphi_s(t)$.

The phase shift $\Delta\varphi_s$ between the force term $F(t)$ and the steady-state solution of the angular defection $\varphi_s(t)$ is defined by the angle of X as follows:

$$\Delta\varphi_s = ang(X) = arctan\left(\frac{2D\omega_0\omega}{\omega_0^2 - \omega^2}\right) \tag{2.11}$$

Figure 3 shows the amplification and phase shift for the different normalized damping values D. With increasing normalized damping values, the amplification decreases, and the phase shift increasingly spreads over a wide frequency range.

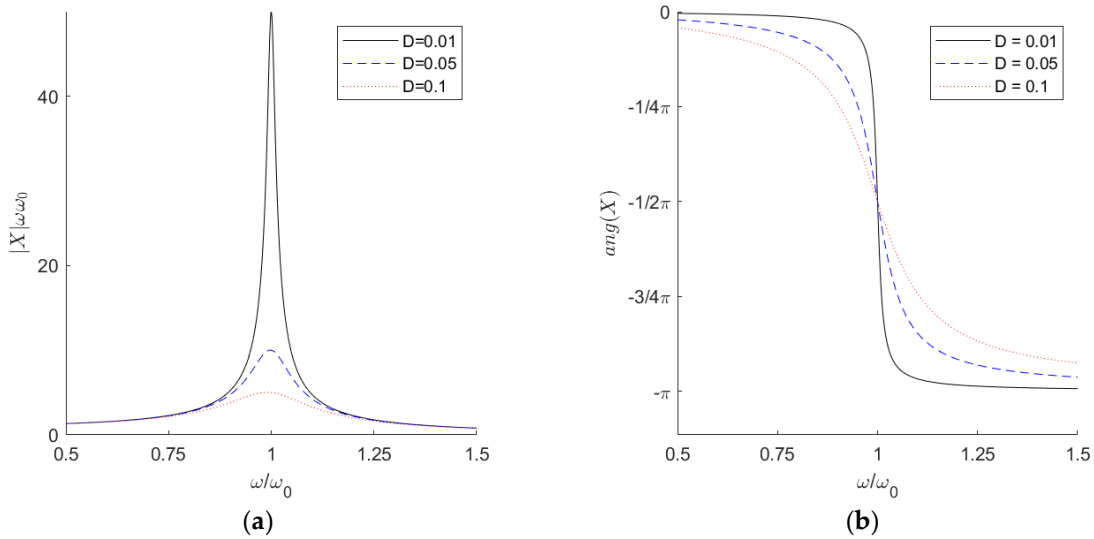

Figure 3: Amplitude (a) and phase (b) of a damped resonator at different normalized damping terms D = [0.01 0.05 0.1]; ω is the angular frequency; ω_0 is the angular resonance frequency; X is the transfer function; and $ang(X)$ is the phase shift between the excitation term and angular deflection of the resonator

To experimentally characterize a single-degree-of-freedom system, the bandwidth Γ and resonance frequency f_0 needs to be determined. The bandwidth of the system can be computed using three methods; all these methods result in the same bandwidth value. The definitions of the three methods are given below:

1. In the first method, the bandwidth is the frequency difference between the phase shift curves when they cross $-\pi/4$ and $-3\pi/4, as\ follows$:

$$\Gamma = \frac{\omega(ang(X(\omega)) = -\pi/4) - \omega(ang(X(\omega)) = -3/4\pi)}{2\pi} \tag{2.12}$$

2. In the second method, the bandwidth is the frequency difference when the amplification $|X|$ is $-3dB$ of its maximum value. The $-3dB$ point is corresponding to $-3dB = 20 \cdot log_{10}(1/\sqrt{2})$. Thus, the definition is given as follows:

$$\Gamma = \frac{\omega\left(\frac{|X(\omega)|}{max(|X(\omega)|)} = -3dB\right)_{\omega>\omega_0} - \omega\left(\frac{|X(\omega)|}{max(|X(\omega)|)} = -3\ dB\right)_{\omega<\omega_0}}{2\pi} \tag{2.13}$$

3. In the third method, when the excitation is turned off, the bandwidth is defined by the rate of exponential decay, as follows:

$$\Gamma = \frac{1}{\tau_d \pi} \tag{2.14}$$

Here, τ_d is the logarithmic decrement. The angular resonance frequency is defined by the phase shift $\Delta\varphi_s$ between the forcing function and angular deflection at exactly $-\pi/2$:

$$\omega_0 = \omega(ang(X) = -\pi/2) \tag{2.15}$$

For more complex systems, a single-degree-of-freedom system will not capture all the effects. To account for either multiple frequencies or modal distortions, a model having multiple-degrees-of-freedom is needed.

2.1.2 System with multiple-degrees-of-freedom

When the resonator is too complex to be simplified to a single-degree-of-freedom model, it is possible to use models with multiple-degrees-of-freedom. The likely scenarios include cases in which either multiple frequencies are of interest or the resonator itself is based on multiple masses and springs.

A model with multiple-degrees-of-freedom is a linear combination of several single-degree-of-freedom systems. Such systems have been discussed in detail by Irretier [31]. The dynamics of the system is given by the following system of differential equations:

$$\boldsymbol{J}\frac{\partial^2\vec{\varphi}}{\partial t^2} + \boldsymbol{D}\frac{\partial\vec{\varphi}}{\partial t} + \boldsymbol{C}\vec{\varphi} = \vec{F} \tag{2.16}$$

where the angular deflection of the torsional resonator $\vec{\varphi}$ is described by a vector and the inertial mass matrix $\boldsymbol{J}$, the damping matrix $\boldsymbol{D}$, the stiffness matrix $\boldsymbol{C}$, and the force term $\vec{F}$.

The angular deflection vector $\vec{\varphi}$ has n elements, where each element represents one differential equation in the system. Note that $\vec{\varphi}$ is used here as a vector quantity, whereas φ in Section 2.1.1. was a scalar quantity.

For an angular displacement vector $\vec{\varphi}$ with n elements, matrices $\boldsymbol{J}$, $\boldsymbol{D}$, and $\boldsymbol{C}$ will be of size $n \times n$. The force term $\vec{F}$ has the same number of elements as $\vec{\varphi}$. In case the system of differential equations is homogeneous, that is, if $\vec{F} = \vec{0}$, there will be n fundamental solutions of the kind shown in the following equation:

$$\vec{\varphi}_m = \hat{\vec{\varphi}}_m \cdot e^{i\omega_{0,m}t} \tag{2.17}$$

where $\omega_{0,m}$ is the angular resonance frequency of the angular deflection amplitude vector $\hat{\vec{\varphi}}_m$ (mode shape), $i = \sqrt{-1}$, and t is the time.

The angular resonance frequencies and their corresponding mode shapes for the undamped system can be determined by solving the following eigenvalue problem:

$$(\boldsymbol{J}\lambda^2 + \boldsymbol{C})\vec{\varphi} = \vec{0} \tag{2.18}$$

where $\lambda = i\omega_{0,m}$ represents a solution of an eigenvalue, and $\hat{\vec{\varphi}}_m$ is its eigenvector. Therefore, each eigenvector and its corresponding eigenvalue builds the fundamental solution shown in Eq. (2.17).

To solve the eigenvalue problem, the following condition must be satisfied:

$$det\ (\lambda\boldsymbol{J} + \boldsymbol{C}) = 0 \tag{2.19}$$

When damping is included, the eigenvalue problem becomes more complex, Eq. (2.20).

$$(\boldsymbol{J}\lambda^2 + \boldsymbol{D}\lambda + \boldsymbol{C})\vec{\varphi} = \vec{0} \tag{2.20}$$

The eigenvalues λ of Eq. (2.20) are complex; the real part is the angular resonance frequency, and the complex part is the inverse of the logarithmic decrement. Thus, a multiple-degrees-of-freedom system, which consists of inertial masses and springs, can predict the angular resonance frequency and system bandwidth.

However, such multiple-degrees-of-freedom systems require the inertial mass is localized at points. For continuous resonators the inertial mass is distributed, thus such resonators are described by continuous systems, see Section 2.1.3.

2.1.3 Continuous resonator

The mode structure of a tube-style resonator can be derived based on a linear mechanical system with infinite modes. The shape and resonance frequency of the modes is obtained by a modal analysis of the following differential equation:

$$\frac{\partial}{\partial x}\left(GI_p \cdot \frac{\partial \Psi}{\partial x}\right) = \rho_s I_p \frac{\partial^2}{\partial t^2}\Psi \tag{2.21}$$

where the angular deflection Ψ is a function of the position x and time t; G is the shear modulus, ρ_s is the denisty of the resonator, and I_p is the second moment of the area. Note that Ψ is used for continuous systems in the space domain, whereas φ and $\vec{\varphi}$ were used for discrete systems in Section 2.1.1 and Section 2.1.2.

In case of a straight, homogeneous tube, neither the shear modulus nor the second moment of inertia depend on the axial position x; therefore, Eq. (2.21) is reduced to the following traditional wave equation:

$$GI_p \frac{\partial^2 \Psi}{\partial x^2} = \rho_s I_p \frac{\partial^2}{\partial t^2}\Psi \tag{2.22}$$

The solution to Eq. (2.22) with two nodal points as boundary conditions, Eqs. (2.23) and (2.24),

$$\Psi(x = 0) = 0 \tag{2.23}$$

$$\Psi(x = L) = 0 \tag{2.24}$$

is given as Eq. (2.25).

$$\Psi = A \cdot sin\left(k\pi \frac{x}{L}\right) \cdot e^{i\omega_0 t} \tag{2.25}$$

Here, A is the complex wave amplitude; k is the wave number; ω_0 is the angular resonance frequency; and L is the distance between the nodal points $(x = 0)$ and $(x = L)$.

The angular frequency depends on the wave number k and is associated with its corresponding mode as follows:

$$\frac{G}{\rho_s}\left(\frac{k\pi}{L}\right)^2 = \omega_0^2 \tag{2.26}$$

To obtain the angular resonance frequency and the mode shape for a non-constant tube radius, Eq. (2.21) is solved directly. The obtained solution can then be written as follows:

$$\Psi = \hat{\Psi} e^{i\omega_0 t} \tag{2.27}$$

where $\hat{\Psi}$ is the amplitude of the mode at the position *x*.

A method to obtain a solution is by solving Eq. (2.21) numerically under quasi–steady-state conditions, for example by using MATLAB®. Figure 4 shows an example of a solution of Eq. (2.21) for a tube having a thick central section with the boundary conditions given by Eqs. (2.23) and (2.24). It is possible to obtain different solutions for the mode shapes and their corresponding resonance frequency by choosing different initial conditions for the numerical solver. Figure 6 shows the mode shapes at the three lowest angular resonance frequencies, that is, Modes 1–3.

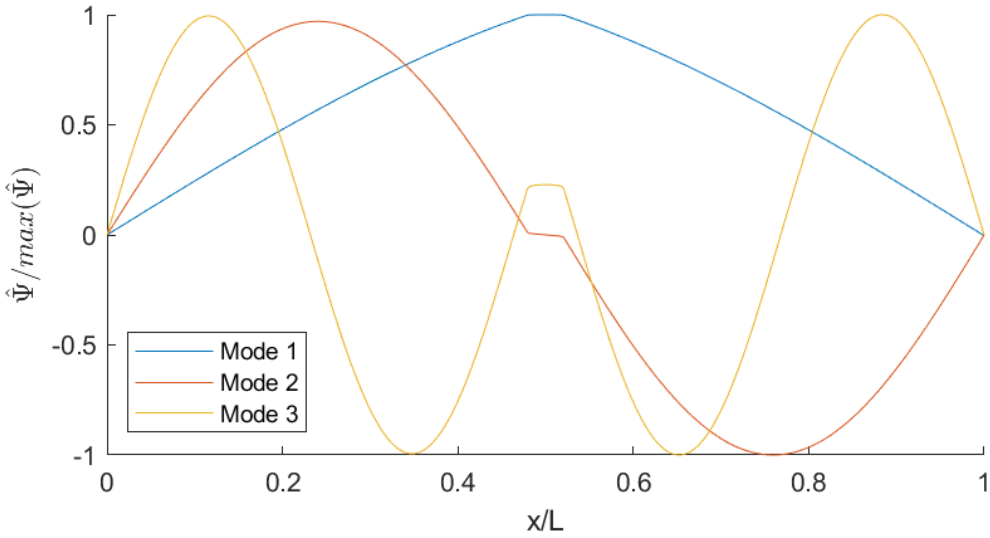

Figure 4: Normalized shapes of the three first modes of a torsional resonating tube with a thick central section; x is the axial position; L is the distance between the nodal points; and $\hat{\Psi}$ is the angular deflection amplitude

Each mode can be described by a single-degree-of-freedom system for which the corresponding inertial mass J, the spring constant c, and the damping term d must be determined. The inertial mass J and damping term d depend on the fluid; the damping term d depends on the fluid properties and the intrinsic damping of the resonator, and J is a combination of the inertial mass of the fluid J_f and the inertial mass of the structure J_0. Modal analysis gives the values of the inertial mass of the structure J_0 and the spring constant c. The parameters d and J_f are discussed in Section 2.2.

The inertial mass of the structure J_0 for each mode is calculated by integrating the second moment of the area over the modal function:

$$J_0 = \int_{-\frac{l}{2}}^{-\frac{l}{2}} \hat{\Psi}(x) \cdot I_p(x) \rho_s \, dx \tag{2.28}$$

where the solution is normalized such that $max(|\Psi(x)|) = 1$.

The spring constant c of the corresponding single-degree-of-freedom system is obtained as follows:

$$c = J_0 \cdot {\omega_0}^2 \tag{2.29}$$

where ω_0 is the angular resonance frequency of the corresponding mode.

In Section 2.1, the structural part of the resonator was discussed. To predict the resonance frequency and bandwidth based on the fluid properties, the fluid-dependent terms J and d need to be determined (see Section 2.2).

2.2 Analytical and numerical fluid models

To integrate the fluid interactions into the structural model with either a single-degree-of-freedom or multiple-degrees-of-freedom (see Sections 2.1.1 to 2.1.3), the damping and inertial mass caused by the fluid needs to be determined. The damping and inertial mass terms were derived based on the flow and pressure fields, see Section 2.2.1.

Different computations were made for the flow field based on each sensor component's geometry. Section 2.2.2 describes the simplest fluid model based on an oscillating flat plate. Section 2.2.3 describes a torsional oscillating cylinder, which increases the model's complexity due to a curved surface. If no analytical solution can be found, CFD provides the means to compute the flow and pressure fields numerically (see Section 2.2.4).

2.2.1 Fluid forces on a resonating body

When resonators are described structurally as mass-spring systems, the fluid's impact on the dynamics of the resonator must be accounted for in the inertial mass and damping terms (J and d, respectively). In single- or multiple-degree-of-freedom systems, solving for J and d through fluid models enables the coupling of the fluid domain with the structural domain. The spring constant c and the matrix $\boldsymbol{C}$ of a system with a single-degree-of-freedom or multiple-degrees-of-freedom, respectively, is given using resonator geometry. The total inertial mass J and the damping term d for a system with a single-degree-of-freedom and the matrices $\boldsymbol{J}$ and $\boldsymbol{D}$ for a system with multiple-degrees-of-freedom depend on the fluid interaction. Each position in the matrices $\boldsymbol{J}$ and $\boldsymbol{D}$ can be determined in the same manner as the inertial mass J and the damping term d for a system with a single-degree-of-freedom. Therefore, hereinafter, we focus only on the terms J and d.

The inertial mass J is the sum of the inertial mass of the structure J_0 and the inertial mass of the fluid J_f. This total is given by the following equation:

$$J = J_0 + J_f \tag{2.30}$$

Similarly, the damping term is the sum of the intrinsic damping of the resonator d_0 and the fluid damping d_f.

$$d = d_0 + d_f \tag{2.31}$$

Note that the intrinsic damping d_0 is independent of the fluid interaction and is a superimposed damping effect that is experimentally determined see Section 2.3.3.

The two parameters d_f and J_f are real, positive values that depend on the fluid properties, sensor geometry, frequency of the resonator. Both parameters are derived based on the pressure and velocity fields surrounding the resonator. Therefore, the pressure-induced torque $M_{p,t}$ and the shear stress–induced torque $M_{v,t}$ acting on the fluid–structure boundary $d\Omega_r$ are computed as follows:

$$M_{v,t}(t, \eta, \rho, \omega, \hat{\varphi}) = \eta \vec{e}_i \cdot \int_{d\Omega_r} \left(\vec{r} \times (\vec{n} \cdot \nabla \vec{u})\right) dA \tag{2.32}$$

$$M_{p,t}(t, \eta, \rho, \omega, \hat{\varphi}) = \vec{e}_i \cdot \int_{d\Omega_r} (p\vec{n} \times \vec{r}) dA \tag{2.33}$$

where η is the dynamic viscosity of the fluid; ρ is the fluid density; $\hat{\varphi}$ is the angular deflection amplitude; ω is the angular frequency; $\vec{n}$ is the surface normal of the boundary; $\vec{r}$ is the distance from the axis; p is the pressure field; $\vec{u}$ is the velocity field; and $\vec{e}_i$ is the unity vector of the torsional axis.

Due to the harmonic oscillation of the system, the pressure and viscous amplitude are periodic if the system behaves linearly. Note that for non-periodic solutions, strong fluid–structure coupling may have to be considered; therefore, the method described in this section may not be suitable.

The amplitudes of the pressure and shear stress–induced torque are obtained by Fourier analysis. Due to the linearity of the system, the amplitude is zero for any frequency other than the frequency of the excitation. Therefore, only the amplitude at the angular frequency ω of the excitation is determined, see Eqs. (2.34) and (2.35):

$$\widehat{M}_v(\omega,\eta,\rho,\hat{\varphi}) = \mathcal{F}\left(M_{v,t}(t,\eta,\rho,\omega,\hat{\varphi})\right) \tag{2.34}$$

$$\widehat{M}_p(\omega,\eta,\rho,\hat{\varphi}) = \mathcal{F}\left(M_{p,t}(t,\eta,\rho,\omega,\hat{\varphi})\right) \tag{2.35}$$

where $\widehat{M}_v$ is the amplitude of the complex shear stress torque; $\widehat{M}_p$ is the amplitude of the complex pressure torque; and $\mathcal{F}()$ is the operator of the Fourier analysis.

The inertial mass of the fluid J_f and the fluid damping term d_f are obtained from the real and imaginary parts of the sum of the amplitudes of the pressure and shear stress torque, Eqs. (2.36) and (2.37).

$$J_f = \Re\left(\frac{\widehat{M}_p(\omega,\eta,\rho,\hat{\varphi}) + \widehat{M}_v(\omega,\eta,\rho,\hat{\varphi})}{\omega^2\hat{\varphi}}\right) \tag{2.36}$$

$$d_f = \Im\left(\frac{\widehat{M}_p(\omega,\eta,\rho,\hat{\varphi}) + \widehat{M}_v(\omega,\eta,\rho,\hat{\varphi})}{\omega\hat{\varphi}}\right) \tag{2.37}$$

Thus, the damping term d and inertial mass J can be computed by using Eqs. (2.30) and (2.31) based on the properties of the fluid and resonator, which allows the prediction of the resonance frequency and bandwidth through the previously described structural models, see Section 2.1.

However, to compute the terms $\widehat{M}_p(\omega,\eta,\rho,\hat{\varphi})$ and $\widehat{M}_v(\omega,\eta,\rho,\hat{\varphi})$, the solution of the velocity and pressure fields needs to be known. The solution method also depends on the geometry, as discussed in Sections 2.2.2–2.2.4.

2.2.2 In-plane oscillating plate

The in-plane oscillating plate is a fluid model that is commonly used; it is especially suitable for shear wave–emitting piezoelectric sensors, such as thickness–shear resonators or cylindrical torsional resonators. Johannsmann [27] investigated many different fluid and solid constellations of an in-plane oscillating plate, ranging from single to multiple fluid/solid layers with either Newtonian or viscoelastic properties. In this section, only Newtonian fluids in a semi-infinite domain are considered.

In this approach, the flow u_x over the surface is modeled under the assumption that the flow is unidirectional (especially in the *x*-direction), and the flow changes only in the *z*-direction, normal to the flow direction u_x. Therefore, we have

$$\frac{\partial u_x}{\partial t} = \frac{\eta}{\rho}\frac{\partial^2 u_x}{\partial z^2} \tag{2.38}$$

where t is the time; η is the dynamic viscosity; ρ is the fluid density; and z is the distance from the surface.

Eq. (2.38) can be solved under the assumption of a periodic solution as follows:

$$u_x i\omega = \frac{\eta}{\rho}\frac{\partial^2 u_x}{\partial z^2} \tag{2.39}$$

where ω is the angular velocity, and $i = \sqrt{-1}$.

The boundary conditions are imposed on the surface of the plate and at an infinite distance to obtain Eqs. (2.40) and (2.41),

$$u_x(z = 0) = \omega\widehat{\Psi}\hat{\varphi}e^{i\omega t} \tag{2.40}$$

$$u_x\left(\lim_{z\to\infty} z\right) = 0 \tag{2.41}$$

where $\hat{\varphi}$ is the amplitude of the oscillation, and $\widehat{\Psi}$ is the value of the modal function.

The solution to Eq. (2.39) is given as follows:

$$u_x(z, t) = -\omega\widehat{\Psi}\hat{\varphi}e^{\frac{z}{\delta(1+i)}}e^{i\omega t} \tag{2.42}$$

where δ is the thickness of the boundary layer and represents the length scale of the flow; this thickness is the distance from the wall where the velocity amplitude is e^{-1} times its original velocity amplitude as follows:

$$\delta = \sqrt{2\frac{\eta}{\rho\omega}} \tag{2.43}$$

The boundary-layer thickness δ is independent of the wall velocity and depends only on the dynamic viscosity η, fluid density ρ, and the angular velocity ω.

The in-plane oscillating plate model can be used when the length scale of the flow δ is much smaller than the scale of geometrical features of the resonating structure (e.g., cylinder), and the radius is much larger than the flow structure. If the boundary-layer thickness is in the same order of magnitude than the

radius, then the curvature of the tube or cylinder would influence the flow field. This case has been discussed in Section 2.2.3.

2.2.3 Torsional oscillating tube

The model described in Section 2.2.2 neglects the curvature of the structure's surface (e.g., the tube of the tubular viscosity-sensor). This approach is reasonably accurate when the radius of the tube is much larger than the boundary-layer thickness. As the boundary-layer thickness increases, the curvature must be included in the fluid model. For this, the equations of fluid mechanics are solved using cylindrical coordinates under the assumption that there is no axial flow, no azimuthal change, and no radial flow, as shown in the following equations:

$$\frac{\partial u_\alpha}{\partial t} = \frac{\eta}{\rho}\left(\frac{1}{r}\frac{\partial u_\alpha}{\partial r} + \frac{\partial^2 u_\alpha}{\partial r^2} + \frac{u_\alpha}{r^2}\right) \tag{2.44}$$

$$\frac{{u_\alpha}^2}{r} = \rho\frac{\partial p}{\partial r} \tag{2.45}$$

where u_α is the azimuthal velocity; r is the radial coordinate; ρ is the fluid density; η is dynamic viscosity; and p is the pressure.

Assuming temporal periodicity, we have the following equations from Eq. (2.45):

$$i\omega u_\alpha = \frac{\eta}{\rho}\left(\frac{1}{r}\frac{\partial u_\alpha}{\partial r} + \frac{\partial^2 u_\alpha}{\partial r^2} - \frac{u_\alpha}{r^2}\right) \tag{2.46}$$

where ω is the angular frequency, and $i = \sqrt{-1}$.

The solution for Eq. (2.46) is given as follows:

$$u_\alpha(r) = c_1 J_1\left((-1)^{\frac{3}{4}} r\sqrt{\frac{\omega\eta}{\rho}}\right) + c_2 Y_1\left(-(-1)^{\frac{3}{4}} r\sqrt{\frac{\omega\eta}{\rho}}\right) \tag{2.47}$$

where J_1 is the Bessel function of the first kind and first order; Y_1 is the Bessel function of the second kind and first order; and c_1 & c_2 are constants that are determined by the following boundary conditions:

$$u_\alpha(r = 0) = 0 \tag{2.48}$$

$$u_\alpha(r = R) = \omega\hat{\varphi}\widehat{\Psi}R \tag{2.49}$$

where R is the inner radius of the tube, $\hat{\varphi}$ is the angular deflection amplitude and $\widehat{\Psi}$ is the value of the modal function.

Note that for computing the damping term d_f and the inertial mass J_f in Eqs. (2.30) and (2.31), respectively, the mode shape described by the modal function $\widehat{\Psi}$ needs to be considered. The mode shape $\widehat{\Psi}$ for a tube has been discussed in Section 2.1.3.

A solution of Eq. (2.46) is shown in Figure 5 for four fluids with different viscosities at a fluid density of 1000 kg/m^3. When the viscosity increases, the velocity field $u_\alpha(r)$ penetrates further into the tube.

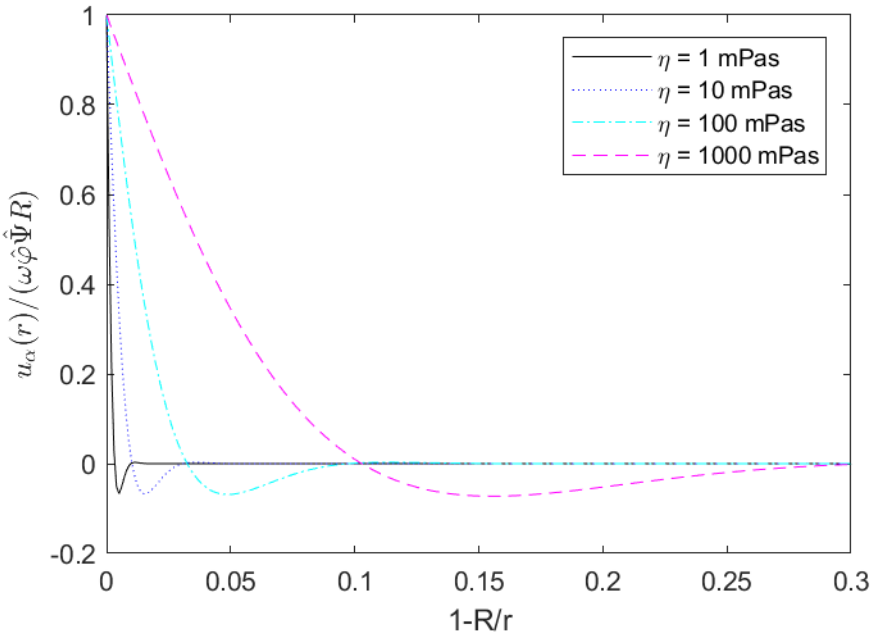

Figure 5: Flow field in a tube for viscosities η of four fluids at a fluid density of 1000 kg/m³. Here, $u_\alpha/(\omega\hat{\varphi}\hat{\Psi}R)$ is the normalized azimuthal velocity; r is the radial position; and R is the inner radius of the tube.

Analytical solutions have been presented for either flat or circular geometries. However, there is no guarantee that analytical solutions can be found for more complex geometries. Section 2.2.4 introduces a numerical approach to compute the flow field. This approach is suitable for arbitrary geometries.

2.2.4 Computational fluid dynamics

A more general approach to obtain the velocity and pressure fields around a resonating structure is by numerically solving the fluid mechanics equations. In this study, the flow was assumed to be incompressible, thermally uniform, homogeneous, and Newtonian, as given below:

$$\nabla \cdot \vec{u} = 0 \tag{2.50}$$

$$\rho\left(\frac{\partial \vec{u}}{\partial t} + (\vec{u} \cdot \nabla)\vec{u}\right) = -\nabla p + \eta \Delta \vec{u} + \vec{F} \tag{2.51}$$

Here, ρ is the fluid density; $\vec{u}$ is the velocity field; p is the pressure field; $\vec{F}$ is a force term; η is the dynamic viscosity; and t is the time.

The amplitude of the torsional vibration was very small compared to the size of the structure. Therefore, the convective term of the fluid mechanics equations $(\vec{u} \cdot \nabla)\vec{u}$ is negligible, as shown in Eq. (2.52). Neglecting the convective term reduces the computational effort. However, the validity of this assumption is case specific; therefore, it needs to be treated as such.

$$\rho\left(\frac{\partial \vec{u}}{\partial t}\right) = -\nabla p + \eta \Delta \vec{u} + \vec{F} \tag{2.52}$$

In Sections 2.2.2 and 2.2.3, the flow field is analytically computed by assuming temporal periodicity and a simple geometry. To compute the flow around a sensor tip (as shown in Figure 2), it is not possible to simplify the fluid mechanics equations and the boundary conditions to a degree for which analytical solution can be found. Thus, to obtain a solution of the velocity and pressure fields, Eqs. (2.50) and (2.51) or Eqs. (2.50) and (2.52) are solved numerically.

There are two main approaches for numerically solving the fluid mechanics equations: the finite volume method [32] and the finite element method [33].

The difference between the finite volume and finite element methods lies in how the equations are discretized. In the simplest terms, the finite volume method solves for the fluxes between the cells. The main advantage of this method is that the mass flux is inherently conserved, that is, the mass flux that is transferred from one cell to another cell has the same value. Therefore, even if the flux has a numerical error from the solver, the mass is neither created nor lost.

The finite element method is different; it uses the shape functions for the derivatives. The advantage of using shape functions is that higher-order discretization schemes can be used unlike the finite volume method. However, the numerical method does not inherently conserve mass flux. Thus, there might be some discrepancy in the flux from one cell to another. However, for many numerical applications, this error is negligible.

In this research, the fluid mechanics application was solved using two commercial software solutions: COMSOL Multiphysics® and ANSYS CFX®. COMSOL Multiphysics® is a finite element code, whereas ANSYS CFX® follows the finite volume method. To ensure that the solution is independent of the numerical method, both methods must yield the same solution. Then, we can safely conclude that the obtained solution is independent of the numerical method.

Reduced-order modeling

The fluid mechanics application used in this research focuses on the viscosity–density sensors. In particular, the flow and pressure fields around the torsional oscillating sensor tip (see Figure 2) are solved to determine the inertial mass and viscous damping term (Eqs. (2.30) and (2.31)) of the fluid. However, there is a large difference in the orders of magnitudes between the fluid length scale and geometrical length scale; therefore, a full resolution of the flow field in a three-dimensional domain around the sensor tip exceeds current computational resources.

An estimate of the fluid length scale can be obtained by assuming that the flow behaves similar to the flow over an in-plane oscillating plate, as discussed in Section 2.2.2. Then, the fluid length scale of the flow is the boundary layer thickness δ (see Eq. (2.38)). For a fluid with the properties of water, this boundary layer thickness (i.e., the fluid length scale) is approximately $6.5\ \mu m$. This thickness is much smaller than the diameter of the shaft (5 mm) or the elapsing diameter of the tip (12 mm). The difference in the length scales poses a considerable challenge because the cells need to be sufficiently small for resolving the flow near the boundary, but the computational domain is comparatively very large. Therefore, to accurately compute the flow, a very large number of cells is necessary.

One way to overcome this challenge is by reducing the computational domain to a cross section, which lowers the number of cells by two to three orders of magnitude. However, this simplification causes any edge effects on the tip to be neglected, which results in a systematic error in the computed inertial mass and viscous damping term (Eqs. (2.30) and (2.31)). If said error is small, the qualitative trends can still be captured and applied in practice, even when a two-dimensional cross section of the structure is used.

To accurately compute the flow within the cross section, the mesh resolution must be sufficiently high, that is, refining the mesh further should not change the solution of the flow. Figure 6 shows the mesh of the cross section of the tip of one resonator studied in this thesis, which is sufficiently resolved. Therefore, the flow solution is independent of further mesh refinement and can be considered mesh independent.

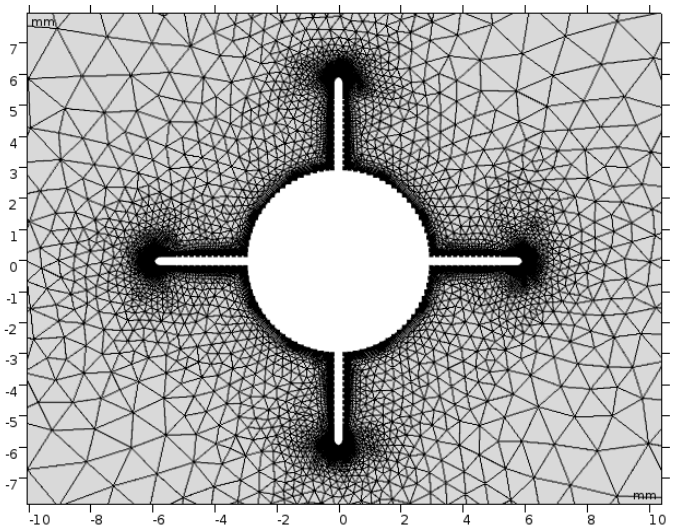

Figure 6: Two-dimensional mesh of the computational domain in COMSOL Multiphysics® with 26558 elements

Hereafter, the independence of the numerical method and mesh independence are assumed. There are several methods to describe the structural vibration and thereby compute the flow around the given vibrating structure.

The solutions of the flow and the pressure fields must also be invariant under different methods for applying the torsional oscillation. The torsional oscillation of the structure was modeled using two methods: moving wall and frame of reference.

- *Moving wall approach*
  In the moving wall approach, the torsional vibration is modeled by the boundary condition of the oscillating structure. The torsional oscillation is around the axis $\vec{e}_i$, which is normal to the computational domain (i.e., the cross section). The velocity at the boundary of the resonator $d\Omega_r$ is defined by Eq. (2.53) as

$$\vec{u}(d\Omega_r) = \omega\widehat{\Psi}\hat{\varphi} \cdot cos(\omega t)\,(\vec{r} \times \vec{e}_i) \tag{2.53}$$

  where $\vec{u}$ is the velocity field; ω is the angular frequency; $\vec{r}$ is the distance from the axis $\vec{e}_i$ to the boundary; $\hat{\varphi}$ is the oscillation amplitude; and $\widehat{\Psi}$ is the value of the modal function.

- *Frame of reference*
  Instead of inducing the torsional vibration on the wall, the frame of reference approach induces the motion in the domain. Thereby, the force term $\vec{F}$ is replaced by the centrifugal acceleration $\vec{\Omega} \times (\vec{\Omega} \times \vec{r})$, Coriolis acceleration $2\vec{\Omega} \times \vec{u}$, and Euler acceleration $(\partial\vec{\Omega})/(\partial t \times \vec{r})$, as follows:

$$\rho\left(\frac{\partial\vec{u}}{\partial t} + \vec{u} \cdot \nabla\vec{u} + 2\vec{\Omega} \times \vec{u} + \vec{\Omega} \times \left(\vec{\Omega} \times \vec{r}\right) + \frac{\partial\vec{\Omega}}{\partial t} \times \vec{r}\right) = -\nabla p + \eta\Delta\vec{u} \tag{2.54}$$

  where $\vec{\Omega}$ is the rotation vector of the domain. The motion of the domain is described by $\vec{\Omega}$ as,

$$\vec{\Omega} = \overrightarrow{e_i}\widehat{\Psi}\hat{\varphi} \cdot sin(\omega t) \tag{2.55}$$

  where ω is the angular frequency; $\overrightarrow{e_i}$ is the unity vector of the torsional axis; $\hat{\varphi}$ is the oscillation amplitude; and $\widehat{\Psi}$ is the value of the modal function.

Note that the modal function $\widehat{\Psi}$ is constant for a cross section. However, when computing the damping term d_f and the inertial mass J_f, the shear stress–induced and pressure-induced torques are integrated over the axis of the resonator, where $\widehat{\Psi}$ is not constant.

Sections 2.2.2 through 2.2.4 describe a numerically robust method for obtaining a solution for the flow and pressure fields. This solution can be coupled with the analytical structural model (discussed in Section 2.1) to numerically determine the bandwidth and resonance frequency a sensor. Before these numerical predictions can be incorporated into the sensor design process, they must be experimentally validated, as discussed in Section 2.3.

2.3 Experiments

Resonance-based viscosity–density sensors can be considered as devices that measure the resonance frequency, bandwidth, and temperature. Based on these measured properties, the fluid viscosity and density are predicted. To avoid complex multi-dimensional prediction models that require many experiments for calibration, we need parameters that describe the viscosity and density without reciprocal effects. Section 2.3.1 discusses a parameter that can be used to describe the density, and Section 2.3.2 discusses a parameter for the product of fluid viscosity and density.

Section 2.3.3 presents the experimental protocols that verify that there are no cross sensitivities for either the viscosity prediction or the density prediction.

2.3.1 Density measurement

To determine the fluid density based on the measured bandwidth and resonance frequency, a parameter that depends only on the fluid density is required. This parameter can be derived based on a single-degree-of-freedom resonator. Therefore, the resonance frequency of the resonator is defined as follows:

$$f_0 = \frac{1}{2\pi}\sqrt{\frac{c}{J}} \tag{2.56}$$

where c is the spring constant, and J is the inertial mass (see Section 2.1.1).

The inertial mass J can be decomposed into two parts: the inertial mass of the fluid J_f and the representative inertial mass of the structure J_0 (see Eq. (2.30)). The inertial mass caused by the fluid J_f is proportional mainly to the fluid density; however, it is also affected by the viscous effects.

The resonance frequency is affected by the fluid viscosity and temperature. These effects were compensated as follows:

- *Effects of viscosity:*
  The flow field is described by the model presented in Section 2.2.2. In this model, the flow equally contributes to the inertial and damping terms. This additional inertial mass creates a viscosity dependence. For compensation, half the bandwidth was added to the resonance frequency.
- *Effects of temperature:*
  Temperature affects the shear modulus of the resonator, which affects its undamped frequency and the parameter c in Eq. (2.56). This temperature dependence was compensated by taking the difference between resonance frequency and the undamped resonance frequency in air ($f_{0,air}$), at which the parameter c is the same.

Thus, the fluid density can be described by the parameter Δf_0:

$$\Delta f_0 = f_{0,air} - \left(f_0 + \frac{\Gamma}{2}\right) \tag{2.57}$$

where f_0 is the resonance frequency; Γ is the bandwidth; and $f_{0,air}$ is the resonance frequency of the sensor in air. To describe the fluid viscosity, we discuss an additional parameter in Section 2.3.2.

2.3.2 Viscosity measurement

For many resonance sensors, the bandwidth divided by the resonance frequency, i.e. normalized bandwidth Γ/f_0, can be correlated directly to the viscosity-density product of the fluid. In a single-degree-of-freedom resonator, the normalized damping is equal to the ratio of the stored energy and energy dissipation per cycle. This ratio can be approximated by the ratio between the fluid damping and

the inertial mass J. If we assume that J is constant, then Γ/f_0 is proportional to the square root of the product of fluid viscosity and density (applying the model described in Section 2.2.2). In case the fluid adds inertial mass or changes the modal function, the inertial mass J of the single-degree-of-freedom system is changed. This creates a fluid density dependence on the normalized bandwidth because of changes in the inertial mass of the single-degree-of-freedom resonator. To compensate for this density dependence, the expression Γ/f_0 is multiplied by the inertial mass J, which produces an indicator for the damping term of the single-degree-of-freedom system.

The inertial mass of the corresponding single-degree-of-freedom system cannot be measured directly. However, it can be determined mathematically by dividing the resonance frequency by its derivative with respect to the inertial mass:

$$-2J = \frac{f_0}{\frac{\partial f_0}{\partial J}} \tag{2.58}$$

where f_0 is the resonance frequency.

Also, the derivative $(\partial f_0)/\partial J$ cannot be measured directly. In a good approximation, the first-order derivative has the following proportionality:

$$\frac{\partial f_0}{\partial J} \sim \propto \frac{\partial f_0}{\partial \rho} \tag{2.59}$$

where ρ is the fluid density. By substituting Eq. (2.57) in Eq. (2.59) and assuming a low fluid viscosity (i.e., a small bandwidth $\Gamma \approx 0\ Hz$), we obtain Eq. (2.60).

$$\frac{\partial f_0}{\partial \rho} = \frac{\partial(\Delta f_0)}{\partial \rho} \tag{2.60}$$

This assumption implies that the inertial mass can be described as:

$$J = J_0 + c_3 \cdot \rho \tag{2.61}$$

Here, the inertial mass is assumed to be a linear function of the density $J_0 + c_3\rho$, where c_3 is a constant. Then, the proportionality of $(\partial f_0)/\partial\rho$ and $(\partial f_0)/\partial J$ can be shown by using the following chain rule:

$$\frac{\partial f_0}{\partial J} = \frac{\partial f_0}{\partial \rho}\frac{\partial \rho}{\partial J} = \frac{\partial f_0}{\partial \rho}\frac{-J_0}{c_3} \propto \frac{\partial f_0}{\partial \rho} \tag{2.62}$$

Therefore, based on the presented derivation, the parameter Γ^+ should be only be dependent on the product of viscosity and denisty of the fluid. We have Eq. (2.63).

$$\Gamma^+ = \frac{\Gamma}{f_0} \cdot \frac{f_0}{\frac{\partial f_0}{\partial \rho}} = \frac{\Gamma}{\frac{\partial(\Delta f_0)}{\partial \rho}} \tag{2.63}$$

To determine whether the parameters Γ^+ and Δf_0 exhibit any reciprocal effects of viscosity and density, experimental protocols needed to be designed to detect the exact parameters, as discussed in Section 2.3.3.

2.3.3 Identifying cross sensitivities

Experiments need to be conducted to experimentally determine the bandwidth and resonance frequencies at given temperatures, viscosities and densities. Therefore, the resonance frequency $f_{0,air}$

and bandwidth Γ_{air} of the resonator were first measured in air, where there is minimal interaction between resonator and the surrounding environment. The measured bandwidth in air Γ_{air} is a measure of the intrinsic damping of the resonator d_0, see section 2.2.1. Once the resonator is in contract with a liquid, the bandwidth and resonance frequency changes. The change in bandwidth due to the interaction of the resonator with the fluid is obtained by subtracting the bandwidth in air Γ_{air} from the measured bandwidth Γ_m, i.e. $\Gamma = \Gamma_m - \Gamma_{air}$. Therefore, Γ is a measure of the change in bandwidth due to the fluid interaction, i.e. it relates to d_f.

The fluids used in this study were Newtonian with the precise values of the viscosity and density known at a given temperature. The typical fluids that satisfied the above criterions included NIST traceable viscosity reference fluids that are available for different viscosity ranges (N2, S600, N100, S200) and pure substances such as chloroform ($CHCl_3$), acetone, and n-dodecane. Figure 7 shows the viscosity (a) and the density (b) of the fluids used in this study depending on their temperature.

To ensure that the sensor predicts the same viscosity or density regardless of the fluid temperature, density, and viscosity, the potential cross sensitivities were identified. Fluids were selected such that their densities and viscosities overlapped over segments of the desired range of temperature measurements. This allowed cross measuring (e.g., measuring viscosities at different temperatures and densities) and subsequent identification of potential cross sensitivities among the fluid properties.

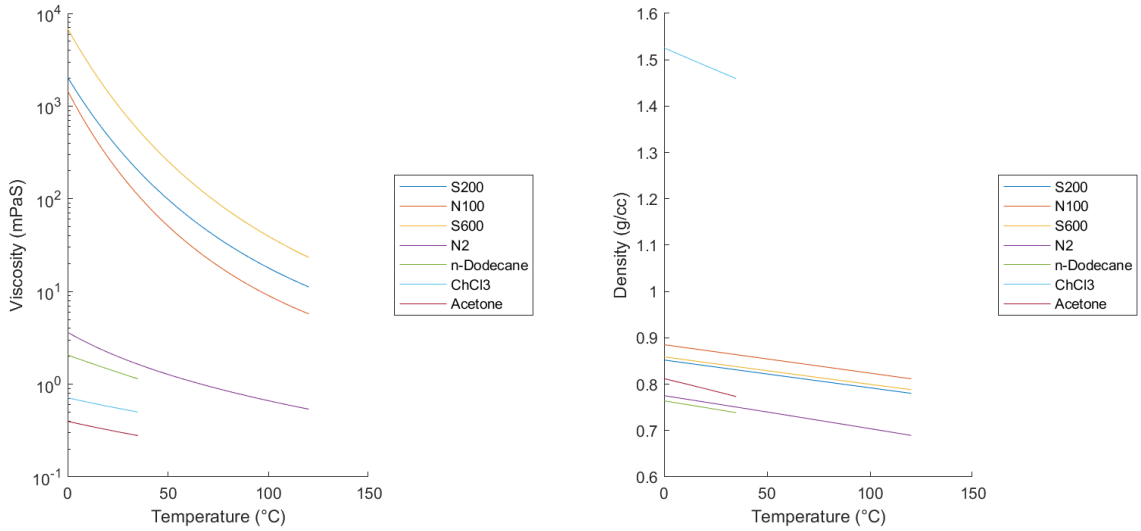

(**a**) (**b**)

Figure 7: Viscosities (a) and fluid densities (ab) versus temperature

3 Results and Discussions

This Section discusses the results of the papers with regard to the RQs I–IV. In Paper I, a new viscosity–density sensor is presented (see Section 3.1). The same sensor is then numerically investigated in Papers II and III. Paper II presents a new mathematical model that combines a mass–spring system with CFD (see Section 3.2). The numerical flow simulation is investigated in Paper III (see Section 3.3). In Paper IV, a new non-intrusive sensor is presented, which can measure the product of the fluid's viscosity and density (see Section 3.4). In section 3.5, the results are summarized and discussed in conjuncture with the RQs.

3.1 Paper I

Viscosity–Density Sensor Based on Torsional Vibrations

J. Goodbread[3], D. Brunner[1,2], K. Häusler[3], S. Kumar[3], H. Khawaja[2]

Manuscript ready

1. ZHAW, Zurich University of Applied Sciences, Switzerland
2. UIT, The Arctic University of Norway
3. Rheoncis GmbH, Switzerland

This study discusses a new sensor for measuring the viscosity and density of Newtonian fluids. The sensor's design is based on the symmetric torsional resonator first described by Goodbread et al. [32] (see Figure 8). The resonator consists of two ends that are connected to a central disk. One end, which contains a permanent magnet, is used for exciting and sensing the resonator's motions. The other end has four radial fins and is immersed into the fluid. Each end is connected to the central disk by an elastic tube, and the ends are connected with each other by a coaxially located torsional spring (not shown in Figure 8). The torsional spring couples the vibrations of the two ends, making them oscillate at the same frequency.

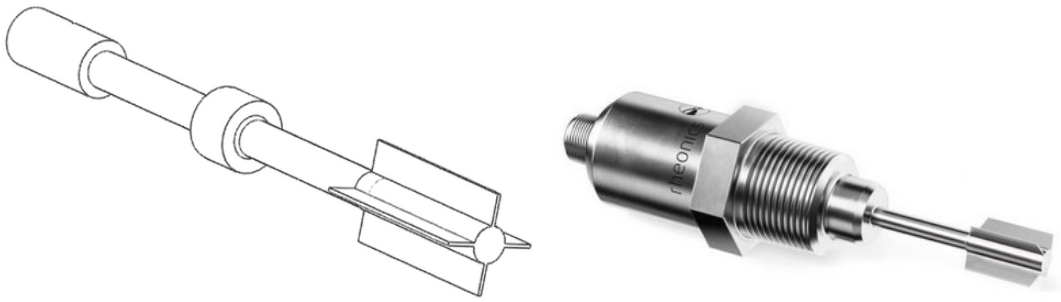

Figure 8: Schematic of the resonator (left) and sensor (right)

The properties measured by the sensor are the resonator's bandwidth, resonance frequency, and temperature. To predict the viscosity and density based on these three measured quantities, parameters were required to describe the viscosity and density with minimal reciprocal effects. In this research, the two derived parameters were mainly dependent on either the viscosity or the density. The parameters were derived based on the underlying principles of a resonance sensor, that is, a single-degree-of-freedom system (see Section 2.1). The two parameters Γ^+(Eq. (2.63)) and Δf_0 (Eq. (2.57)) describe the fluid's viscosity–density product and density, respectively. The derivation of these parameters has been discussed in Section 2.3.

The Δf_0 value was measured for different fluids over a range of temperatures, viscosities, and densities, as shown in Figure 9. All the points tended to converge to one curve, which implied that the parameter Δf_0 was a function only of the fluid density. Therefore, there is no need for complex multi-dimensional correlation functions, and the fluid density can be directly determined based on the Δf_0 value.

To model the correlation between Δf_0 and ρ, a purely empirical model (e.g., a polynomial) is unsuitable because the measurements are clustered rather than uniformly distributed; the interpolation between the clusters is unreliable. A more robust interpolation method is to use a basis function that reflects the basic properties of the sensor. This basis function results from the model presented in Paper II and is multiplied by another function to fit the experimental data shown in Figure 9 as a black line. This multiplier function only accounts for small deviation between basis function and experiments, which minimizes the empirical correction. The resulting fitting function (black line) would be straight for a single-degree-of-freedom model. However, the model predictions and the experimental results confirmed a non-linear relationship between the Δf_0 value and fluid density. At high densities, the slope of the curve decreases with respect to the fluid density. This change is caused by the distortion of the modal function, which decreases the absolute sensitivity to high densities.

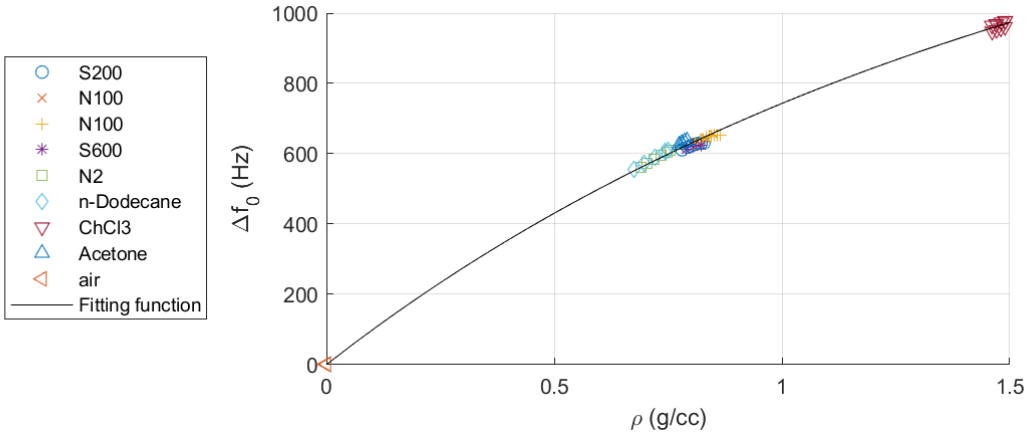

Figure 9: The Δf_0 values for experiments and the fitting function for different fluid properties and temperatures.

Fluid damping is typically correlated to the viscosity–density product of the fluid. To measure the fluid viscosity, the fluid density is first determined, then the viscosity value is computed. Figure 10 shows the measured Γ^+ values of the fluids at different temperatures, viscosities, and densities. By plotting the viscosity–density product versus Γ^+ (see Eq. (63)), all the points collapse onto one curve, which indicates that the parameter Γ^+ is only a function of the viscosity–density product (see black line in Figure 10, fitting function). Thus, thus Γ^+ is independent of fluid temperature and density.

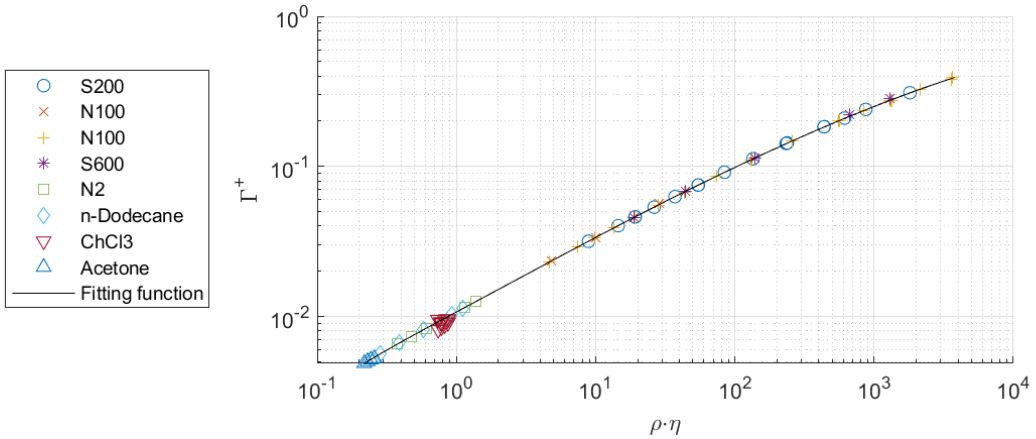

Figure 10: Viscosity–density product vs. normalized and density-corrected bandwidths for different fluids and temperatures

Experiments demonstrated that the sensor can measure fluid viscosities from less than 1 mPas up to 4000 mPas and densities from 600 kg/m³ to 1500 kg/m³ at temperatures between 0 °C and 120 °C. Both viscosity and density could be directly correlated to the two parameters $\Gamma^+$and $\Delta f_0$with minimal cross-sensitivity.

To gain a deeper understanding of the resonator that goes beyond empirical and single-degree-of-freedom models, predictive models are required that fully describe the sensor. Based on such models, the bandwidth and resonance frequency of the sensor can be predicted before it is manufactured. Such a model is presented in Paper II.

3.2 Paper 2

Modelling a Viscosity–Density Sensor Based on Small Amplitude Torsional Vibrations

D. Brunner[1,2], J. Goodbread[3], K. Häusler[3], S. Kumar[3], G. Boiger[1], H. Khawaja[2]

Manuscript ready

1. ZHAW, Zurich University of Applied Sciences, Switzerland
2. UIT, The Arctic University of Norway
3. Rheoncis GmbH, Switzerland

The mathematical model proposed in this study describes the fluid–structure interactions of the viscosity–density sensor presented in Paper I. The resonant element of the sensor is comprised of a two-mass, three-spring system. The model of the resonator describes the angular deflections of the two inertial masses J_1 and J_2, which are connected to the fixed point via the springs c_1 and are directly connected with the inner rod c_2. This modelling approach was discussed in general terms as a multi-degree-of-freedom system in section 2.1.2 and is applied on the viscosity-density sensor as a two-degrees-of-freedom system.

The schematic of the resonator and its modal function are shown in Figure 11; the blue lines show the angular deflection of the springs c_1, and the pink line shows the angular deflection of the inner rod c_2.

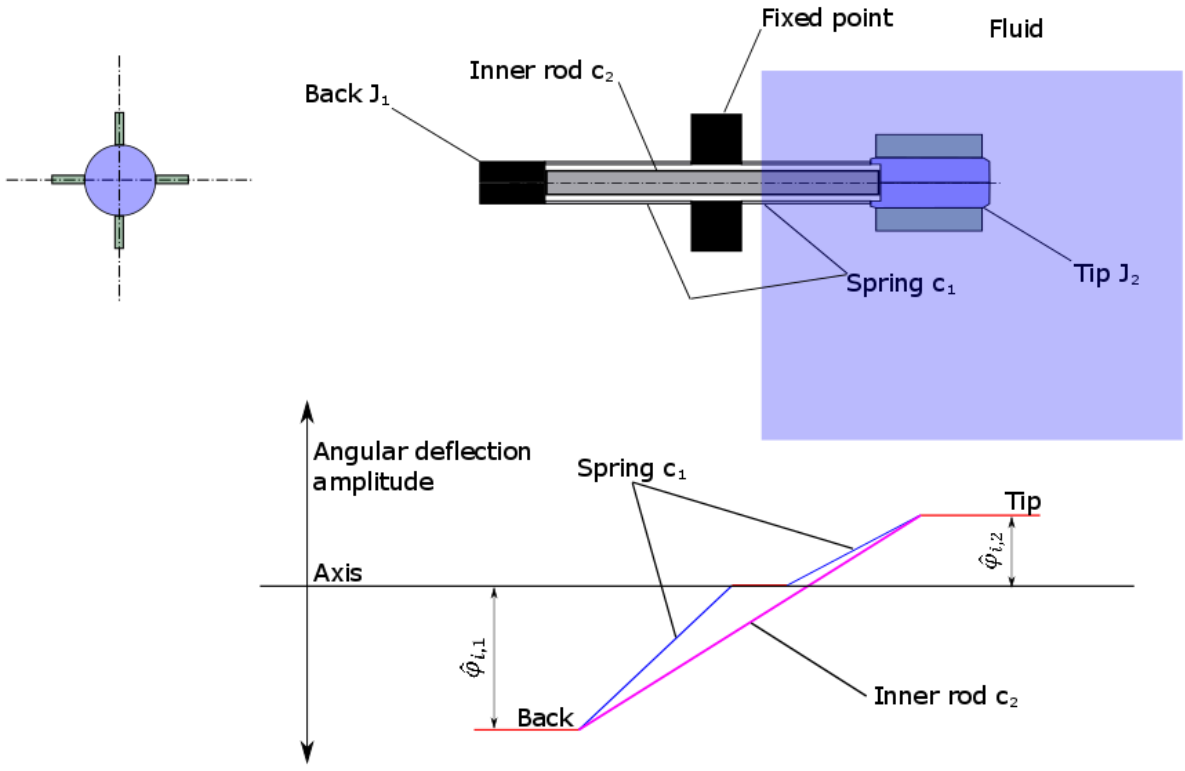

Figure 11: Schematic of the sensor (above) and modal function (below), where the red line shows the angular deflection amplitude of the tip $\hat{\varphi}_{i,1}$ and the back $\hat{\varphi}_{i,2}$. The blue line shows the deflection amplitude of the springs c_1, and the pink line shows the angular deflection amplitude of the inner rod c_2.

The fluid–structure interaction is modeled by the damping term d_f and inertial mass J_f. These two terms were imposed on the tip. The viscous damping d_f and inertial mass J_f have been discussed in Section 2.2.1 and were derived based on two solutions of the fluid mechanics equations. The flow field around

the tip with the four radial fins was modeled using CFD (see Section 2.2.4), and the cylindrical section was modeled using a flat plate approach (see Section 2.2.2).

Based on the flow simulations, the values for the damping d_f and inertial mass of the fluid J_f were computed for various angular frequencies, viscosities and densities. Figure 12 shows J_f (a) and d_f (b) as functions of the boundary layer thickness δ (see Eq. (2.43)). The inertial mass J_f was normalized by the fluid density ρ, and the fluid damping d_f was normalized by $\sqrt{\eta\rho\omega}$. The normalization made all the points collapse onto one line, which was modeled through a polynomial fit, that is, an empirical model.

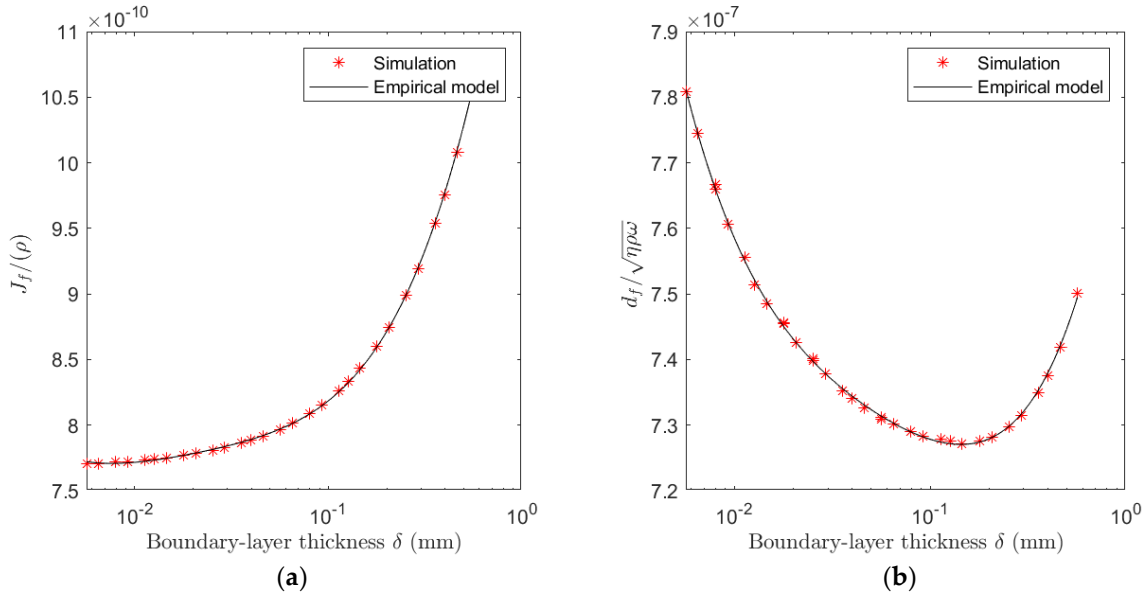

Figure 12: Normalized inertial mass of the fluid J_f as a function of the boundary-layer thickness δ (a) and the normalized damping term d_f as a function of the boundary-layer thickness δ (b)

To validate the model's predictions, the numerical results were compared with the experimental results presented in Paper I. This comparison was performed in two steps. First, the predicted and measured resonance frequencies were compared. Then the inertial masses of the model were refined to minimize the difference between measured and predicted resonance frequency by means of the least square method. The relative deviations between these fitted inertial masses and the inertial masses estimated from the dimensions of the sensor were less than 5 %. This low deviation confirmed the plausibility of the fitted inertial masses. The predicted and measured resonance frequencies at different temperatures, fluid densities and viscosities are shown in Figure 13.

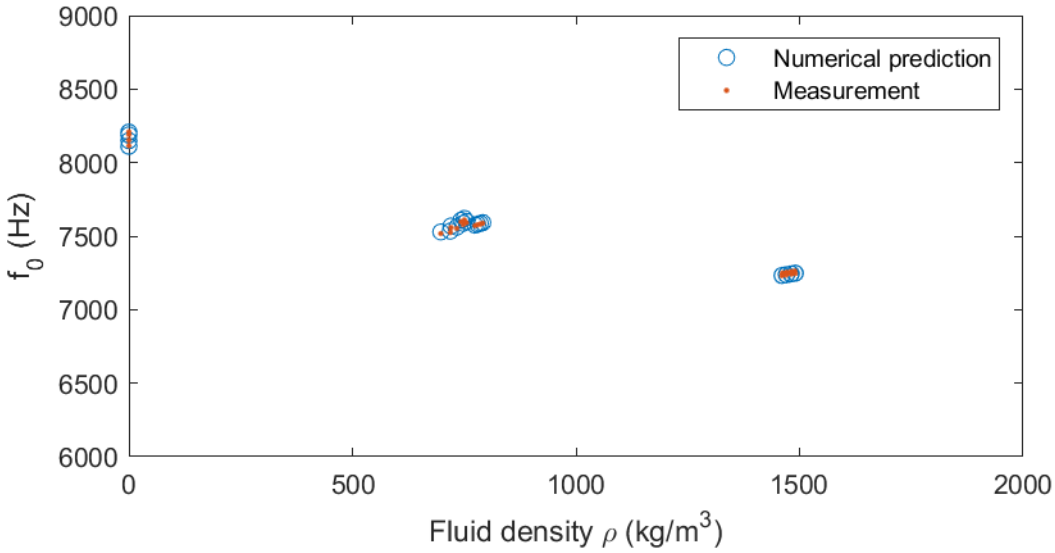

Figure 13: Comparison of the predicted and computed resonance frequencies f_0 at different fluid densities, viscosities, and temperatures

In the second step, this refined model was further validated based on the predicted normalized bandwidth Γ/f_0 (bandwidth divided by the resonance frequency). Figure 14 shows Γ/f_0 versus the viscosity–density products of the fluids for both the experimental results and numerical predictions. Most of the fluids had fluid densities between 650 kg/m³ and 900 kg/m³, as shown by the color bar. The fluid density of $CHCl_3$ (not shown in the color bar in Figure 14) was approximately 1480 kg/m³ (temperature dependent). The normalized bandwidth of $CHCl_3$ was approximately 40 % lower than that for fluids with densities between 650 kg/m³ and 900 kg/m³. This effect did not originate from a low damping coefficient d_f but from a change in the amplitude ratio between tip and back, because of the high fluid density. The high fluid density increased the inertial mass of the tip; therefore, the angular deflection amplitude of the back increased. This changed the balance between the inertial and damping forces of the system; therefore, the normalized bandwidth was reduced.

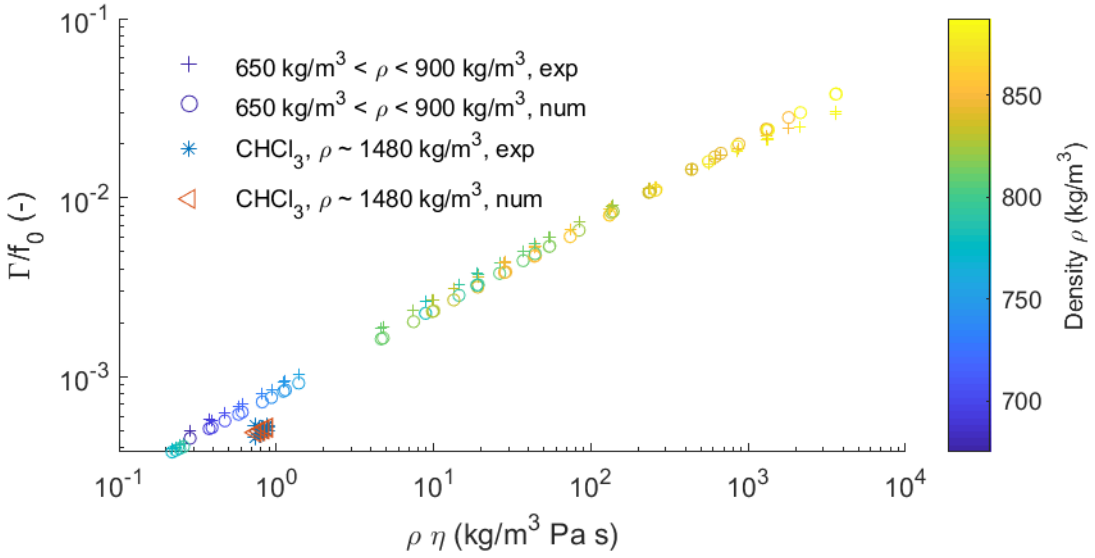

Figure 14: Comparison between the predicted and measure normalized bandwidths Γ/f_0 for different viscosity–density products. Γ is the bandwidth; f_0 is the resonance frequency; ρ is the fluid density; and η is the dynamic viscosity.

Figure 15 shows the relative deviation from the predicted and measured normalized bandwidths. For viscosities less than 100 mPas (at the reference density of 1000 kg/m³), there was constant offset between the model and predictions. For viscosities higher than 100 mPas, the numerical model systematically deviated and predicted higher bandwidths than those observed experimentally. A potential source of the deviations an the edge effects at the tip, which were neglected by reducing the computational domain into a cross section. Including these edge effects in a three-dimensional domain can be investigated in future studies.

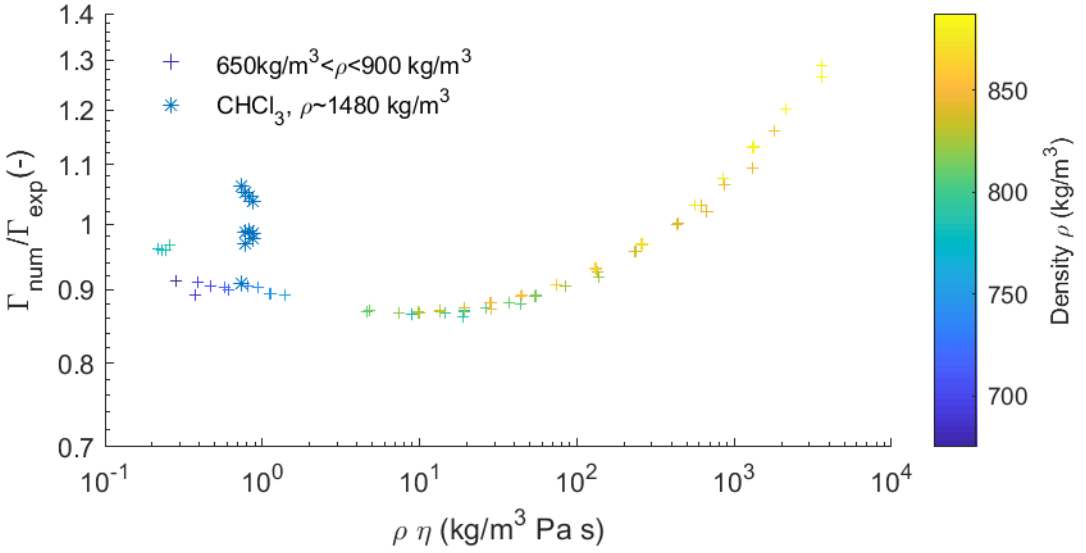

Figure 15: Relative deviations between the predicted and measured normalized bandwidths Γ/f_0 for different viscosity–density products. Here, Γ is the bandwidth; f_0 is the resonance frequency; ρ is the fluid density; and η is the dynamic viscosity.

The proposed model has proven to efficiently and accurately predict the behavior of the viscosity–density sensor. Thus, the model allows for computationally supported geometrical optimization, and it has the potential to significantly decrease the development time of a new generation of sensors.

However, the model has only been validated for integrated quantities, such as the normalized bandwidth and resonance frequencies. To further validate the numerical part of the model and increase the credibility of the obtained solutions, a comparison of the local quantities (pressures and shear rates at the boundary of the structure) is required (see Paper III).

3.3 Paper 3

CFD Modeling of Pressure and Shear Rate in Torsionally Vibrating Structures using ANSYS CFX and COMSOL Multiphysics

D. Brunner[1,2], H. Khawaja[2], M. Moatamedi[2], G. Boiger[1]

The International Journal of Multiphysics, Vol. 12, no. 4, pp. 349–358, 2018.

1. ZHAW, Zurich University of Applied Sciences, Switzerland
2. UIT, The Arctic University of Norway

In the paper II, a model was presented to predict the bandwidth and resonance frequency of a torsional resonator. The damping term d_f and inertial mass of the fluid J_f were determined using CFD. The results were validated only on integrated quantities, i.e. bandwidth and resonance frequency. Therefore, a more in-depth investigation of the numerical flow simulation is required to ensure the validity of the numerical flow solution.

To increase confidence in the solution of the velocity and pressure fields, it needs to be shown that the solution is independent of the numerical method and the method in which the oscillation is applied. This was achieved by comparing the solutions of the velocity and pressure fields in two commercial software:

- COMSOL Multiphysics® (based on the finite element method)
- ANSYS CFX® (based on the finite volume method)

The two methods, finite element and finite volume, have been discussed in Section 2.2.4.

Motion is induced differently in the two programs; therefore, a comparison would reflect the correctness of the models and their suitability for the solution. COMSOL Multiphysics® uses a moving wall approach, whereas ANSYS CFX® induces motion in the domain by using a frame of reference approach.

The following cases were compared:

- Moving wall approach, COMSOL Multiphysics®
  The moving wall applied the torsional oscillation motion via a boundary velocity (see Eq. (2.52) in Section 2.2.4).
  The equations of fluid mechanics have been solved (see Eqs. (2.50) and (2.51)).

- Linearized moving wall approach, COMSOL Multiphysics®
  The moving wall applied the torsional oscillation motion via a boundary velocity (see Eq. (2.53) in Section 2.2.4).
  The equations of fluid mechanics have been solved in their linearized form, that is, the convection was neglected (see Eqs. (2.50) and (2.52)).

- Frame of reference approach, ANSYS CFX®
  Instead of creating the motion at the structure, a frame of reference was applied in the flow field. Thereby, additional terms were added to Eq. (2.51), namely, centrifugal acceleration, Coriolis acceleration, and Euler acceleration (see Eq. (2.54)).

The solutions of the shear rates and pressures on the boundaries were compared. These quantities were chosen because they were needed to determine integrated torques (Eqs. (2.32) and (2.33)) to compute the inertial mass of the fluid J_f and the damping term d_f.
This paper investigates the geometry of the tip of the viscosity–density sensor presented in Paper I. The tip was divided into three sections: radial, fin, and tip (see Figure 16).

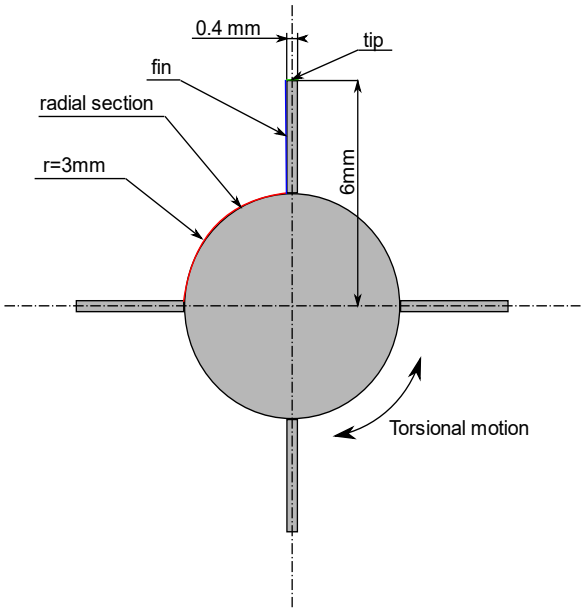

Figure 16: Geometry of the sensor tip of a viscosity–density sensor

The shear rates and pressure values computed by the different methods were compared at these three geometrical sections. After reaching the quasi-steady-state, the shear rate and pressure were harmonic due to of the harmonic oscillation of the structure. Thus, the shear rate and pressure were compared in terms of their amplitude and phase. Figure 17 shows the shear rate amplitude for two fluid viscosities and three numerical methods. The solutions for all the methods were found to be in good agreement.

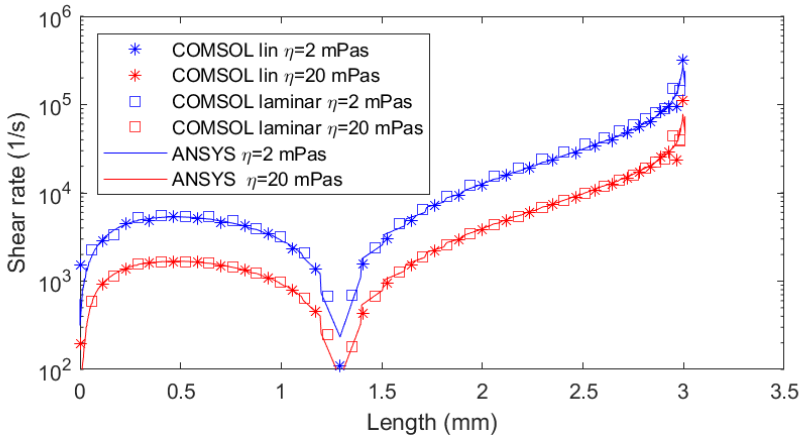

Figure 17: Comparison of shear rate amplitudes over the fin between COMSOL Multiphysics® (full and linearized version of fluid mechanics equations) and ANSYS CFX®

Figure 18 shows the pressure amplitude, and Figure 19 shows the phase of the pressure for the radial section. The pressure and phase were only plotted for a dynamic viscosity of 2 mPas since the solutions were almost identical to those at 20 mPas. For all the methods, the pressure amplitude was reduced strongly in the center of the radial section. At the same location, the pressure phase switched from slightly above 0° to almost 180°, which indicated that the pressure field was asymmetric. For both the phase and amplitude, all the three methods were in good agreement.

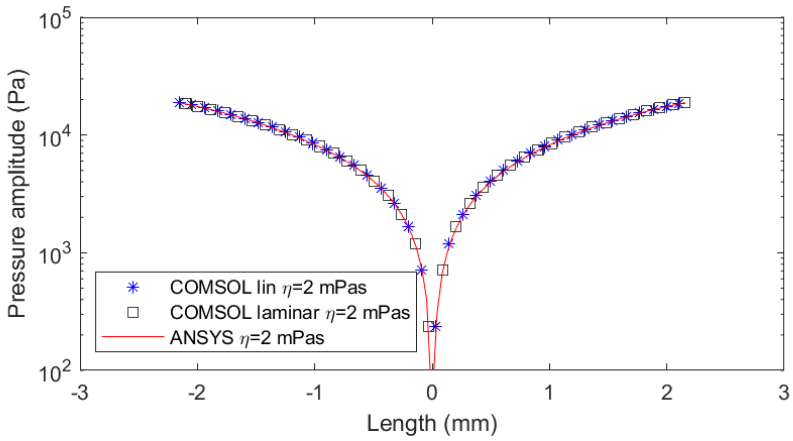

Figure 18: Comparison of the pressure amplitude over the radial section between COMSOL Multiphysics (full and linearized version of the Navier–Stokes equation) and ANSYS CFX

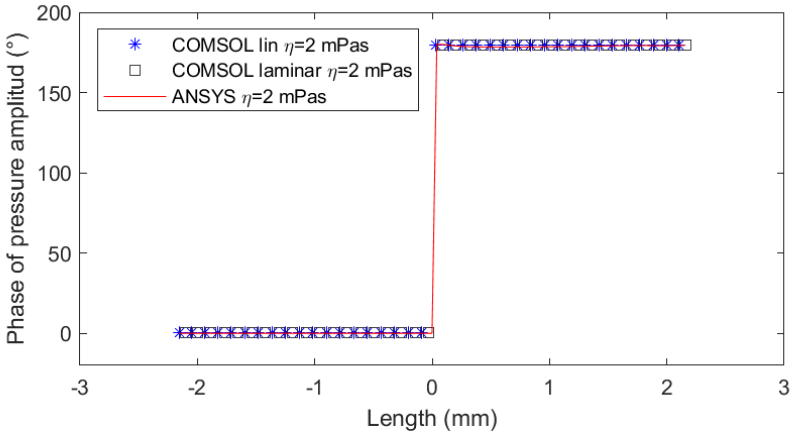

Figure 19: Comparison of the phase of the pressure over the radial section between COMSOL Multiphysics (full and linearized version of the Navier–Stokes equation) and ANSYS CFX

All the numerical models yielded the same solution; therefore, the solution was independent of the numerical method and how the motion was applied. This underlines the potential of CFD for investigating the fluid mechanism around a torsional resonator (i.e., the viscosity–density sensor).

In Papers I–III, a probe-style viscosity–density sensor was investigated. Probe-style sensors have limited applications for the real-time measurement of viscosity in industrial processes because they create an obstruction in the piping systems. Such obstructions can be problematic in biochemical processes and cleaning-in-place procedures. Therefore, a non-intrusive viscosity sensor is presented in Paper IV.

3.4 Paper 4

Analysis of a Tubular Torsionally Resonating Viscosity-Density Sensor
D. Brunner[1,2], J. Goodbread[3], K. Häusler[3], S. Kumar[3], G. Boiger[1], H. Khawaja[2],
MDPI Sensors, 2020, 20 (11), 3036. https://doi.org/10.3390/s20113036.
1. ZHAW, Zurich University of Applied Sciences, Switzerland
2. UIT, The Arctic University of Norway
3. Rheoncis GmbH, Switzerland

In this research, we propose a new tubular sensor that can measure the product of the fluid viscosity and density under conditions of internal flow. The sensor comprises of a straight, thin walled, stainless-steel tubular body; the flow passes through the sensor body without any interruption. This allows the tubular sensor to be directly integrated into a process line.

The working principle of the tubular sensor is based on torsional resonance. The first torsional mode of the resonator was excited at a frequency close to its natural frequency. The excited resonance created motion in the fluid. The shear stresses caused by the fluid motion induced a torque on the sensor, which dampened the resonator's oscillation. The damping of the oscillation can be measured by a bandwidth and related to the viscosity–density product of the fluid.

Figure 20 shows the schematic of the tubular sensor. The resonator consists of a tube and two large decoupling disks mounted onto the outer diameter. The first torsional mode was excited between the two masses via two permanent magnets that were mounted onto the tube. These magnets were driven by electromagnets, which produced an oscillating torque near the natural frequency of the first torsional mode. This driving torque was turned off after sufficient energy had been provided to the resonator. Then, the decay in the torsional oscillation was measured using electromagnets. Based on the measured signal, the bandwidth Γ and resonance frequency f_0 were computed.

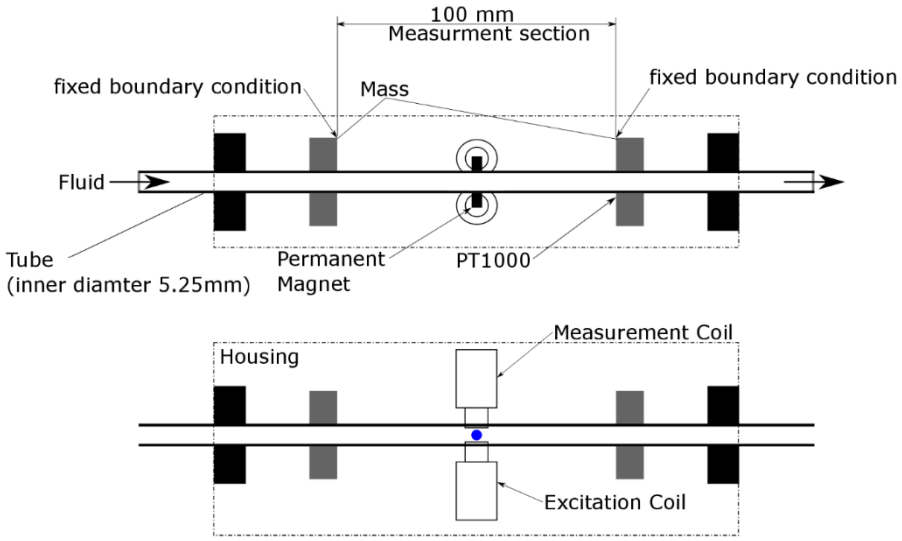

Figure 20: Experimental setup of the tubular sensor

Appropriate models are required to numerically predict the bandwidth and resonance frequency. The sensor was modeled based on a continuous resonator; only the first torsional mode was considered. The modal analysis of a continuous tubular sensor has been discussed in Section 2.1.3. Based on this modal analysis, the first torsional mode could be described by a single-degree-of-freedom system (see Section

2.1.1). Therefore, the representative inertial mass and spring constant of the single-degree-of-freedom system were determined (see Eqs. (2.28) and (2.29)). The fluid damping was computed based on an analytical solution of the flow on cylindrical structures, as discussed in Section 2.2.3.

Experiments were performed to validate the predictions of the numerical models and test the capabilities of the sensors. These experiments were conducted in two steps:

- First, the sensor was tested under well-defined conditions without any internal flow, that is, the temperature, viscosity, and density were known and controlled. NIST traceable viscosity reference fluids (N2, S6, S20, S60, N100, S200, and S600) were used.
- Second, the sensor was placed in a flow loop at room temperature to investigate the sensitivity of the measurement of the viscosity–density product on the internal flow at Reynolds numbers ranging from 500 to 50,000.

Figure 21 shows the product of fluid viscosity and density ($\rho\eta$) versus the normalized bandwidth Γ/f_0. The colormap shows the temperatures at which the $\rho\eta$-values were measured. Overall, the normalized bandwidth was proportional to the square root of the $\rho\eta$-value. This proportionality is typical for resonance sensors and was also observed for the viscosity–density sensor discussed in Papers I–III. Also, no significant trends were found in the measured normalized bandwidth with respect to temperature; therefore, the measured normalized bandwidth was independent of the temperature.

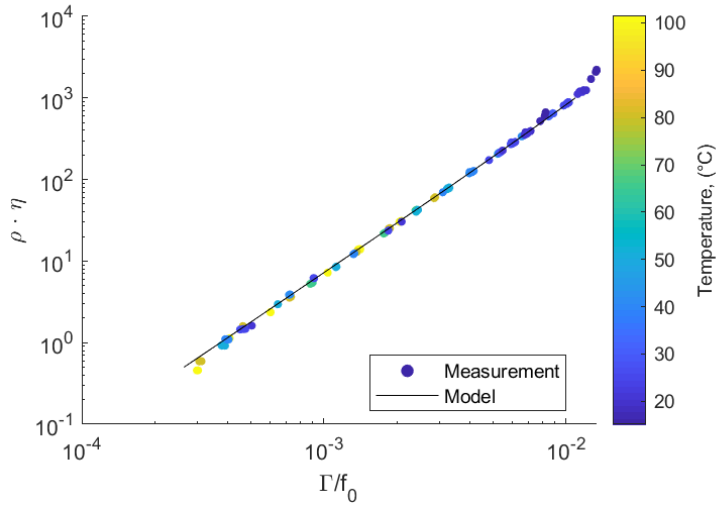

Figure 21: Comparison between the numerical prediction and experimental results for different fluids and temperatures

The model predicts the $\rho\eta$-value for a given normalized bandwidth, as shown in Figure 21 (black line). The predictions had the same order of magnitude and showed the same trend as the experiments. This indicates that the model captured the primary effects of the resonator. However, the experimental results deviated from the model at high viscosities. This deviation is more evident in Figure 22, where the relative deviation between the numerical prediction and experiment measurement is shown. Despite the good agreement among the overall trends, the predictions systematically differed for high $\rho\eta$-values. At low $\rho\eta$-values, there was constant offset between the numerical predictions and experimental results, which could be explained by the manufacturing tolerances. However, at high $\rho\eta$-value (i.e., high damping), systematic deviations were observed in the trend. This systematic deviation was statistically significant and could be caused by an effect that was not incorporated into the model. The potential sources of deviation included a bias on the bandwidth measurement or a distortion of the modal function.

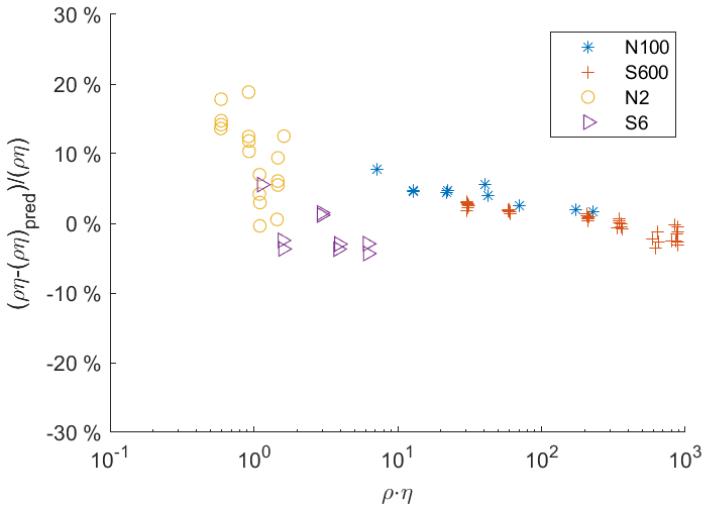

Figure 22: Relative deviations in the viscosity–density product predictions from the numerical model when compared with the actual model for different fluids.

To predict the $\rho\eta$-value based on the measured bandwidth without the systematic error, the prediction must be corrected. This was achieved by multiplying the prediction by an empirical correction function. This correction function accounts for the systematic deviations and was based on the experiments shown in Figure 22. The validity of this corrected prediction model was tested using two additional fluids, which were not used to create the correction function. The relative deviation between the predicted and measured $\rho\eta$-value is shown in Figure 23. The deviation of the measured $\rho\eta$-value from the predicted value was within the 95 % confidence level of the measurement. Therefore, the prediction was verified.

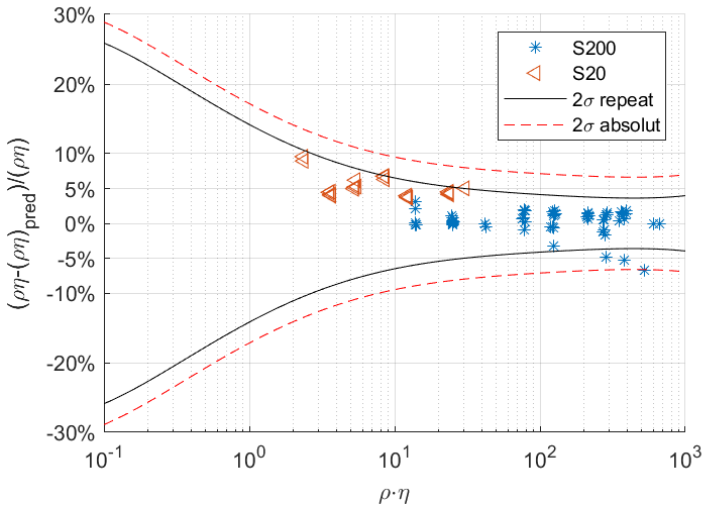

Figure 23 Relative deviation in the product of fluid viscosity and density prediction from the corrected numerical model to the actual product of fluid viscosity and density for S20 and S200, including the double standard-deviation (2) confidence interval.

To determine the impact of a superimposed flow, the measurements at different Reynolds numbers were compared with the static conditions. This enabled the investigation of the interactions between the vibration-induced flow and the flow passing through the tube. Figure 24 shows the relative deviations of the predicted viscosity between the static conditions and internal flows at different Reynolds numbers. Most deviations were below ±1 %. This value is below the confidence interval for repeatability, and the data was randomly spread; therefore, the internal flow does not significantly affect the viscosity measurements for Reynolds numbers below 50,000.

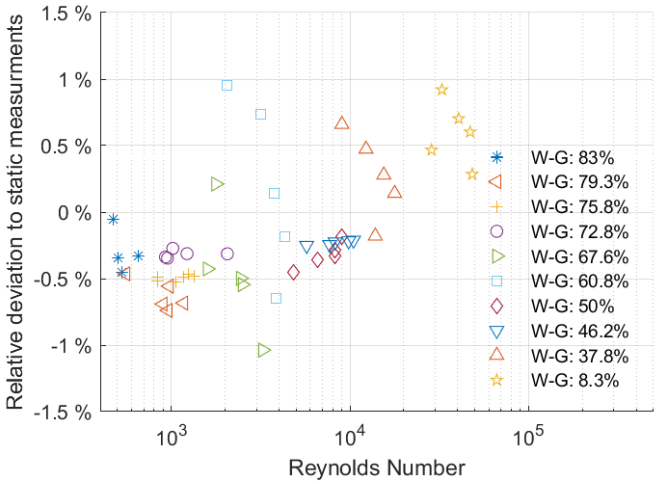

Figure 24: Relative deviations of viscosity predictions at different Reynolds numbers and static measurements

Overall, the tubular sensor showed good potential for applications in industrial processes. The sensor could accurately measure the $\rho\eta$-value of a fluid under static conditions and internal flow conditions. However, further studies are required to clarify the deviations of the prediction from the real sensor behaviors at high viscosities. This could be achieved by using strong fluid–structure interaction to consider the potential effects of the modal distortions caused by high fluid viscosities.

3.5 Summary

In Sections 3.1 to 3.4, the results of the research papers were discussed. Section 3.5 aims to answer the RQs in conjunction with the research papers. Furthermore, the relationship between the RQs and research papers are summarized in Table 1. The details given in Table 1 are visually illustrated in Figure 25.

RQ I: What is the underlying physics of torsional resonators in the context of viscosity and density measurement applications?

RQ I was mainly addressed in three papers: I, II, and IV. Paper I investigated a fluid viscosity–density sensor using experiments. In Paper II, a comprehensive numerical model was presented that could be used to predict the bandwidth and resonance frequency of the sensor based on the fluid properties. The predictions were compared against the experimental results presented in Paper I. In Paper IV, a new continuous resonator was presented. This study combined both intense modeling and extensive experimental investigations.

RQ II: Are reduced-order models suitable for coupling the flow simulations with resonator models?

Reduced-order modeling has proven to be a viable tool to model torsional resonators. Papers I, II, and IV used reduced-order modeling in different variations. Therefore, it has been demonstrated that reduced-order models are suitable for describing the interactions between fluids and resonators.

RQ III: How can CFD be used to compute the flow field around a torsional oscillating structure?

CFD was used to compute the flow around a torsionally oscillating structure in Paper II and Paper III. Paper II discussed a method to efficiently couple the flow simulation solution with the model of the resonator. In Paper III, an in-depth investigation on the method of the solution was presented, wherein it was demonstrated that the solution is independent of the numerical method and boundary conditions. Thus, CFD was successfully used to compute the flow field around the torsionally oscillating structures to determine the inertial mass and damping caused by the fluid.

RQ IV: How can we compensate for the cross sensitivities among the fluid viscosity, density, and temperature?

Reducing cross sensitivities is essential to accurately predict the viscosity or the density. In Paper I, the approach of using two parameters that were mainly functions of either the viscosity or the density was discussed. Therefore, it was shown that the parameters can be used to compensate the reciprocal effects between the viscosity and density. These parameters were based on a simple mass–spring system. However, the assumptions were motivated by the comprehensive model presented in Paper II.

Table 1: Research papers and correlation to the RQs

Research questions (RQs)	Paper I	Paper II	Paper III	Paper IV
RQ I: What is the underlying physics of torsional resonators in the context of viscosity and density measurement applications?	+++	+++	++	+++
RQ II: Are reduced-order models suitable for coupling the flow simulations with resonator models?	++	+++	+	+++
RQ III: How can CFD be used to compute the flow field around a torsional oscillating structure?	+	+++	+++	+
RQ IV: How can we compensate for cross sensitivities among the fluid viscosity, density, and temperature?	+++	++	+	++

Note. The + sign denotes a weak connection; ++ specifies a medium connection, and +++ specifies a strong connection.

Figure 25: Correlations among the papers and research questions.

4 Research Contributions and Future Work

4.1 Research contributions

The study makes the following scientific contributions:

- Different mathematical approaches were investigated to compute the boundary force on the vibrating structures using CFD. It was demonstrated that vibrations can be induced by different methods without affecting the solution.

- The solution obtained by a CFD-simulation was successfully coupled with a structural model of the resonator. This was achieved by computing damping and inertial mass terms through CFD, which were then used in the structural model to account for the fluid interaction. This allows the prediction of the resonator's bandwidth and resonance frequency when the fluid's viscosity and density are known.

- A new approach was presented for compensating the cross sensitivities between the viscosity and density. This was a generic method to compensate the effects caused by a change in the model function of the resonator.

- A new viscosity sensor based on a tube was presented. The sensor has the potential to be used for measuring the viscosity in-line without disturbing the flow. Also, it was demonstrated that the flow rate did not significantly impact the viscosity measurement in either the laminar or turbulent flow conditions. This implies that the flow field produced by micro-vibrations was not affected by the superimposed flow.

4.2 Suggestions for future work

In the future, research is possible in the following areas:

- CFD simulations have proven to accurately compute the flow field near a resonator element and thereby provide insights into the working principle of the resonator's interactions with the fluid. In the future, CFD can be used to study various resonator shapes, and the geometry can be optimized to increase the sensor accuracy. Further, to obtain a better agreement between the simulation and experiments, three-dimensional CFD simulations can be performed to account for the edge effects.

- Weak fluid–structure interaction is limited to geometries in which the fluid does not significantly distort the mode shape. Models having strongly coupled fluid–structure interactions enable the simulation of geometries wherein the fluid significantly changes the structure of the mode. Therefore, research is required with strongly coupled fluid structures interactions.

- A future study could include non-Newtonian and viscoelastic fluids. The challenge with both fluids is that the measured viscosity is not directly comparable with the measurements performed by using traditional laboratory devices. Therefore, it is important to understand the relationship between the viscosities measured by a resonant sensor and a traditional laboratory equipment.

Works cited

[1] B. Jakoby, R. Beigelbeck, F. Keplinger, F. Lucklum, A. Niedermayer, E.K. Reichel, C. Riesch, T. Voglhuber-Brunnmaier, B. Weiss, Miniaturized sensors for the viscosity and density of liquids - Performance and issues, IEEE Trans. Ultrason. Ferroelectr. Freq. Control. 57 (2010) 111–120. https://doi.org/10.1109/TUFFC.2010.1386.

[2] B. Jakoby, M. Scherer, M. Buskies, H. Eisenschmid, An automotive engine oil viscosity sensor, IEEE Sens. J. 3 (2003) 562–568. https://doi.org/10.1109/JSEN.2003.817164.

[3] A.M. Sánchez, R. Prieto, M. Laso, T. Riesgo, A piezoelectric minirheometer for measuring the viscosity of polymer microsamples, IEEE Trans. Ind. Electron. 55 (2008) 427–436. https://doi.org/10.1109/TIE.2007.910528.

[4] A. Andreotti, I. Bonaduce, M.P. Colombini, F. Modugno, E. Ribechini, C. Industriale, Combined GC / MS Analytical Procedure for the Characterization of Glycerolipid , Waxy , Resinous , and Proteinaceous Materials in a Unique Paint Microsample of lipids , waxes , proteins , and resinous materials in the, Society. 78 (2006) 4490–4500.

[5] M. Fuchs, W. Drahm, C. Matt, A. Wenger, A Coriolis meter with direct viscosity measurement, Flomeko. (2003) 1–5.

[6] M. Heinisch, T. Voglhuber-Brunnmaier, E.K. Reichel, I. Dufour, B. Jakoby, Application of resonant steel tuning forks with circular and rectangular cross sections for precise mass density and viscosity measurements, Sensors Actuators, A Phys. 226 (2015) 163–174. https://doi.org/10.1016/j.sna.2015.02.007.

[7] J. Toledo, T. Manzaneque, J. Hernando-García, J. Vázquez, A. Ababneh, H. Seidel, M. Lapuerta, J.L. Sánchez-Rojas, Application of quartz tuning forks and extensional microresonators for viscosity and density measurements in oil/fuel mixtures, in: Microsyst. Technol., 2014: pp. 945–953. https://doi.org/10.1007/s00542-014-2095-x.

[8] M. Heinisch, T. Voglhuber-Brunnmaier, E.K. Reichel, I. Dufour, B. Jakoby, Electromagnetically driven torsional resonators for viscosity and mass density sensing applications, Sensors Actuators, A Phys. 229 (2015) 182–191. https://doi.org/10.1016/j.sna.2015.03.033.

[9] T. Brack, Multi-frequency phase control of a torsional oscillator for applications in dynamic fluid sensing, ETH Zürich, 2017, PhD dissertation. https://doi.org/https://doi.org/10.3929/ethz-a-010867290.

[10] T. Brack, S. Bolisetty, J. Dual, Simultaneous and continuous measurement of shear elasticity and viscosity of liquids at multiple discrete frequencies, Rheol. Acta. 57 (2018) 415–428. https://doi.org/10.1007/s00397-018-1083-y.

[11] T. Brack, J. Dual, Multimodal torsional vibrations for the characterization of complex fluids, WIT Trans. Built Environ. 129 (2013) 191–199. https://doi.org/10.2495/FSI130171.

[12] J. Dual, Experimental methods in wave propagation in solids and dynamic viscometry, ETH Zürich, 1989, PhD dissertation.

[13] M. Heinisch, S. Clara, I. Dufour, B. Jakoby, A spiral spring resonator for mass density and viscosity measurements, Procedia Eng. 87 (2014) 1143–1146. https://doi.org/10.1016/j.proeng.2014.11.367.

[14] M. Heinisch, E.K. Reichel, I. Dufour, B. Jakoby, A U-shaped wire for viscosity and mass density

sensing, Sensors Actuators, A Phys. 214 (2014) 245–251. https://doi.org/10.1016/j.sna.2014.04.020.

[15] S. Clara, H. Antlinger, F. Feichtinger, A.O. Niedermayer, T. Voglhuber-Brunnmaier, B. Jakoby, A balanced flow-through viscosity sensor based on a torsionally resonating pipe, Proc. IEEE Sensors. 2017-Decem (2017) 1–3. https://doi.org/10.1109/ICSENS.2017.8234137.

[16] K. Häusler, W.H. Reinhart, P. Schaller, J. Dual, J. Goodbread, M. Sayir, A newly designed oscillating viscometer for blood viscosity measurements, Biorheology. 33 (1996) 397–404. https://doi.org/10.1016/0006-355X(96)00030-3.

[17] W.H. Reinhart, K. Hausler, P. Schaller, S. Erhart, M. Stetter, J. Dual, M. Sayir, Rheological properties of blood as assessed with a newly designed oscillating viscometer., Clin. Hemorheol. Microcirc. 18 (1998) 59–65.

[18] T. Brack, S. Bolisetty, J. Dual, Simultaneous and continuous measurement of shear elasticity and viscosity of liquids at multiple discrete frequencies, Rheol. Acta. 57 (2018) 415–428. https://doi.org/10.1007/s00397-018-1083-y.

[19] T. Brack, J. Dual, Multimodal torsional vibrations for the characterization of complex fluids, in: WIT Trans. Built Environ., 2013: pp. 191–199. https://doi.org/10.2495/FSI130171.

[20] D. Valtorta, E. Mazza, Dynamic measurement of soft tissue viscoelastic properties with a torsional resonator device, Med. Image Anal. 9 (2005) 481–490. https://doi.org/10.1016/j.media.2005.05.002.

[21] J. Goodbread, J. Dual, Resonant conductor measurement system and method, United States patent US 8,752,716 B2, 2014.

[22] J. Goodbread, D. Brunner, K. Haeusler, S. Kumar, A Viscosity-Density Sensor Based on Torsional Vibrations, Manuscript ready. (2020).

[23] M. Heinisch, T. Voglhuber-Brunnmaier, E.K. Reichel, I. Dufour, B. Jakoby, Reduced order models for resonant viscosity and mass density sensors, Sensors Actuators, A Phys. 220 (2014) 76–84. https://doi.org/10.1016/j.sna.2014.09.006.

[24] H. Li, J. Wang, X. Li, D. Chen, Viscosity–density sensor with resonant torsional paddle for direct detection in liquid, IET Nanobiotechnol. 5 (2011) 121–125. https://doi.org/10.1049/iet-nbt.2011.0016.

[25] N. McLoughlin, S.L. Lee, G. Hähner, Simultaneous determination of density and viscosity of liquids based on resonance curves of uncalibrated microcantilevers, Appl. Phys. Lett. 89 (2006) 184106. https://doi.org/10.1063/1.2374867.

[26] M.F. Khan, S. Schmid, P.E. Larsen, Z.J. Davis, W. Yan, E.H. Stenby, A. Boisen, Online measurement of mass density and viscosity of pL fluid samples with suspended microchannel resonator, Sensors Actuators B Chem. 185 (2013) 456–461. https://doi.org/10.1016/j.snb.2013.04.095.

[27] D. Johannsmann, The Quartz Crystal Microbalance in Soft Matter Research: Fundamentals and Modeling, 2014. https://doi.org/10.1007/978-3-319-07836-6.

[28] S. Clara, F. Feichtinger, T. Voglhuber-Brunnmaier, A.O. Niedermayer, A. Tröls, B. Jakoby, Balanced torsionally oscillating pipe used as a viscosity sensor, Meas. Sci. Technol. 30 (2019). https://doi.org/10.1088/1361-6501/aae755.

[29] N. Mahmoodi, C.J. Anthony, Air Damping Simulation of MEMS Torsional Paddle, Excerpt from Proc. 2014 COMSOL Conf. (2014) 15–18.

[30] E.K. Reichel, T. Voglhuber-Brunnmaier, B. Jakoby, Fluid Impedance Model for Resonator Viscosity Sensors, Procedia Eng. 168 (2016) 1012–1015. https://doi.org/10.1016/j.proeng.2016.11.328.

[31] H. Irretier, Grundlagen der Schwingungstechnik 2, wieweg, 2001. https://doi.org/10.1007/978-3-322-80244-6.

[32] J. Goodbread, S. Kumar, K. Häusler, B. Zybach, Temperature compensated density viscosity sensor having a resonant sensing element, United States patent US 10,502,670, 2019.

Appendix

Paper I

A Viscosity–Density Sensor Based on Torsional Vibrations

J. Goodbread[3], D. Brunner[1,2], K. Häusler[3], S. Kumar[3], H. Khawaja[2]

Manuscript ready

1. ZHAW, Zurich University of Applied Sciences, Switzerland
2. UIT, The Arctic University of Norway
3. Rheoncis GmbH, Switzerland

Author contributions:

- J. Goodbread, K. Häusler conceptualized the sensor
- J. Goodbread, D. Brunner, and H. Khawaja did the methodology
- J. Goodbread, K. Häusler did the experimental work
- D. Brunner, J. Goodbread postprocessed the experimental data
- D. Brunner prepared the draft
- J. Goodbread, S. Kumar and H. Khawaja did review and editing
- D. Brunner did the visualization
- H. Khawaja, J. Goodbread and G. Boiger did the supervision
- S. Kumar did the project administration

Organizations contributions:

- MATLAB® license was provided by ZHAW
- Sensor and experimental work were provided by Rheonics GmbH

Funding:

- This research was funded by Rheonics GmbH and Innosuisse, grant number 27254.1

A Viscosity-Density Sensor Based on Torsional Vibrations

J. Goodbread[3], D. Brunner[12], K. Häusler[3], S. Kumar[3], H. Khawaja[2]

1. ZHAW,Technikumstrasse 9, CH - 8401 Winterthur

2. UIT The Arctic University of Norway

3. Rheonics GmbH, Switzerland

joe.goodbread@rheonics.com

Abstract

This study discusses a new sensor for measuring the viscosity and density of fluids. The sensor is based on a torsional resonator having a cylindrical tip with radial fins. The interaction of the resonator with the fluid changes the its damping and resonance frequency. The change in resonance frequency and damping can be related to the fluid properties. The sensor was tested experimentally, using fluids with well-known properties. It was shown that the sensor can be used to measure fluid viscosity and density over a wide range with very high accuracy. The prediction is based on models that account for and minimize reciprocal effects between viscosity and density.

1. INTRODUCTION

The physical properties of fluids used in chemical and biochemical processes can be used as an indicator of their composition. Sensors capable of providing a real-time measurement of viscosity and density are generally based on resonant elements immersed in the fluid. In comparison to the large and delicate instruments used in laboratory rheological measurements, resonant sensors are generally compact, robust, and capable of being introduced directly into process systems. Jakoby et al.[1] reviewed a range of miniaturized sensors that measure fluid viscosity and density. These sensors make use of a variety of resonators, such as thickness shear piezoelectric elements, electromagnetic-acoustic resonators, vibrating bridge devices, double membrane devices and micromachined plate devices.

Resonant elements in these sensors are immersed in the fluid to be measured. The resonator interacts with the fluid so as to change its resonance frequency and damps its oscillation. Both resonance frequency and oscillation damping are dependent on the fluid viscosity and density. Heinisch [2] presented a reduced order model based on lumped elements, describing the correlation between damping and frequency of a mechanical resonator with respect to fluid properties.

Typical resonant elements in larger, more robust industrial sensors include tuning forks[3,4], cylindrical torsional resonators[5], spiral springs[6], and u-shaped wires[7]. In order to measure viscosity, it is necessary to shear the fluid. Resonators such as cylinders and spheres that oscillate around a central axis produce primarily shearing motions in the fluid, and therefore are limited to viscosity measurement. These types sensors have been used to measure the viscosity-density product of

Newtonian fluids as well as to investigate non-Newtonian fluids[8–11]. To measure density, an immersed resonator must displace through its motion. This requires that the motion of the resonator have a velocity component normal to its surface. This normal velocity component displaces fluid, loading the resonator with additional mass, which changes both its resonance frequency and its damping. For this reason, transversely vibrating resonators such as tuning forks, reeds, and wires have traditionally been used for density measurement.

It is also possible to measure fluid density with torsional resonators provided that a portion of the resonator vibrates normal to its own surface. Torsional resonators are attractive because they are less prone to wall effects than are transversely vibrating devices, making them easier to integrate into industrial systems. Fuchs et al.[12] described a straight-tube Coriolis sensor, in which an eccentric mass a was attached to a transversely vibrating tube through which a fluid was flowing. The eccentric mass converted the lateral vibration into a torsional mode superimposed on the transverse vibration, enabling simultaneous measurement of fluid viscosity, density and mass flow rate. A different approach to a torsional viscosity-density sensor was presented by Heinisch et al.[5], who used a resonating paddle for his measurements.

This paper presents a novel torsional resonator with a non-cylindrical tip that can measure a fluid's viscosity and density. The sensor's design is based on the symmetric torsional resonator described by Goodbread et.al.[13]. In the present study, it was demonstrated that the sensor can be used to measure fluids viscosities from less than 1 mPaS up to 4000 mPaS, and densities from 0.6 to 1.5g/cc at temperatures between 0°C and 120°C, with minimal reciprocal effects between viscosity and density. Viscosity and density measurements were shown to be nearly independent of one another.

2. WORKING PRINCIPLE AND SENSOR DESIGN

The sensor presented in this study is a symmetrical torsional resonator with a non-cylindrical tip (Figure 1). One end, containing a permanent magnet, is used for excitation and sensing of the resonator's motions; it is completely enclosed in the body of the sensor. The second end, which is immersed in the fluid, is provided with four radial fins. Each end is connected to a central nodal disk by means of a thin-walled elastic tube and directly connected with each other by a coaxially situated torsional spring which is not visible in the figure. This torsional spring vibrationally couples the two end masses resulting in minimal torsional reaction force on the nodal disk.

In the primary resonant mode, the nodal point is located at the central disk, which is the only connection to the resonator's housing. Having the nodal point at the mounting location means no forces are exerted by the resonator on the external structure, so that the resonator is largely isolated from its environment.

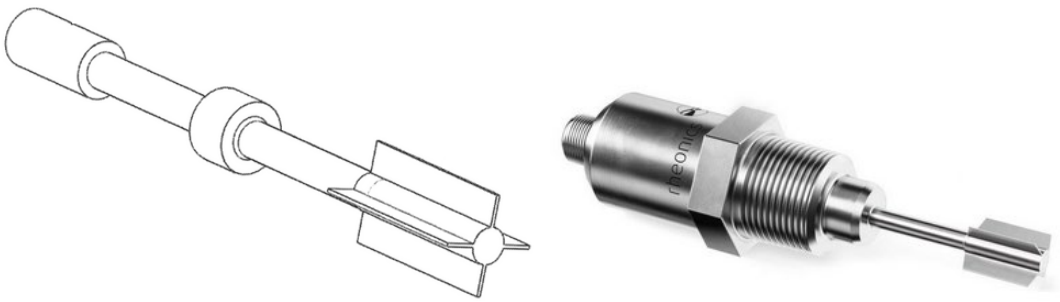

Figure 1: Rendering of the resonator (left), and the complete sensor (right)[13]

The operation of the sensor is based on torsional resonance. The out-of-phase torsional mode of the resonator is excited by a transducer located in the body of the sensor, producing motion in the surrounding fluid. The shear stresses caused by the fluid motion induce a torque on the sensor, which damps oscillation. The damping, resonance frequency, and temperature of the resonator tip are measured by associated electronic instruments, permitting changes in the resonator behavior to be related to the viscosity and density of the fluid.

The excitation and measurement of the torsional vibration are achieved using a gate phase locked loop system described by Goodbread and Dual [14]. A current is passed through coils in proximity to the magnet in the resonator end, inducing an alternating magnetic field that exerts an oscillating torque on the magnet. The motion of the resonator magnet is sensed by means of the induced current in the coils. The phase relationship between the current driving the magnetic field and the sense signal is fed back to control the frequency and amplitude of the excitation current, creating a phase locked loop. By changing the phase relationship between the excitation and sense signals, the relation between phase and frequency can be determined, from which the resonance frequency and damping of the resonant system can be determined.

3. METHODS

The purpose of this study is to investigate the changes of the resonator's characteristic using parameters that are used that are only sensitive towards either viscosity or density. The experimental procedure is described in Section 3.1. To predict the viscosity and density based on the measured properties, it is helpful to derive parameters which can be used to separate the effects of viscosity or density. The derivation of these parameters is discussed in Sections 3.2 and 3.3 for density and viscosity, respectively.

3.1 Experimental Procedure

Experiments were conducted at temperatures between 0 and 120°C. To determine the properties of the resonator without any fluid interaction, the bandwidth Γ_{air} and resonance frequency $f_{0,\mathrm{air}}$ were measured in air. The measured bandwidth in air Γ_{air} is the intrinsic damping of the resonator. Once the resonator is in contact with the fluid, the bandwidth changes. The damping due to the fluid is obtained by subtracting the intrinsic damping from the measured bandwidth Γ_{m} to yield the net damping Γ caused by the fluid. The bandwidth used hereafter is defined as the change of bandwidth caused by the fluid $\Gamma = \Gamma_{\mathrm{m}} - \Gamma_{\mathrm{air}}$.

In this study, Newtonian Fluids with well-known viscosity and density were used to measure the response of the sensor under well-defined conditions. The fluids used were either calibration oils from Cannon Instrument Company or pure chemical substances such as chloroform, acetone and n-dodecane. The fluid properties' viscosity (left) and density (right) with respect to temperature are shown in Figure 2.

The fluids cover a wide range of viscosities (0.2 – 3600 mPa.s) and densities (0.6 - 1.5 g/cc). Fluids were selected to so that their densities and viscosities overlapped over segments of the range of measurement temperatures. This allows measuring of, for example viscosity at different temperatures and densities, which enables determining cross-sensitivities between fluid properties.

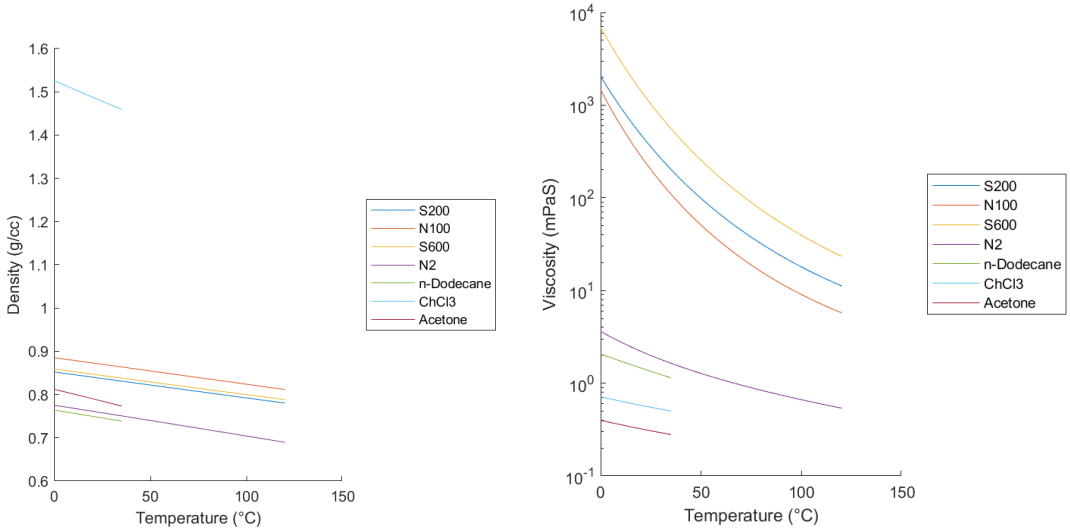

Figure 2: Viscosity and density of fluids with respect to temperature

To evaluate the repeatability of a measurement, the bandwidth and resonance frequency were measured at nine different temperatures between 20 and 120 °C. Each measurement cycle was repeated ten times. Between measurement cycles the sensor was cleaned and the measurement chamber refilled with fresh fluid. This resulted in a set of ten independent measurements for each of the nine different temperatures. The standard deviation of the bandwidth was 0.05 Hz for bandwidths ranging from 14 Hz up to 223Hz. This means that the sensor can detect a change in fluid viscosity of $\pm$1% with a 95% confidence level for fluid viscosities greater than 2.8 mPaS and $\pm$0.1% for viscosities greater than 450 mPaS. The standard deviation of the resonance frequency was 0.04

Hz for resonance frequencies from 7392-7491Hz. This enables the sensor to detect changes in fluid density of $\pm 1 \text{ x } 10^{-4}$ g/cc with a 95% confidence level at a fluid density of 0.84 g/cc.

3.2 Density Measurement

To determine the fluid density based on measured bandwidth and resonance frequency, a parameter is needed that depends only on the density. This parameter can be derived, based on a single degree of freedom resonator, i.e. a mass-spring system. The resonance frequency of such a system is defined by

$$\mathrm{f}_0 = \frac{1}{2\pi}\sqrt{\frac{c}{J}} \quad (1)$$

where c is a spring constant and J is a moment of inertia. The fluid creates an additional inertial load on the resonator, changing the inertia J and thus the resonance frequency. This shift in resonance frequency is described by Δf_0, which can be related to the fluid density, see Eq. (2),

$$\Delta f_0 = f_{0,air} - \left(f_0 + \frac{\Gamma}{2}\right) \quad (2)$$

where f_0 is the measured resonance frequency, Γ is the bandwidth, and $f_{0,air}$ is the resonance frequency in air at the same temperature f_0 was measured.

The parameter Δf_0 is used to compensate for temperature and viscosity effects.

- Viscosity effects are compensated for by adding half the bandwidth to the resonance frequency, which compensates for inertia added by the viscous boundary layer[15].
- Temperature affects the shear modulus of the resonator, which affects its undamped frequency. This temperature effect is removed by taking the difference to the resonance frequency in air at the same temperature.

Thus, the parameter Δf_0 should be a function only of the fluid density ρ and independent of fluid viscosity and temperature.

3.3 Viscosity Measurement

For many sensors, the bandwidth divided by the resonance frequency Γ/f_0 can be directly correlated to the viscosity-density product of the fluid. In a single degree-of-freedom resonator, parameter Γ/f_0 is equal to the ratio of moment of inertia J and the fluid-induced damping. Please note that the moment of inertia J is not the inertia of the structure. The inertia of the structure would be computed by Eq. (3),

$$\mathrm{J_s} = \int_V |\vec{r}|^2 \rho_s dV \quad (3)$$

where V is the volume of the resonator, ρ_s is the density of resonator, and $\vec{r}$ is the distance from the rotational axis.

The inertia J depends on the shape of the mode of the resonator since different parts of the structure have a different contribution due to different oscillation amplitudes. The inertia J also

accounts for the inertia added by the fluid. Assuming the inertia J is constant, then the term Γ/f_0 would be proportional to $\sqrt{\rho\eta}$ for low viscosities.

The present sensor was modelled by Brunner et al.[16] by a two-mass, three-spring system. Their results indicate that the measured damping is also affected by the fluid density in a manner that is beyond its contribution to the viscosity-density product, which in the simple case is the only contribution to fluid-induced damping. The cause of this density-dependency is the change of the moment of inertia J of the corresponding single degree of freedom system due to the added inertia by the fluid. This effect is amplified by a change of the modal function. To remove this density-related effect, the fluid induced damping must directly be determined. A method of doing this is multiplying the normalized bandwidth Γ/f_0 with the inertia J. For a single degree of freedom system, this removes all effects of the inertia and gives a direct measure of the fluid forces, i.e. viscous damping.

The inertia of the corresponding single degree of freedom system cannot be directly measured. Mathematically, it can be obtained by dividing the resonance frequency by its derivative with respect to the moment of inertia, Eq. (4).

$$-2\mathrm{J} = \frac{\mathrm{f}_0}{\frac{\partial f_0}{\partial J}} \tag{4}$$

Whereas the resonance frequency can be directly measured, its derivative $(\partial f_0)/\partial J$ cannot. A good assumption is that $(\partial f_0)/\partial J$ is in first order proportional to $(\partial f_0)/\partial \rho$, Eq. (5).

$$\frac{\partial f_0}{\partial J} \approx\propto \frac{\partial f_0}{\partial \rho} \tag{5}$$

The derivative $(\partial f_0)/\partial \rho$ can be expressed by the parameter Δf_0, which is used for measuring densities. We do this under the assumption that the fluid viscosity is relatively small, thus the term $\Gamma/2$ in Eq. (2) can be neglected, see Eq. (6).

$$\frac{\partial f_0}{\partial \rho} = \frac{\partial(\Delta f_0)}{\partial \rho} \tag{6}$$

This assumption implies that the inertia can be described by Eq. (7),

$$J = J_0 + a \cdot \rho \tag{7}$$

where J_0 and a are coefficients of the linear function for the inertia J.

Then, we can show the proportionality of $(\partial f_0)/\partial \rho$ and $(\partial f_0)/\partial J$,using the chain rule, Eq. (8).

$$\frac{\partial f_0}{\partial J} = \frac{\partial f_0}{\partial \rho}\frac{\partial \rho}{\partial J} = \frac{\partial f_0}{\partial \rho}\frac{-J_0}{a} \propto \frac{\partial f_0}{\partial \rho} \tag{8}$$

To compensate for density effects, the normalized damping Γ/f_0 is multiplied by $\mathrm{f}_0/((\partial f_0)/\partial \rho)$, resulting in the corrected normalized damping parameter Γ^+, Eq. (9).

$$\Gamma^+ = \frac{\Gamma}{\mathrm{f}_0} \cdot \frac{\mathrm{f}_0}{\frac{\partial f_0}{\partial \rho}} = \frac{\Gamma}{\frac{\partial(\Delta f_0)}{\partial \rho}} \tag{9}$$

This parameter should only be sensitive to viscous damping, i.e. only depend on the viscosity-density product of the fluid.

4. DISCUSSION AND RESULTS

This section discusses how the parameters derived in section 3 correlate with the fluid's viscosity and density. Section 4.1 discusses the effects on the density measurement, whereas Section 4.2 discusses the viscosity measurement.

4.1 Density Measurement

The Δf_0value was measured for different fluids over a range of temperatures, viscosities and densities, as shown in Figure 3. All points tend to converge to one curve, implying that the parameter $\Delta f_0$is a function only of the fluid density. Therefore, there is no need for complex multi-dimensional correlation functions, and the fluid density can directly be determined based on the Δf_0 value.

To model the correlation between Δf_0 and ρ, a purely empirical model such as a polynomial is unsuited because the measurements are clustered rather than uniformly distributed; interpolating between the clusters is unreliable. Furthermore, the derivative $(\partial(\Delta f_0)/\partial\rho$ is needed for determining the parameter Γ^+, which would require a high-order polynomial for an accurate fit.

A more robust interpolation method is to use a base function, which reflects the basic properties of the sensor, and correct it to fit the experimental data. Brunner et al. [16] described a numerical model based on a two-mass, three-spring system for the presented sensor. This model predicts the Δf_0 value for a given fluid density for the presented sensor. To account for deviations between the numerical model and experimental data, the numerical prediction $\Delta f_{0,sim}(\rho)$ is multiplied by an empirical correction function $c(c_1, c_2)$; see Eqs. (10) and (11),

$$\Delta f_{0,m}(c_1, c_2, \rho) = \Delta f_{0,sim}(\rho) \cdot c(a, b) \quad (10)$$

$$c(c_1, c_2) = c_1 + c_2 \cdot \rho \quad (11)$$

where $\Delta f_{0,m}$ is the fitting function and c_1, c_2 are coefficients fitted to the experimental data, using the least square method and; see Eq. (12).

$$c_1, c_2 \colon \min\left(\sum(\Delta f_0(\rho, \eta) - \Delta f_{0,m}(\rho, c_1, c_2)\right) \quad (12)$$

The fitting function $\Delta f_{0,m}$ is shown as a black line in Figure 3. For a single degree of freedom model, the fitting function would be almost a straight line. The model predicts, and the experimental results confirm, a non-linear relation between the Δf_0 value and fluid density. The slope of the curve decreases with respect to fluid density at higher densities. This behavior is caused by change of the modal function, which in turn changes the inertia of the resonator and decreases the absolute sensitivity to density at high densities.

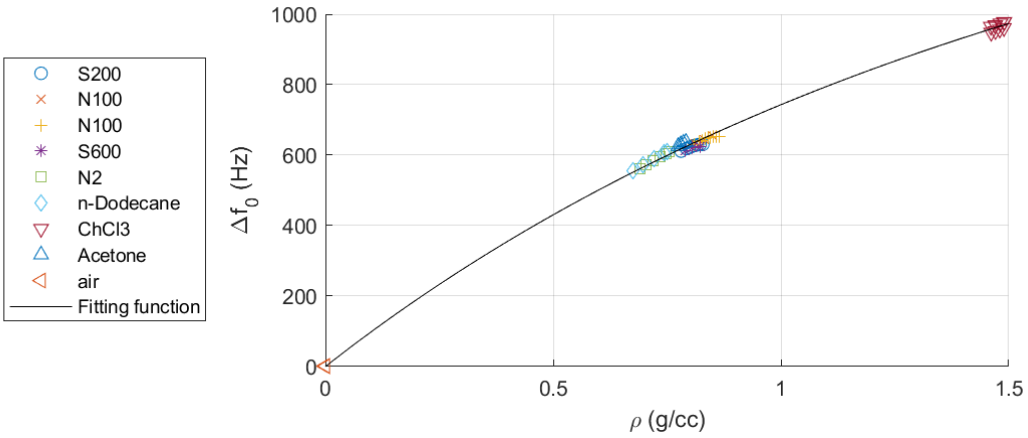

Figure 3: Fluid density ρ vs. the parameter Δf_0 for different fluids with different fluid densities, viscosities at temperatures between 0°C and 120°C

4.2 Viscosity Measurement

Fluid damping is typically correlated to the viscosity-density product. To measure the fluid viscosity, the fluid density is first determined, then the viscosity value is computed. Figure 4 shows the values of Γ^+ for different fluids at different temperatures, viscosities and densities. By plotting the viscosity-density product against the parameter Γ^+, all points collapse onto one curve. There is no systematic influence of fluid density or temperature on the measurement, indicating that the parameter Γ^+ is only a function of the viscosity-density product.

The black line shows the empirical model based on a polynomial function which can be used to predict the viscosity-density product based on the measured bandwidth and resonance frequency, Eq. (13),

$$\ln(\Gamma^+) \approx \sum_n \mathrm{a_n} ln\left(\sqrt{\rho\eta}\right)^n \qquad (13)$$

where η is the dynamic viscosity and $\mathrm{a_n}$ the coefficients of the empirical model.

The coefficients $\mathrm{a_n}$ are determined by using the least square method. For low viscosities, parameter Γ^+ is proportional to the square root of the viscosity-density product. This behavior is typical for viscosity sensors based on vibrating structures. However, with higher viscosities the behavior deviates from this typically observed trend. According to Brunner et al.[16], it is likely that such a deviation originates from three dimensional flow effects at the tip which become more dominant as the boundary layer thickness increases with viscosity.

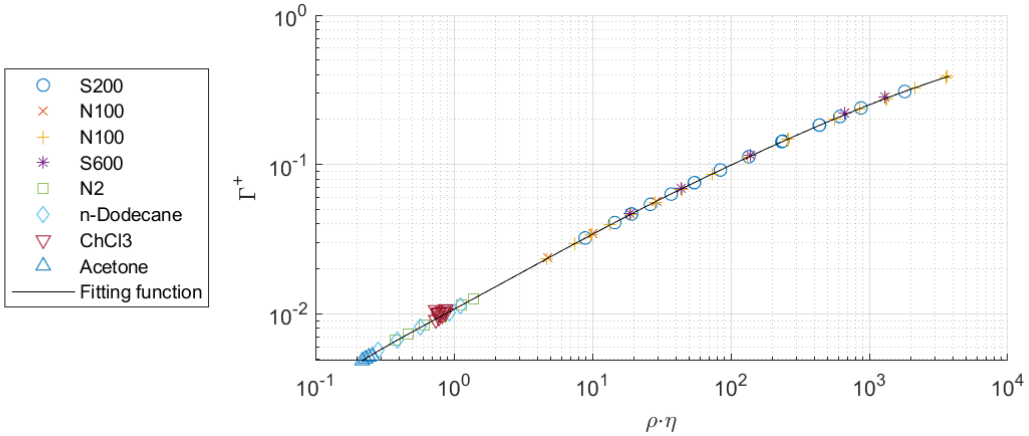

Figure 4: Product of viscosity η and density ρ vs. the parameter Γ^+ for different fluids with different fluid densities, viscosities at temperatures between 0°C and 120°C

5. CONCLUSION

In this study, a new viscosity-density sensor was presented. The sensor is based on an electromagnetically driven torsional resonator having a non-cylindrical tip which is immersed in the fluid. The fluid changes the resonance frequency and bandwidth of the resonator. These changes in resonator properties are then related to the fluid's viscosity and density.

Experiments were conducted under thermally uniform conditions at temperatures between 0 and 120°C, using different Newtonian fluids with well-known viscosities and densities. The measured bandwidth and resonance frequency were correlated to the fluid properties, using parameters that depend only on either density or the viscosity-density product. Thus, viscosity and density can be predicted without cross-sensitivity between temperature, density and viscosity.

The sensor has proven to give accurate measurements over a wide range of fluid properties. The measurements show a good repeatability, allowing the sensor to be able to detect changes in viscosity of 1% for viscosities greater 2.8 mPaS and 0.1% for viscosities greater 450 mPaS with a 95% confidence level. Changes of fluid density of $\pm 1 \text{ x } 10^{-4}$ g/cc are detectable with a 95% confidence level at a fluid density of 0.84 g/cc.

Further studies are planned to include the investigation of non-Newtonian fluids, where the interaction of the fluid properties and the sensor is highly fluid-dependent.

REFERENCES

1 B. Jakoby, R. Beigelbeck, F. Keplinger, F. Lucklum, A. Niedermayer, E.K. Reichel, C. Riesch, T. Voglhuber-Brunnmaier, B. Weiss, Miniaturized sensors for the viscosity and density of liquids - Performance and issues, IEEE Trans. Ultrason. Ferroelectr. Freq. Control. 57 (2010) 111–120. https://doi.org/10.1109/TUFFC.2010.1386.

2 M. Heinisch, T. Voglhuber-Brunnmaier, E.K. Reichel, I. Dufour, B. Jakoby, Reduced order models for resonant viscosity and mass density sensors, Sensors Actuators, A Phys. 220 (2014) 76–84. https://doi.org/10.1016/j.sna.2014.09.006.

3 M. Heinisch, T. Voglhuber-Brunnmaier, E.K. Reichel, I. Dufour, B. Jakoby, Application of resonant steel tuning forks with circular and rectangular cross sections for precise mass density and viscosity measurements, Sensors Actuators, A Phys. 226 (2015). https://doi.org/10.1016/j.sna.2015.02.007.

4 J. Toledo, T. Manzaneque, J. Hernando-García, J. Vázquez, A. Ababneh, H. Seidel, M. Lapuerta, J.L. Sánchez-Rojas, Application of quartz tuning forks and extensional microresonators for viscosity and density measurements in oil/fuel mixtures, in: Microsyst. Technol., 2014: pp. 945–953. https://doi.org/10.1007/s00542-014-2095-x.

5 M. Heinisch, T. Voglhuber-Brunnmaier, E.K. Reichel, I. Dufour, B. Jakoby, Electromagnetically driven torsional resonators for viscosity and mass density sensing applications, Sensors Actuators, A Phys. 229 (2015) 182–191. https://doi.org/10.1016/j.sna.2015.03.033.

6 M. Heinisch, S. Clara, I. Dufour, B. Jakoby, A spiral spring resonator for mass density and viscosity measurements, Procedia Eng. 87 (2014) 1143–1146. https://doi.org/10.1016/j.proeng.2014.11.367.

7 M. Heinisch, E.K. Reichel, I. Dufour, B. Jakoby, A U-shaped wire for viscosity and mass density sensing, Sensors Actuators, A Phys. 214 (2014) 245–251. https://doi.org/10.1016/j.sna.2014.04.020.

8 T. Brack, Multi-frequency phase control of a torsional oscillator for applications in dynamic fluid sensing, 2017, ETH Zürich, PhD dissertation. https://doi.org/https://doi.org/10.3929/ethz-a-010867290.

9 T. Brack, S. Bolisetty, J. Dual, Simultaneous and continuous measurement of shear elasticity and viscosity of liquids at multiple discrete frequencies, Rheol. Acta. 57 (2018) 415–428. https://doi.org/10.1007/s00397-018-1083-y.

10 T. Brack, J. Dual, Multimodal torsional vibrations for the characterization of complex fluids, in: WIT Trans. Built Environ., 2013: pp. 191–199. https://doi.org/10.2495/FSI130171.

11 J. Dual, Experimental methods in wave propagation in solids and dynamic viscometry, 1989, ETH Zürich, PhD dissertation.

12 M. Fuchs, W. Drahm, C. Matt, A. Wenger, A Coriolis meter with direct viscosity measurement, Flomeko. (2003)

13 J. Goodbread, S. Kumar, K. Häusler, B. Zybach, Temperature compensated density viscosity sensor having a resonant sensing element, United States patent US 10,502,670, 2016.

14 J. Goodbread, J. Dual, Resonant conductor measurement system and method, United States patent US 8,752,716 B2, 2014.

15 D. Johannsmann, *The Quartz Crystal Microbalance in Soft Matter Research: Fundamentals and Modeling* (2014).

16 D. Brunner, J. Goodbread, K. Häusler, K. Sunil, B. Gernot, H. Khawaja, Modelling a Viscosity-Density Sensor based on Micro-Vibration, Target J. Sensors Actuators A. Phys. (n.d.).

Paper II

Modelling a Viscosity–Density Sensor based on Small Amplitude Torsional Vibrations

D. Brunner[1,2], J. Goodbread[3], K. Häusler[3], S. Kumar[3], G. Boiger[1], H. Khawaja[2]

Manuscript ready

1. ZHAW, Zurich University of Applied Sciences, Switzerland
2. UIT, The Arctic University of Norway
3. Rheoncis GmbH, Switzerland

Author contributions:

- D. Brunner, H. Khawaja conceptualized the study
- D. Brunner, and H. Khawaja did the methodology
- D. Brunner did all numerical work
- D. Brunner and H. Khawaja did the numerical validation
- D. Brunner prepared the draft
- D. Brunner, J. Goodbread, S. Kumar and H. Khawaja did review and editing
- D. Brunner did the visualization
- H. Khawaja, J. Goodbread and G. Boiger did the supervision
- G. Boiger and S. Kumar did the project administration
- G. Boiger and S. Kumar did the funding acquisition

Organizations contributions:

- MATLAB® license was provided by ZHAW
- COMSOL Multiphysics® license was provided by ZHAW

Funding:

- This research was partially funded by Innosuisse, grant number 27254.1

Modelling a Viscosity-Density Sensor based on Small Amplitude Torsional Vibrations

D. Brunner[1,2*], J. Goodbread[3], K. Häusler[3], S. Kumar[3], H. Khawaja[2], G. Boiger[1]

[1]ZHAW, Zurich University of Applied Sciences Winterthur

[2]UIT The Arctic University of Norway

[3]Rheonics GmbH, Switzerland

*Corresponding author. Email: brni@zhaw.ch

Abstract

The flow field around a cylindrical torsional resonator can be modelled analytically, but more complex shapes require more rigorous approaches. This study proposes a numerical model of a non-cylindrical torsional resonator for a viscosity–density measurement application. The proposed model couples an analytical mechanical model of the resonator with an empirical, simulation-based fluid model. The model was validated using experimental data over a wide range of fluid viscosities and densities. The predictions are in good agreement with the numerical model. The model could capture all viscosity- and density-related effects. Therefore, it will, enable computationally supported geometrical optimization of future viscosity-density sensors generations.

Keywords: computational fluid dynamics, viscosity sensor, density sensor, fluid–structure interaction

1. INTRODUCTION

In many chemical and biochemical processes, viscosity and density can be used as indicators of the composition of a fluid at any point during those processes. Real-time, inline measurements of fluid viscosity and density provide important information about the progress of such processes and enable automated control. Resonance sensors are capable of simultaneously measuring both viscosity and density, either through sampling or inline measurements. To develop and calibrate resonance sensors, models are required to describe the fluid–structure interaction.

Typically, resonators are modeled using simplified, single-degree-of-freedom (SDOF) models in which the resonance frequency and damping of the resonator are related to the fluid's viscosity and density. Heinisch [1] presented such an SDOF model based on lumped elements. In his model, the resonator was interpreted as a mass–spring system, where the fluid created an inertial load and damped the oscillation. The viscous-induced damping was computed based on an analytical one-dimensional fluid model, which described the flow over an in-plane oscillating plate. The resulting shear stress was used to determine the fluid damping. This approach of using an analytical fluid model in combination with an SDOF fluid model has also been used, in different configurations by other researchers [2–9]. Another geometry for which the fluid domain can be analytically modeled is that of cylindrical structures, though the curvature of the surface adds complexity to modeling the

in-plane oscillating plate. This approach was used by Dual [10], Heinisch [3, 4], Fuchs [11], and Clara [12].

Several different geometries can be calculated using such analytical models. However, as complexity increases, the one-dimensional shear wave approximation may no longer be applicable, necessitating the use of numerical methods. Fluid–structure interaction models are an option for numerically solving the flow field and predicting damping and changes of resonance frequency. Using this method, Mahmoodi and Anthony [13] studied a torsional paddle with a two-dimensional (2-D) fluid–structure interaction model. Reichel et al. [14] presented a 2-D simulation to study the characteristics of an oscillating rectangle and obtain scaling properties for larger sensors. They also showed that to simulate a resonator, a complete three-dimensional (3-D) fluid–structure interaction model requires an impracticable amount of computational resources. Therefore, reduced-order models are preferable for efficiently studying different geometries numerically.

The goal of this study was to develop a mathematical model describing the sensor presented by Goodbread et al. [15]. This paper describes a weak fluid–structure interaction model based on a mass–spring system coupled with an empirical fluid model. Its novelty is that the empirical fluid model is based on a parameter study conducted using computational fluid dynamics (CFD). The proposed model was validated against experimental data [15].

2. NUMERICAL MODEL

The sensor investigated in this study is a probe-style torsional resonator, first reported and then experimentally investigated by Goodbread et al [15,16]. The proposed model aims to describe the change in resonance frequency and damping induced by fluids of different viscosities and densities.

Section 2.1 discusses the structural part of the resonator model. In this model, the fluid interaction is approximated by source terms, as described in detail in Section 2.2, with the cylindrical and tip sections described using different models in Sections 2.2.1 and 2.2.2, respectively.

2.1 Resonator Model

The torsional resonator was modeled as a mass–spring system, which is a symmetric, cylindrical probe-style resonator comprised of two main masses which act as the inertial masses J_1 and J_2 for torsional vibration (see Figure 1). Each of these inertial masses is connected to a fixed point through a thin-walled tube c_1 which acts as a torsional spring. Additionally, the inertial masses J_1 and J_2 are directly connected to each other by a coaxially situated inner rod c_2. This spring vibrationally couples the two inertial masses. There are two primary modes of vibration: one in which both inertial masses oscillate in-phase, and another in which they oscillate out-of-phase. The out-of-phase mode was used for measurement purposes because its minimal net torsional reaction force at the fixed point largely isolates the resonator from its environment. The tip has four radial fins attached to it. These fins create a velocity component perpendicular to their own plane surface that causes fluid displacement, i.e., inertial mass loading on one end. This effect changes J_2, which affects the amplitude ratio between tip and back. Figure 1 shows a schematic of the sensor (above) and the mode shape (below), where the tip and back amplitudes are different. The pink line shows the angular deflection amplitude of the inner rod c_2, and the blue line shows that for the springs c_1. The amplitude of the immersed end (the tip) of the resonator is described by $\hat{\varphi}_{i,2}$, and the other end (the back) is described by $\hat{\varphi}_{i,1}$, where the index i represents the mode-number.

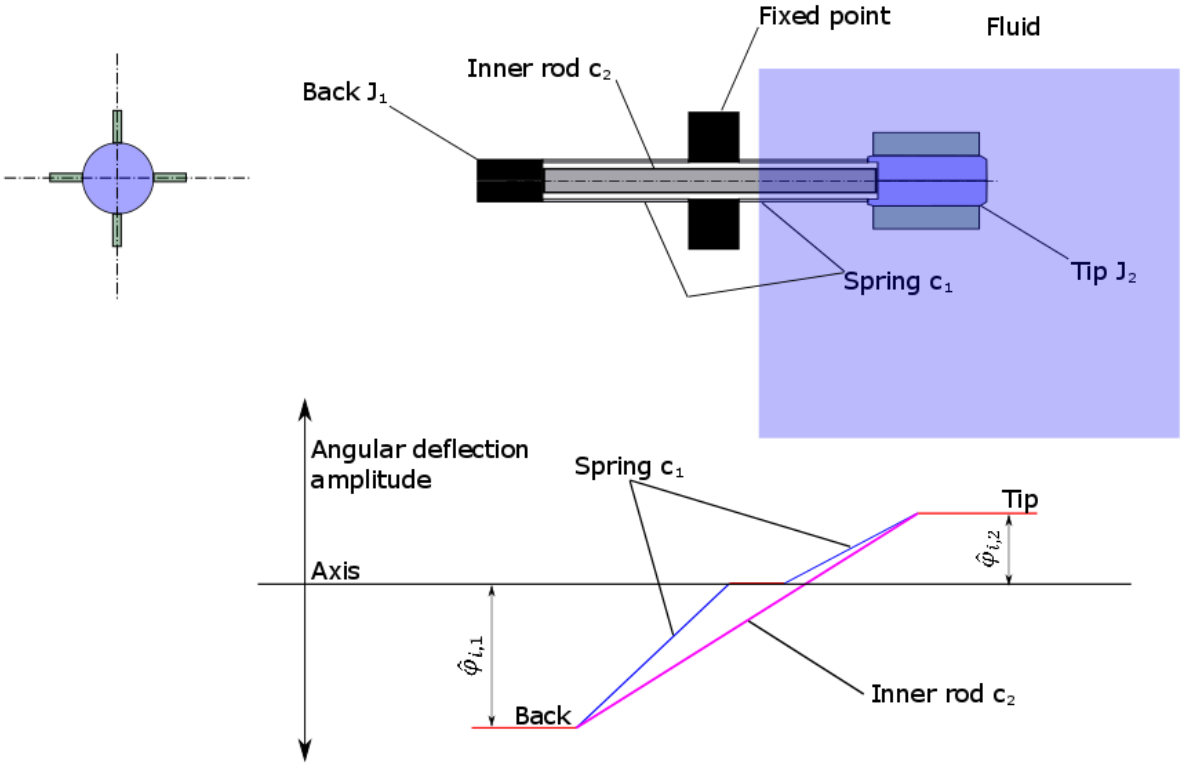

Figure 1: Schematic of the sensor (above) and modal function (below). The red line shows the angular deflection amplitude of the tip $\hat{\varphi}_{i,2}$ and back $\hat{\varphi}_{i,1}$, the blue line shows the deflection amplitude of the springs c_1, and the pink line shows the angular deflection amplitude of the inner rod c_2.

The model describes the angular deflection of the two inertial masses J_1 and J_2 (see Eqns. (1) and (2)) by a linear system with multiple degrees of freedom,

$$\boldsymbol{J}\frac{\partial^2\vec{\varphi}}{\partial t^2} + \boldsymbol{D}\frac{\partial\vec{\varphi}}{\partial t} + \boldsymbol{C}\vec{\varphi} = 0 \tag{1}$$

where is the $\boldsymbol{J}$ mass-matrix, $\boldsymbol{D}$ is the damping matrix, $\boldsymbol{C}$ is the spring matrix and $\vec{\varphi}$ is the angular deflection vector consisting of the angular deflection of the tip amplitude φ_1 and back φ_2, see Eqn (2).

$$\vec{\varphi} = \begin{bmatrix}\varphi_1 \\ \varphi_2\end{bmatrix} \tag{2}$$

To solve Eqn (1), it is transformed from the time domain into the frequency domain (seen Eqn (3)),

$$-\omega^2\boldsymbol{J}\vec{\hat{\varphi}} + i\omega\boldsymbol{D}\vec{\hat{\varphi}} + \boldsymbol{C}\vec{\hat{\varphi}} = 0 \tag{3}$$

where $\vec{\hat{\varphi}}$ is the angular deflection amplitude, ω is the angular frequency and $i = \sqrt{-1}$.

Then, Eqn (3) can be solved as an eigenvalue-problem, Eqn (4),

$$(\boldsymbol{J}\lambda^2 + \boldsymbol{D}\lambda + \boldsymbol{C})\vec{\hat{\varphi}}_i = \vec{0} \tag{4}$$

where $\lambda = i\omega$ is the eigenvalue and $\vec{\hat{\varphi}}_i$ is the eigenvector. Hence, the solution of Eqn (1) has the following form: $\vec{\varphi} = \vec{\hat{\varphi}}_i \cdot \mathrm{e}^{\mathrm{i}\lambda_\mathrm{i}\mathrm{t}}$, where λ_i is the eigenvalue and $\vec{\hat{\varphi}}_i$ its corresponding eigenvector.

Based on the eigenvalue, the resonance frequency f_0 and bandwidth Γ can be determined (Eqns. (5) and (6)).

$$f_0 = \Re\left(\frac{\lambda}{2\pi}\right) \tag{5}$$

$$\Gamma = \Im\left(\frac{\lambda}{\pi}\right) \tag{6}$$

The entries of the inertial mass matrix $\boldsymbol{J}$ and damping matrix $\boldsymbol{D}$ are dependent on both the eigenvector and eigenvalue of the mode of interest (when $\hat{\varphi}_{i,1}$ and $\hat{\varphi}_{i,2}$ are of approx. opposite phase). Due to this non-linear dependency, the Eqn (4) is solved iteratively, until the resonance frequency f_0 has converged below 0.01 Hz.

To solve the eigenvalue problem (Eqn. (4)), the matrices $\boldsymbol{J}$, $\boldsymbol{C}$ and $\boldsymbol{D}$ must be determined. Matrix $\boldsymbol{J}$ and $\boldsymbol{D}$ are dependent on the solution, i.e. on the resonance frequency and the eigen-vector. The inertial mass matrix $\boldsymbol{J}$, see Eqn (7),

$$\boldsymbol{J} = \begin{bmatrix} J_1 + \frac{|\hat{\varphi}_{i,1}|}{2(|\hat{\varphi}_{i,1}|+|\hat{\varphi}_{i,2}|)} J_r & 0 \\ 0 & J_2 + \frac{|\hat{\varphi}_{i,2}|}{2(|\hat{\varphi}_{i,1}|+|\hat{\varphi}_{i,2}|)} J_r + J_f \end{bmatrix} \tag{7}$$

consist of the end masses J_2 and J_1, additionally, the inertial mass of the inner rod J_r and the inertial mass of the fluid J_f. The inertial mass of the inner rod J_r is split between tip and back depending on the amplitude ratio. This amplitude ratio is calculated based on the eigenvector $\vec{\hat{\varphi}}_i$ of the asymmetric solution, when $\hat{\varphi}_{i,1}$ and $\hat{\varphi}_{i,2}$ are of approximately opposite phase. The inertial mass caused by the fluid-interaction only appears at the tip of the resonator and is based on the flow simulation as will be discussed in section 2.2.

The viscous damping caused by the fluid-interaction is imposed on the tip and described by the damping matrix $\boldsymbol{D}$, Eqn (8). The damping coefficient d_f within the damping matrix $\boldsymbol{D}$ is discussed in detail in chapter 2.2.

$$\boldsymbol{D} = \begin{bmatrix} 0 & 0 \\ 0 & d_f \end{bmatrix} \tag{8}$$

The spring matrix $\boldsymbol{C}$ is derived based on the structure of the resonator and thus given by:

$$\boldsymbol{C} = \begin{bmatrix} c_1 + c_2 & -c_2 \\ -c_2 & c_1 + c_2 \end{bmatrix} \tag{9}$$

where c_1 and c_2 are the springs in the system.

2.2 Fluid Interaction

The fluid interacts with the oscillating system on the immersed part of the sensor. This interaction can be accounted for by parameters J_f and d_f. The two parts of the sensor that interact with the fluid, i.e., spring c_1 and the tip, were modeled through different approaches. The spring c_1 is a cylindrical structure for which the flow can be described analytically. The tip is a cylinder with four radial fins attached, for which the flow was computed using CFD.

2.2.1 Cylindrical section

The velocity amplitude of an oscillating structure that is immersed in the fluid typically decays exponentially with increasing distance from the moving boundary. The distance at which the flow velocity amplitude is $1/e$ of the boundary-wall velocity amplitude is called the boundary-layer thickness δ. For a flat oscillating plate, δ is defined by Eqn. (10):

$$\delta = \sqrt{2\frac{\eta}{\rho\omega}} \tag{10}$$

where η is the dynamic viscosity, ρ is the fluid density, and ω is the angular frequency.

For our sensor, the boundary-layer thickness for water was approximately $6.5\ \mu\mathrm{m}$. In comparison, the radius of the cylindrical section was 2.5 mm. Thus, the flow length scale δ was several orders of magnitude smaller than the radius R of spring c_1 ($\delta \ll R$); therefore, it could be ignored. This approach has been proven for torsional resonators by Brack et al. [17], Dual [10], and Clara et al. [12] under these conditions.

In this approach, the azimuthal flow u_α over the surface is modeled under the assumption that the flow is unidirectional and is thus only subject to shear stresses and inertial forces; see Eqn. (11).

$$\frac{u_\alpha}{\partial t} = \frac{\eta}{\rho}\frac{\partial^2 u_\alpha}{\partial r^2} \tag{11}$$

where r is the radial location and t is the time.

Equation 11 can be solved under the assumption of a periodic solution and the following boundary conditions (Eqns. (12)–(15)):

$$u_\alpha = \frac{i}{\omega}\frac{\eta}{\rho}\frac{\partial^2 u_\alpha}{\partial r^2} \tag{12}$$

$$u_\alpha(\mathrm{r} = \mathrm{R}) = v_0 \cdot e^{i\omega t} \tag{13}$$

$$u_\alpha(\mathrm{r} = \infty) = 0 \tag{14}$$

$$u_\alpha(r,t) = -v_0 e^{\frac{r-R}{\delta(1+i)}} e^{i\omega t} \tag{15}$$

where r is the distance from the center, R is the radius of the structure, and v_0 is the velocity amplitude of the oscillating surface.

The velocity amplitude v_0 is not constant over the length of the structure. The boundary velocity will be zero where the spring is attached to the central disk (nodal point) and $R\omega\hat{\varphi}_{i,1}$ where the spring is attached to the tip. Between these points, the boundary velocity increases linearly.

2.2.2 Computational Fluid Dynamics

The tip of the sensor is a cylinder with four radial fins attached. The flow was modeled using CFD. There are different ways of modeling the motion of the tip, such as constructing a frame of reference or applying the motion as a boundary velocity. These methods have been compared in a previous study [18]. It was found that modeling the motion as a boundary velocity in COMSOL Multiphysics is an efficient method for computing the flow around the tip.

The fluid mechanics equations for an incompressible, homogeneous Newtonian fluid are solved using Eqns. (16)–(17).

$$\nabla \cdot \vec{\mathrm{u}} = 0 \tag{16}$$

$$\frac{\partial \vec{\mathrm{u}}}{\partial t} + \vec{\mathrm{u}} \cdot \nabla \vec{\mathrm{u}} = \frac{-\nabla p}{\rho} + \frac{\eta}{\rho}\Delta \vec{\mathrm{u}} \tag{17}$$

where $\vec{\mathrm{u}}$ is the velocity, ρ is the density, η is the dynamic viscosity, and p is the pressure.

The torsional oscillation of the tip was modeled by a boundary velocity (see Eqn. (18)):

$$\vec{u}_0 = \hat{\varphi}_{i,1} \sin(\omega t)\, (\vec{\mathrm{r}} \times \vec{\mathrm{e}}_z) \tag{18}$$

where $\hat{\varphi}_{i,1}$ is the angular deflection amplitude of the torsional oscillation, ω is the angular frequency, $\vec{\mathrm{r}}$ is the distance from the rotational axis, $\vec{\mathrm{e}}_z$ is the unity vector of the rotational axis, and t is the time.

The fluid mechanics equations were solved in a 2-D domain because of the high computational effort required to solve them three-dimensionally. Therefore, edge effects and other 3-D effects were ignored. The errors introduced by using a 2-D instead of a 3-D domain were assumed to be small for low-viscosity fluids because the structural length scale was much larger than the fluid boundary layer δ.

The mesh of the domain was created in COMSOL Multiphysics and checked for mesh sensitivity (see Figure 2). The external boundary of the mesh was set to “open”, where the shear stress across the boundary was zero. The distance from the external boundary to the structure was large enough so that it did not affect the solution. The boundary of the oscillating structure was resolved using 18 boundary layers, with a growth rate of 1.2 for a minimal boundary-layer thickness of 1 µm. This minimal boundary-layer thickness was sufficient for accurately resolving the flow near the boundary.

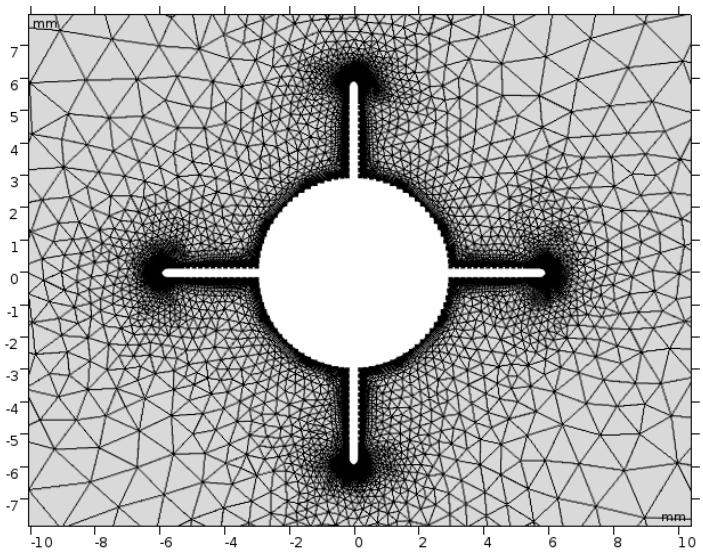

Figure 2: 2-D mesh of the computational domain in COMSOL Multiphysics with 26,558 elements.

3. METHODS

The resonance frequency and bandwidth of the resonator were computed using the solution of Eqn. (4). The parameters J_f and d_f accounted for the viscosity- and density-related effects on the resonator. Section 3.1 aims to describe parameters J_f and d_f through an empirical model that is derived based on the flow simulations in Section 2. This empirical model efficiently couples the flow simulation and the resonator model in a weak manner. A strong coupling, where both are solved simultaneously, would require significantly more computational resources.

3.1 Viscous Damping and Mass Loading

The damping and the inertial mass loading caused by the fluid were computed using the solution of the flow field once a quasi-steady state was reached. Thereby, the fluid forces were integrated over the structure of the tip (A_{tip}) and the cylindrical section. These forces originated from shear stresses and pressure on the wall of the resonator. The forces created a torque that was purely harmonic at the excitation frequency at quasi-steady-state conditions. This torque was computed for both shear stress $\widehat{M}_v$ and pressure $\widehat{M}_p$ independently and described by the complex amplitude at the excitation frequency obtained by Fourier analysis; see Eqns. (19) and (20).

$$\widehat{M}_v = \eta \left\{ \mathcal{F}\left(\vec{e}_z \cdot \iint_{A_{tip}} \left(\vec{r} \times (\vec{n} \cdot \nabla \vec{u}) \right) dA \right) + \mathcal{F}\left(\iint_{cylindrical} \left(R \cdot \frac{\partial u_\alpha(R,t)}{\partial r} \right) dA \right) \right\} \quad (19)$$

$$\widehat{M}_p = \mathcal{F}\left(\vec{e}_z \cdot \iint_{wall} (p\vec{n} \times \vec{r}) dA \right) \quad (20)$$

where $\mathcal{F}()$ is the Fourier analysis operator, $\vec{e}_z$ is the unity vector of the torsional axis, $\vec{r}$ is the distance from the torsional axis $\vec{e}_z$, and $\vec{n}$ is the surface normal of the boundary.

To integrate the torques into the model, they were decomposed into two physical phenomena: inertial mass of the fluid J_f and viscous damping d_f (see Eqns. (21) and (22)).

$$J_f = \Re\left(\frac{\widehat{M}_p + \widehat{M}_v}{\widehat{\varphi}_{i,1} \omega^2} \right) \quad (21)$$

$$d_f = \Im\left(\frac{\widehat{M}_p + \widehat{M}_v}{\widehat{\varphi}_{i,1} \omega} \right) \quad (22)$$

These two parameters depend on the fluid properties and the frequency and amplitude of the resonator. To integrate d_f and J_f into the equations of the matrixes (Eqns. (7) and (8)), an empirical model was used, which described the two parameters as a function of all degrees of freedom: angular deflection amplitude $\widehat{\varphi}_{i,1}$, angular frequency ω, dynamic viscosities η, and fluid density ρ.

Figure 3 shows d_f and J_f as functions of the boundary-layer thickness δ. The inertial mass J_f is normalized by the fluid density ρ, whereas the fluid damping d_f is normalized by $\sqrt{\eta \rho \omega}$. The normalization makes all points collapse onto one line, which can be modeled by a polynomial fit, i.e., an empirical model.

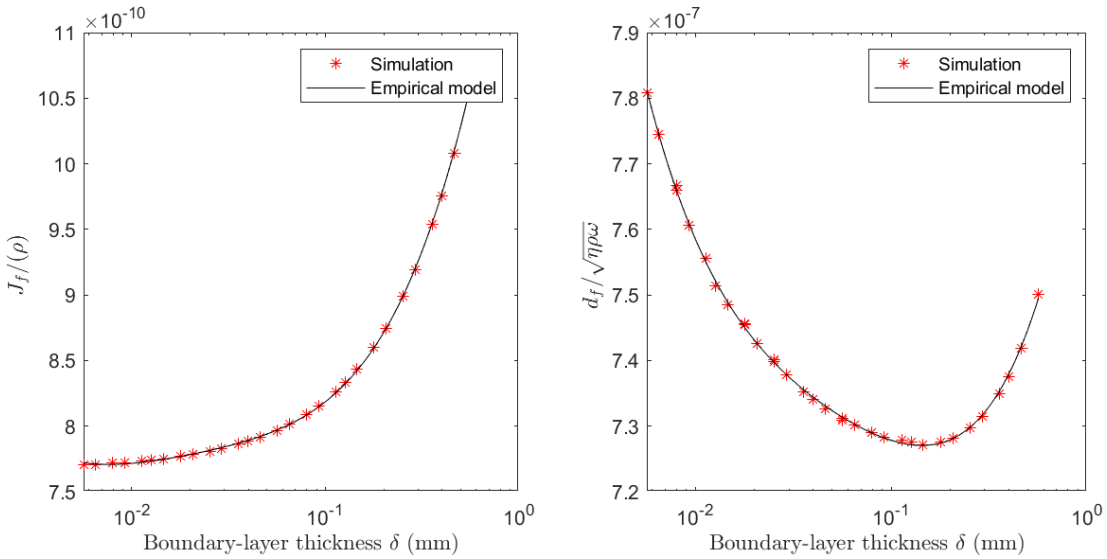

Figure 3: Normalized inertial mass of the fluid as a function of the boundary layer thickness (left) and normalized damping amplitude as a function of the boundary layer thickness (right).

4. DISCUSSION AND RESULTS

The proposed model is capable of predicting the bandwidth and resonance frequency of the torsional resonator based on fluid properties. The predictions were compared in two steps with experiment results obtained by Goodbread et al. [15]. First, the inertial masses of the structure $J_{0,1}$ and $J_{0,2}$ were fitted to the experimental data for different fluid densities (see Section 4.1). Then, the bandwidth was predicted for different fluid properties and compared with experiment results (see Section 4.2).

4.1 Effect of Mass Loading

To predict the resonance frequency of the sensor, Eqn. (4) was solved. The predicted resonance frequencies were then compared with the experimental data obtained by Goodbread et al. [15] for different fluid densities. Because of variations in dimensions due to manufacturing tolerance, the exact values of the inertial masses $J_{0,1}$ and $J_{0,2}$ were unknown. To account for potential variations, the inertial masses the structure of the tip $J_{0,1}$ and back $J_{0,2}$ were fitted to the resonance frequency of the experimental data using the least squares method. This method was applied to the differences between the predicted and experimentally determined resonance frequencies at a given set of viscosities, temperatures, and densities using Eqn. (22).

$$[J_1, J_2] \rightarrow \min\left(\sum_i \left(f_{0,exp}(\eta_i, \rho_i, T_i) - f_0\left([J_{0,1}, J_{0,2}], \eta_i, \rho_i, T_i\right)\right)^2\right) \tag{22}$$

The values calculated for $J_{0,1}$ and $J_{0,2}$ deviated by less than 5% from the values estimated from the dimensions of the sensor; hence, the results are plausible.

Figure 4 shows the measured and predicted resonance frequencies for different fluid temperatures and viscosities. The resonance frequency was affected by fluid density, viscosity, and temperature. With increasing viscosity, temperature, and fluid density, the resonance frequency decreased. The numerical model and experiment results are in good agreement.

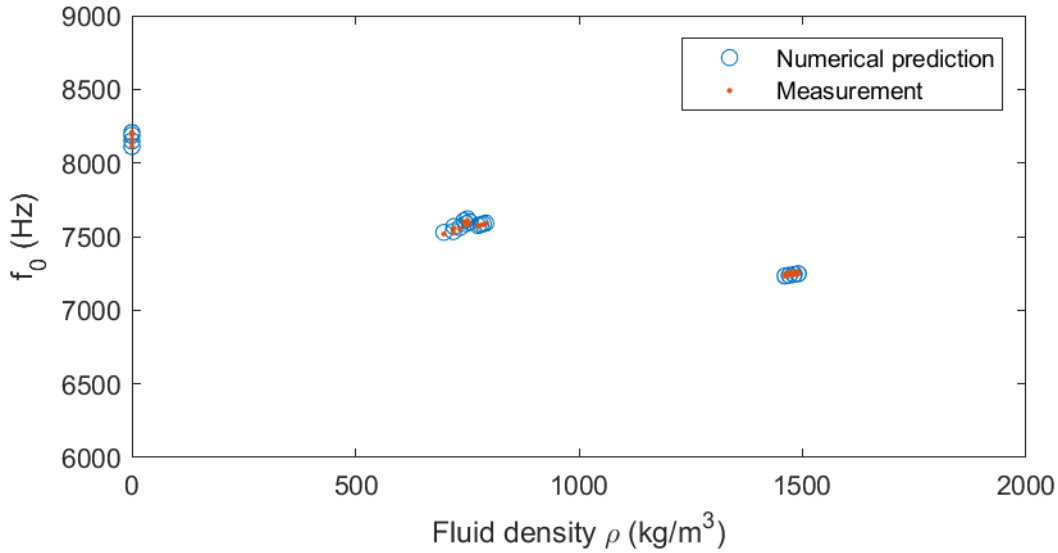

Figure 4: Comparison between predicted resonance frequency f_0 and measured resonance frequency for different fluid densities, temperatures, and viscosities.

4.2 Viscous Damping of the Resonator

The viscous damping of the resonator was measured at normalized bandwidth Γ/f_0, for which the bandwidth Γ was divided by the resonance frequency f_0. Figure 5 shows the normalized bandwidth Γ/f_0 with respect to the viscosity–density product of the fluid for both the experiments and numerical predictions. Most of the fluids had a fluid density between 650 and 900 kg/m³, as shown by the color bar. The fluid density of chloroform ($CHCl_3$) is approximately 1480 kg/m³ (temperature dependent) and is not shown in the color bar. The normalized bandwidth of $CHCl_3$ is approximately 40% lower than for the fluids with densities between 650 and 900 kg/m³. This effect does not originate from the relatively lower damping coefficient $\mathrm{d_f}$, but from a change in the amplitude ratio between tip and back $\hat{\varphi}_{i,2}/\hat{\varphi}_{i,1}$ due to the higher fluid density. The higher fluid density increased the inertia load at the tip J_2; thus, the deflection amplitude of the back increased. This resulted in a change in the balance between the inertial and damping forces of the system; thus, the normalized bandwidth was lower.

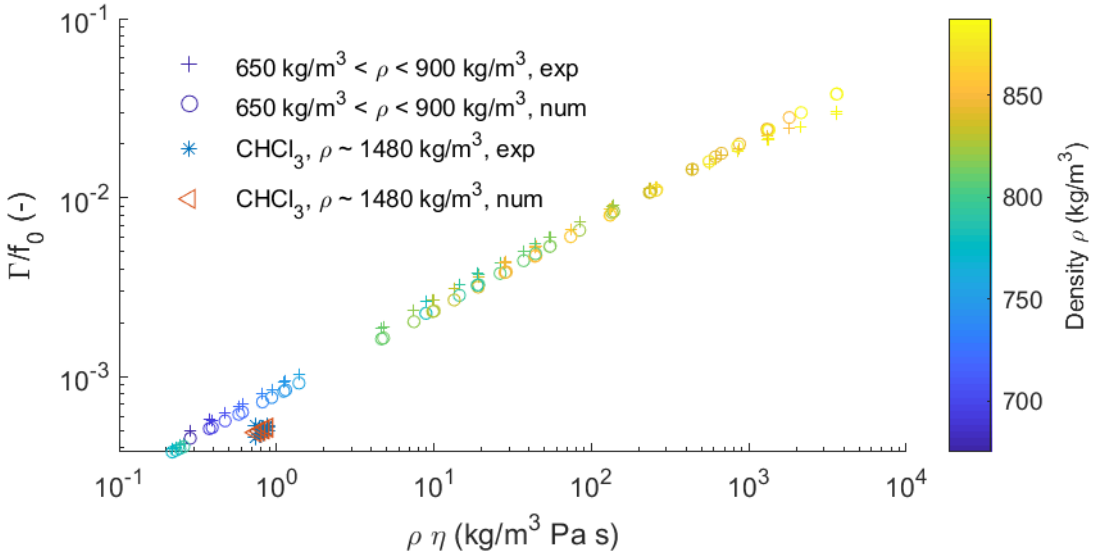

Figure 5: Comparison between predicted and measured [15] normalized bandwidths Γ/f_0 for different viscosity–density products; Γ is the bandwidth, f_0 is the resonance frequency, ρ is the fluid density, and η is the dynamic viscosity.

Figure 6 shows the relative deviation from the predicted and measured normalized bandwidths. For viscosities lower than 100 mPa·s (at a density of 1000 kg/m³), there is a constant offset between the measurement and prediction. At higher viscosities, the numerical model systematically deviates and predicts higher damping than is experimentally observed. Potential sources of this deviation are edge effects at the tip, which were neglected by reducing the computational domain into a cross section. An investigation including these edge effects in a 3-D domain will be part of future studies.

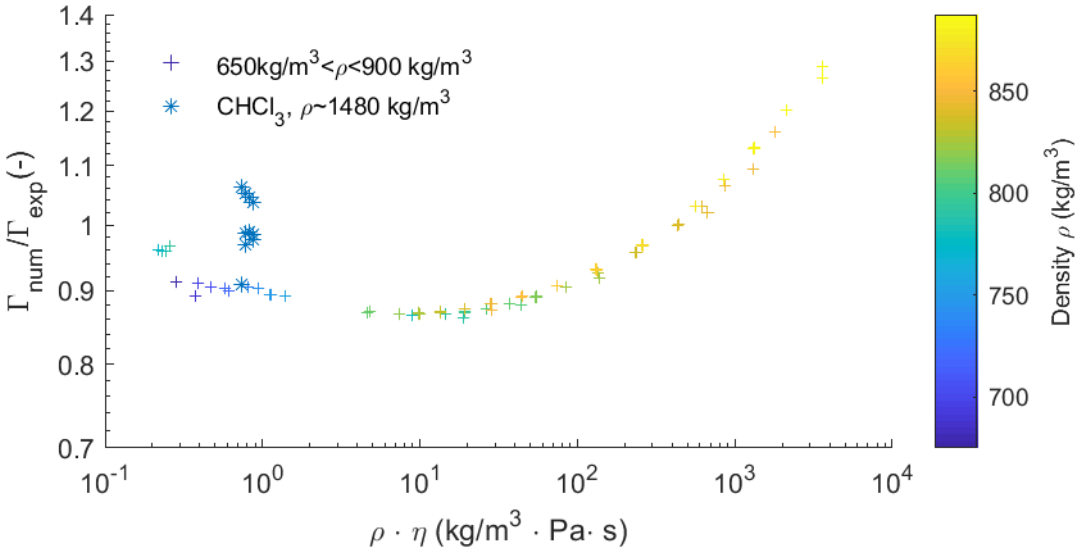

Figure 6: Relative deviation between predicted and measured [15] normalized bandwidths Γ/f_0 for different viscosity–density products, where Γ is the bandwidth, f_0 is the resonance frequency, ρ is the fluid density, and η is the dynamic viscosity.

5. CONCLUSION

In this paper, a mathematical model is presented that combines a mass–spring system with computational fluid dynamics. This model was used to predict the resonance frequency and bandwidth of a viscosity–density sensor first presented by Goodbread et al. [16]. The sensor was a torsional resonator with a non-cylindrical tip that was immersed in the fluid.

Predictions were compared with experiments conducted by Goodbread et al. [15]. For the first step, the inertial masses of the mass–spring system were fitted to the predicted and measured resonance frequencies. The outcome was that the experimentally derived inertial masses deviated by less than 5% from those derived from the geometry; thus, the model was in good agreement with the calculations. In the second step, the predicted and measured normalized bandwidths were compared. They were also largely in good qualitative and quantitative agreement. The relative deviation between the experiment and model prediction for the normalized bandwidth was approximately 10% for viscosities lower than 100 mPa·s. However, at higher viscosities, the numerical model systematically overpredicted the normalized bandwidth. Edge effects are a potential source of the deviation; they were neglected because a 2-D, rather than a 3-D, domain was used for the fluid simulation.

The proposed model proves to be an efficient estimator of the behavior of the viscosity–density sensor, facilitating computationally supported geometrical optimization, and it has the potential to significantly decrease the development time of next-generation sensors.

Acknowledgements

Funding: This research was partially funded by Innosuisse, grant number 27254.1

REFERENCES

[1] M. Heinisch, T. Voglhuber-Brunnmaier, E.K. Reichel, I. Dufour, B. Jakoby, Reduced order models for resonant viscosity and mass density sensors, Sensors Actuators, A Phys. 220 (2014) 76–84. https://doi.org/10.1016/j.sna.2014.09.006.

[2] M. Heinisch, T. Voglhuber-Brunnmaier, E.K. Reichel, I. Dufour, B. Jakoby, Application of resonant steel tuning forks with circular and rectangular cross sections for precise mass density and viscosity measurements, Sensors Actuators, A Phys. 226 (2015) 163–174. https://doi.org/10.1016/j.sna.2015.02.007.

[3] M. Heinisch, S. Clara, I. Dufour, B. Jakoby, A spiral spring resonator for mass density and viscosity measurements, Procedia Eng. 87 (2014) 1143–1146. https://doi.org/10.1016/j.proeng.2014.11.367.

[4] M. Heinisch, E.K. Reichel, I. Dufour, B. Jakoby, A U-shaped wire for viscosity and mass density sensing, Sensors Actuators, A Phys. 214 (2014) 245–251. https://doi.org/10.1016/j.sna.2014.04.020.

[5] H. Li, J. Wang, X. Li, D. Chen, Viscosity–density sensor with resonant torsional paddle for direct detection in liquid, IET Nanobiotechnology. 5 (2011) 121–125. https://doi.org/10.1049/iet-nbt.2011.0016.

[6] O. Cakmak, E. Ermek, N. Kilinc, G.G. Yaralioglu, H. Urey, Sensors and Actuators A: Physical

Precision density and viscosity measurement using two cantilevers with different widths, Sensors Actuators A. Phys. 232 (2015) 141–147. https://doi.org/10.1016/j.sna.2015.05.024.

[7] N. McLoughlin, S.L. Lee, G. Hähner, Simultaneous determination of density and viscosity of liquids based on resonance curves of uncalibrated microcantilevers, Appl. Phys. Lett. 89 (2006) 1–4184106. https://doi.org/10.1063/1.2374867.

[8] M.F. Khan, S. Schmid, P.E. Larsen, Z.J. Davis, W. Yan, E.H. Stenby, A. Boisen, Online measurement of mass density and viscosity of pL fluid samples with suspended microchannel resonator, Sensors Actuators, B Chem. 185 (2013) 456–461. https://doi.org/10.1016/j.snb.2013.04.095.

[9] S.B. Ć, M. Bukurov, M.B. Ć, S. Tašin, I. Pavkov, M.R.Č. In, Liquid viscosity determination by Coriolis flow meter, J. Process. Energy Agric. 4487 (2010) 178–182.

[10] J. Dual, Experimental methods in wave propagation in solids and dynamic viscometry, ETH Zürich, 1989, PhD dissertation.

[11] M. Fuchs, W. Drahm, C. Matt, A. Wenger, A Coriolis meter with direct viscosity measurement, Flomeko. (2003) 1–5.

[12] S. Clara, H. Antlinger, F. Feichtinger, A.O. Niedermayer, T. Voglhuber-Brunnmaier, B. Jakoby, A balanced flow-through viscosity sensor based on a torsionally resonating pipe, Proc. IEEE Sensors. 2017-Decem (2017) 1–3. https://doi.org/10.1109/ICSENS.2017.8234137.

[13] N. Mahmoodi, C.J. Anthony, Air damping simulation of MEMS torsional paddle, Excerpt from Proc. 2014 COMSOL Conf. (2014) 15–18.

[14] E.K. Reichel, T. Voglhuber-Brunnmaier, B. Jakoby, Fluid impedance model for resonator viscosity sensors, Procedia Eng. 168 (2016) 1012–1015. https://doi.org/10.1016/j.proeng.2016.11.328.

[15] J. Goodbread, D. Brunner, K. Haeusler, S. Kumar, A Viscosity-–density sensor based on torsional vibrations, Unpublished manuscript. (2020).

[16] J. Goodbread, S. Kumar, K. Häusler, B. Zybach, Temperature compensated density viscosity sensor having a resonant sensing element, United States patent US 10,502,670, 2016.

[17] T. Brack, Multi-frequency phase control of a torsional oscillator for applications in dynamic fluid sensing, ETH Zürich, PhD dissertation. https://doi.org/https://doi.org/10.3929/ethz-a-010867290.

[18] D. Brunner, H. Khawaja, M. Moatamedi, G. Boiger, CFD modelling of pressure and shear rate in torsionally vibrating structures using ANSYS CFX and COMSOL Multiphysics, Int. Jounal J. Multiphysics. 12 (2018) 349–358. https://hdl.handle.net/10037/14261

Paper III

CFD modeling of pressure and shear rate in torsionally vibrating structures using ANSYS CFX and COMSOL Multiphysics

D. Brunner[1,2], H. Khawaja[2], and M. Moatamedi[2], G. Boiger[1]

The international Journal of Multiphysics, Vol. 12, no. 4, pp. 349–358, 2018.

1. ZHAW, Zurich University of Applied Sciences, Switzerland
2. UIT, The Arctic University of Norway

Author contributions:

- D. Brunner conducted all numerical simulations in COMSOL Multiphysics.
- D. Brunner conducted all numerical simulations in ANSYS CFX with inputs from H. Khawaja
- D. Brunner has written the draft.
- H. Khawaja, M. Moatamedi and G. Boiger proofread the draft and suggested improvements.
- The idea of comparing different numerical codes originated from both D. Brunner and H. Khawaja.
- D. Brunner did the postprocessing with inputs from H. Khawaja

Organizations contributions:

- COMSOL Multiphysics® license were supplied by ZHAW
- ANSYS CFX® license were supplied by UiT
- MATLAB® license was provided by ZHAW

Funding:

- This research was partially funded by Innosuisse, grant number 27254.1

CFD modelling of pressure and shear rate in torsionally vibrating structures using ANSYS CFX and COMSOL Multiphysics

D Brunner[1,2]*, H Khawaja[2], M Moatamedi[2], G Boiger[1]

1. ZHAW, Technikumstrasse 9, CH - 8401 Winterthur
2. UiT-The Arctic University of Norway

ABSTRACT

This paper discusses numerical methodologies to simulate micro vibrations on a nontrivial torsionally oscillating structure. The torsional structure is the tip of a viscosity-density sensor using micro vibrations to measure the fluid properties. A 2D transient simulation of the fluid domain surrounding the tip of the sensor has been conducted in ANSYS CFX and COMSOL Multiphysics software. ANSYS CFX uses a frame of reference to induce the micro vibration whereas a moving wall approach is used in COMSOL Multiphysics for the full Navier-Stokes equation as well as their linearized form. The shear rate and pressure amplitude have been compared between the different numerical approaches. The obtained results show good agreement for both pressure and shear rate amplitudes in all models.

1. INTRODUCTION

Traditionally, the viscosity of a fluid is measured by analysing a sample with common laboratory instruments. Typical laboratory instruments include rotating cylinders or cones. These methods are time consuming, expensive and difficult to automate. Mechanical resonators, however, are a promising alternative to conventional laboratory equipment. These sensors are very robust, have no moving parts and are therefore suited for online measurements. Possible applications involve studying viscoelastic behaviour of polymers, determining a fluid's density and viscosity [1]–[9], characterising mechanical properties of polymer membranes and thin films [10]–[15], or detecting biomolecules and nanoparticle masses [16]–[21].

The working principle of these resonators is based on the change of natural frequency and damping due to the contact with a fluid. To measure damping and frequency shift, the resonator is excited close to a natural frequency while immersed in the fluid. The fluid interaction with the sensor creates an additional damping as well as a shift of resonance frequency in comparison to the resonator in a vacuum. The additional damping is due to the viscous shear stresses of the fluid whereas the frequency shift is due to the displacement of fluid mass.

For simple geometries such as cylinders, analytical solutions can be found. However, for nontrivial geometries numerical simulations are required to investigate the induced forces by shear stresses and pressure. These forces are crucial to make predictions about the characteristics of the sensor in future studies.

*Corresponding Author: brni@zhaw.ch

In this paper, the shear stresses and pressure forces are computed over a non-trivial torsional oscillating structure. To assure that the numerical predictions as well as the underlying CFD equations are appropriate for solution, two different approaches, namely a finite element method in COMSOL Multiphysics and a finite volume method in ANSYS CFX, are compared. The goal is to investigate whether the numerical method (e.g., finite element vs. finite volume), has any impact on the solution. Motion is induced differently in the two programs; hence the comparison would reflect not only on the correctness of the models but also their suitability for the solution. COMSOL Multiphysics uses a moving wall approach, whereas ANSYS CFX induces motion in the domain by a frame of reference.

The subject of this study is part of a torsional resonator which can be used for viscosity-density measurement. Figure 1 shows the cross-section of the oscillating structure which is in contact with the fluid as well as the mesh used in COMSOL. The interest lies in modelling the flow around the structure (see figure 1) where the torsional motion is around the z-axis (through the centre of the cylinder). To reduce the computational effort only a cross section of the sensor tip is used. This simplification can be made because there is no change of fluid motion in axial direction.

The simulations are conducted at a representative excitation amplitude and frequency. A typical value of the excitation frequency is 8000 Hz with an amplitude of 0.001 rad. This amplitude is much smaller than any geometrical length scale.

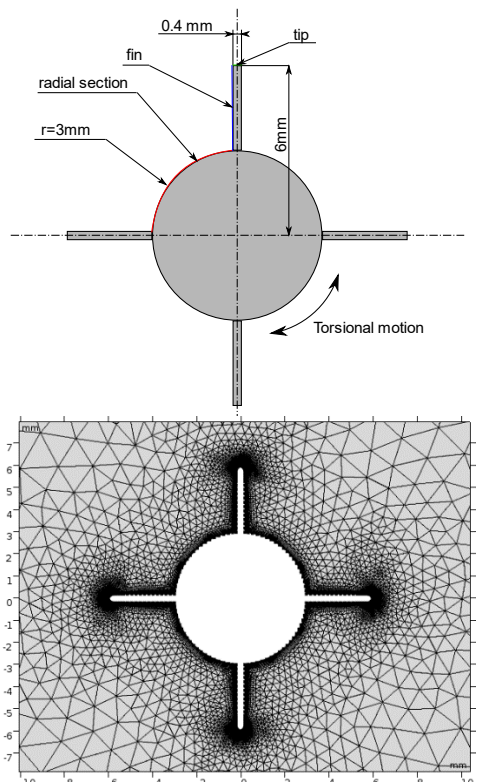

Figure 1: Geometry and mesh of the sensor tip of a viscosity and density sensor.

2. METHODOLOGY

The underlying physics of the micro vibrations can be described by the incompressible Navier-Stokes equation. The micro vibration can be induced by either a moving wall or a frame of reference, where additional source terms are required to be added in the Navier-Stokes equations.

2.1 Moving Wall Approach

In the moving wall approach, the motion is induced at the boundary. The torsional oscillation is around the axis $\overrightarrow{e_z}$ which is normal to the computational domain and in the center of the cylindrical structure. The time depended wall velocity $\vec{u}_{sensor}$ of the boundary is defined by Equation 1, where $\vec{r}$ is the distance from the axis the boundary, X the oscillation amplitude and ω the angular frequency.

$$\vec{u}_{sensor} = X \sin(\omega t)\,(\vec{r} \times \overrightarrow{e_z}) \tag{1}$$

Within the domain, the incompressible Navier-Stokes equation and continuity equation can be solved, as in equations 2 & 3,

$$\nabla \cdot \vec{u} = 0 \tag{2}$$

$$\frac{\partial \vec{u}}{\partial t} + \vec{u} \cdot \nabla \vec{u} \;=\; \frac{-\nabla p}{\rho} + \nu \Delta \vec{u} \tag{3}$$

where ν is the kinematic fluid viscosity, ρ the fluid density, p the pressure and $\vec{u}$ the velocity.

2.2 Linearized Moving Wall Approach

The amplitude of the induced torsional oscillation is very small. Due to these small amplitudes, the convective nonlinear part of the Navier-Stokes equation is negligible. Thus, the convective part of the momentum equation can be neglected, equation 4. The continuity equation as well as the moving boundary remains unchanged, equations 1 & 2.

$$\frac{\partial \vec{u}}{\partial t} = -\frac{\nabla p}{\rho} + \nu \Delta \vec{u} \tag{4}$$

2.3 Frame of Reference

Instead of inducing the torsional vibration on the wall, the frame of reference approach induces the motion in the domain. Thereby, the centrifugal acceleration $\overrightarrow{\Omega} \times \overrightarrow{\Omega} \times \vec{r}$, Coriolis acceleration $2\overrightarrow{\Omega} \times \vec{u}$ and Euler acceleration $\frac{\partial \overrightarrow{\Omega}}{\partial t} \times \vec{r}$ are added, see equation 6. The continuity remains unchanged, equation 7. The motion of the domain is described by $\overrightarrow{\Omega}$, equation 5.

$$\overrightarrow{\Omega} = \mathrm{X}\,\overrightarrow{e_z} \cdot \sin(\omega t) \tag{5}$$

$$\frac{\partial \vec{u}}{\partial t} + \vec{u} \cdot \nabla \vec{u} + 2\overrightarrow{\Omega} \times \vec{u} + \overrightarrow{\Omega} \times \overrightarrow{\Omega} \times \vec{r} + \frac{\partial \overrightarrow{\Omega}}{\partial t} \times \vec{r} = -\frac{\nabla p}{\rho} + \nu \Delta \vec{u} \tag{6}$$

$$\nabla \cdot \vec{u} = 0 \tag{7}$$

Because the motion is induced in the domain, the boundary of the oscillating structure is not moving. Thus, a nonslip boundary condition is needed for the sensor tip.

2.4 Mesh

The meshes have been created within each software individually using tetrahedral elements and checked for sensitivity. The boundary layer at the wall has been resolved using 18 mesh layers with a growth rate of 1.2 for a minimal boundary layer thickness of 1 µm. This thickness was found to be sufficient to resolve the flow in the vicinity of the boundary. The mesh used in COMSOL is shown in figure 1. The mesh created in ANSYS has the same properties.

3. DISCUSSION AND RESULTS

To compare the solution of the different methods described in chapter 2, the forces at the boundary were compared. These forces are important to eventually determine the impact of the fluid on the sensing structure. The local forces can be decomposed into two different categories: Shear stresses and pressure forces. The shear stresses are described by shear rate γ, which is the norm of the velocity derivative with respect to the surface normal $\vec{n}$. Both pressure p and shear rate are purely harmonic and can be describe by an amplitude and their respective phase (ϕ_v for γ and ϕ_p for p), equation 8 & 9, once quasi-steady state conditions are achieved.

$$\left|\frac{\vec{u}(x,y,t)}{\partial \vec{n}}\right| = \gamma(x,y) \cdot \sin\left(\omega t + \phi_v(x\,,y)\right) \tag{8}$$

$$\mathrm{p}(x,y,t) = \mathrm{p}(x,y) \cdot \sin\left(\omega t + \phi_p(x\,,y)\right) \tag{9}$$

The structure shown in figure 1 had 3 different geometrical features: tip, fin and radial section. The amplitude of the shear stress and pressure computed by the different models were compared on the three different geometrical features and discussed in the following sections.

3.1. Comparison of the Shear Stresses between Different Models

The shear stress amplitude predicted by three different models:

- moving wall approach (shown as COMSOL laminar)
- linearized moving wall approach (shown as COMSOL lin)
- frame of reference (shown as ANSYS CFX)

Shear rates for each of the model are shown in figure 2 for the tip, figure 3 for the fin and figure 4 for the radial section. Even though the models are based on different equations and numerical methods, they show an overall good agreement for both computed viscosities 2 and 20 mPas with a constant density of 1000kg/m³.

The shear stresses are highest over the tip section due to the increased boundary velocity caused by the larger distance from the rotational center. The shear rate shows minute oscillations as the tip approaches the fin. These oscillations are caused by interpolation

between the boundary points due to the curvature of the geometry. Thus, the oscillations are a numerical artifact and have a minimal contribution to the overall torque on the structure (below 0.5%).

The shear rate amplitude over the fin shows a good agreement between all three models. All models show a minimum in shear rate at the location 1.35 mm as shown in Figure 3, where 0 mm is at the radial position and 3 mm is at the edge. The shear rate increases dramatically with increasing distance from the rotational center and reaches a maximum of 3 mm at the edge of the tip. On the other end of the fin touching radial section, the shear rate drops significantly.

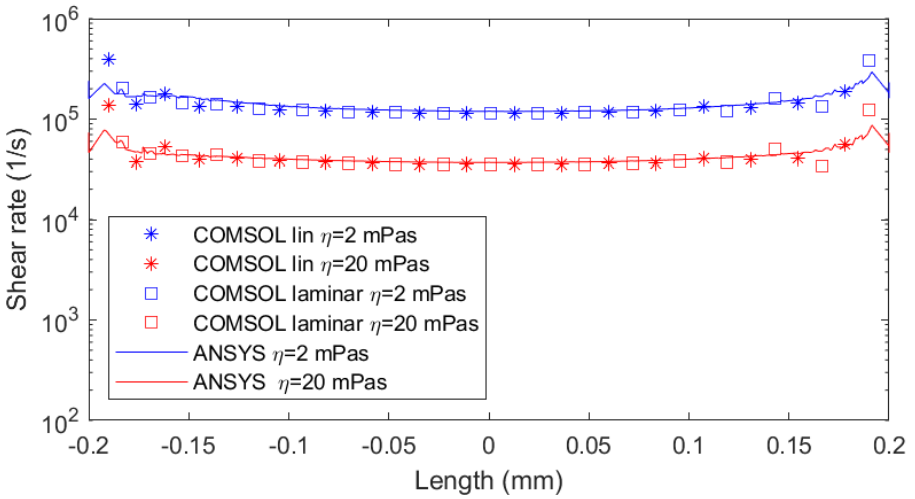

Figure 2: Comparison of shear rates amplitudes over the tip between COMSOL Multiphysics (full and linearized version of the Navier-Stokes equation) and ANSYS CFX.

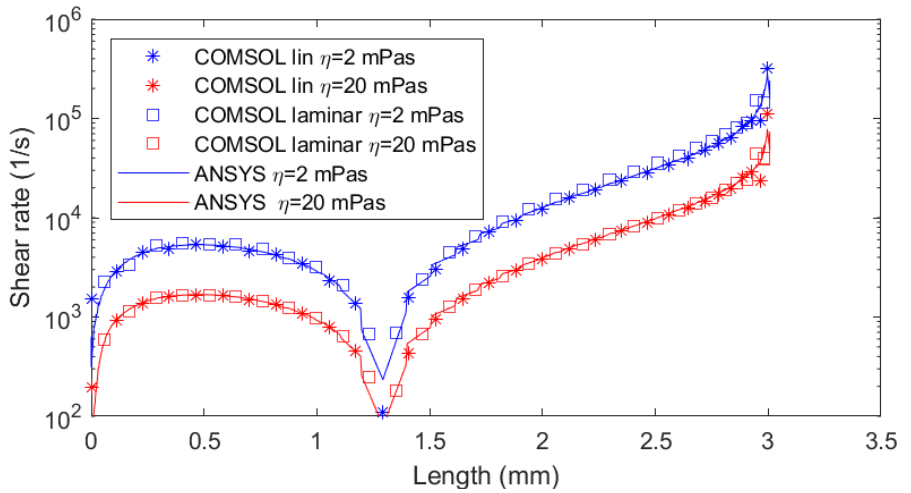

Figure 3: Comparison of shear rates amplitudes over the fin between COMSOL Multiphysics (full and linearized version of the Navier-Stokes equation) and ANSYS CFX.

The radial section shows lower shear rates in comparison to the other sections. The smaller shear rates are caused by the smaller distance to the rotational center as well as the effects of the fins. The fins constrain the flow at the edges of the radial section and increase the flow near the edges. The shear rates decrease in the middle region of the radial section. In absolute terms, there is a minor discrepancy between the results computed by ANSYS CFX and COMSOL. Even though the relative differences are high, the absolute difference is about 2 orders of magnitude lower than on the tip. Thus, it has a negligible effect on the overall forces.

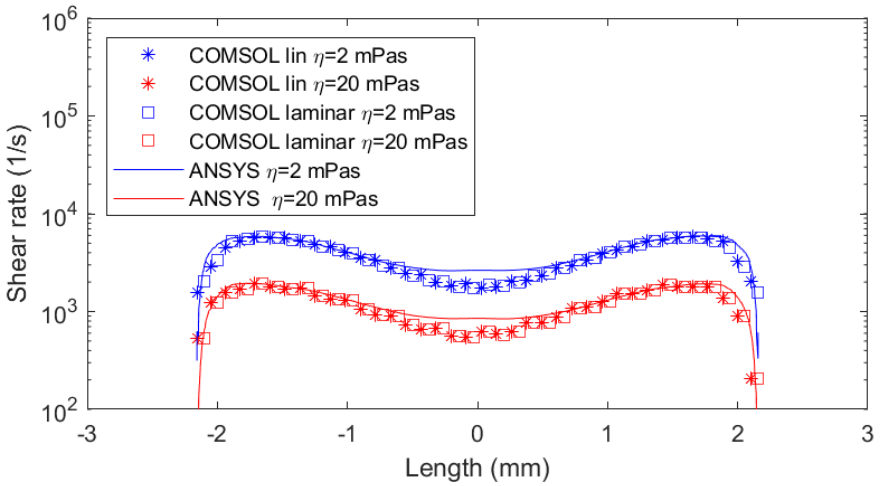

Figure 4: Comparison of shear rates amplitudes over the radial section between COMSOL Multiphysics (full and linearized version of the Navier-Stokes equation) and ANSYS CFX.

3.2. Comparison of the Pressure Amplitude between the Different Models

The pressure amplitudes are shown over the same structural elements as the shear rates in Figure 5 for the tip, figure 6 for the fin and figure 7 for the radial section. The viscosity of the fluid has a very small impact on the pressure amplitude, therefore the figures show the results for η = 2mPas only.

The pressure amplitudes over the tip and radial section approaches zero in the center of the section. This drop in the pressure amplitudes are caused by the symmetry of the structure. The location of the drop is also the position of a structural symmetry line. Considering the symmetry line through the center of the fin, one side of the fin is pushing the fluid away and the other side is pulling towards it. Thus, the pressure is positive on the pushing side and negative on the pulling side. This effect can be visualized by the phase value of the pressure. In the radial section, the phase of the pressure amplitude changes from 0 to 180° at the central point, which indicates that the pressure switches from negative to positive, hence must be zero in the center in order to be observe the continuum, see figure 8. Due to the symmetry, the tip section shows the same phenomena, see figure 5. The simulations conducted in COMSOL Multiphysics captured this phenomenon sharper than ANSYS CFX. The ANSYS CFX simulation shows a slightly wider transition area for negative to plus in comparison to COMSOL Multiphysics.

The pressure distribution over the fin does not exhibit a sudden drop due to symmetry. The pressure amplitude constantly increasing with the length (from radial section) up to the location 1.3 mm, after which the shear rate drops again. Past this local maximum of the pressure amplitude, it decreases with steadily increasing slope towards the tip.

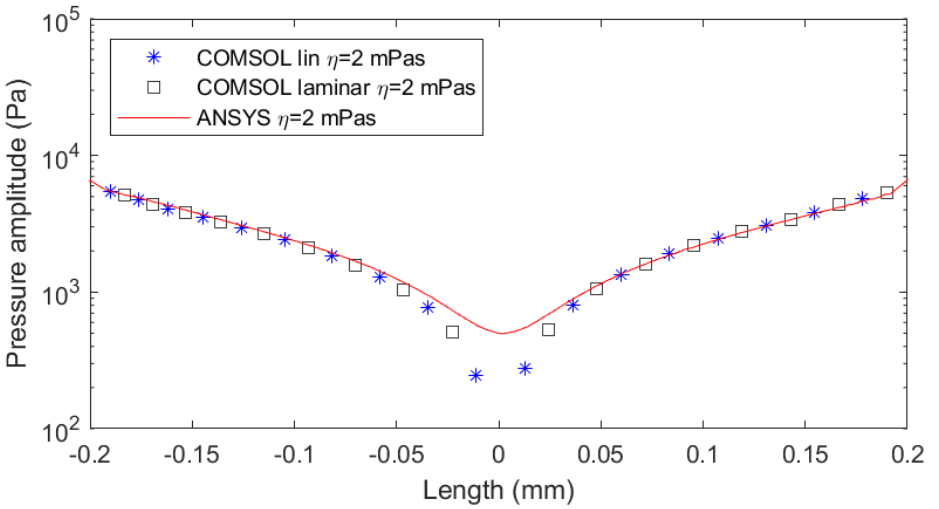

Figure 5: Comparison of the pressure amplitudes over the tip between COMSOL Multiphysics (full and linearized version of the Navier-Stokes equation) and ANSYS CFX.

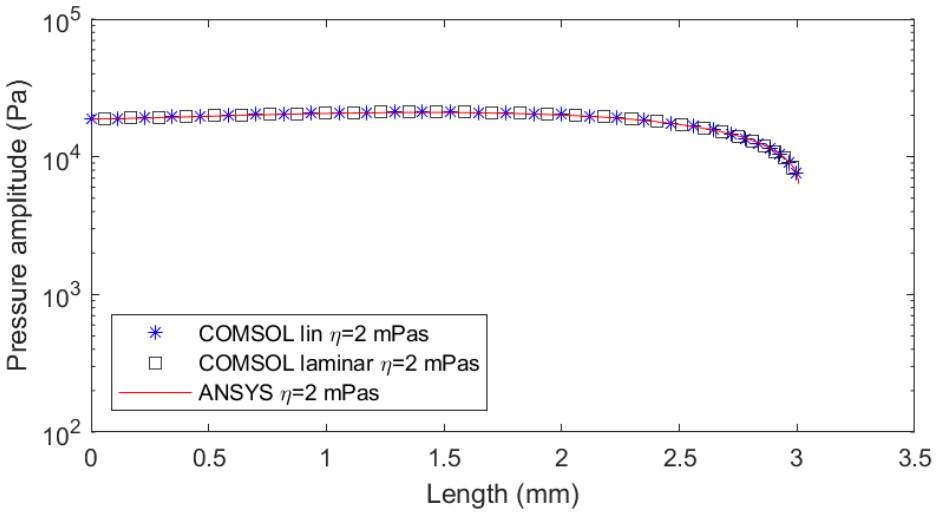

Figure 6: Comparison of the pressure amplitudes over the fin between COMSOL Multiphysics (full and linearized version of the Navier-Stokes equation) and ANSYS CFX.

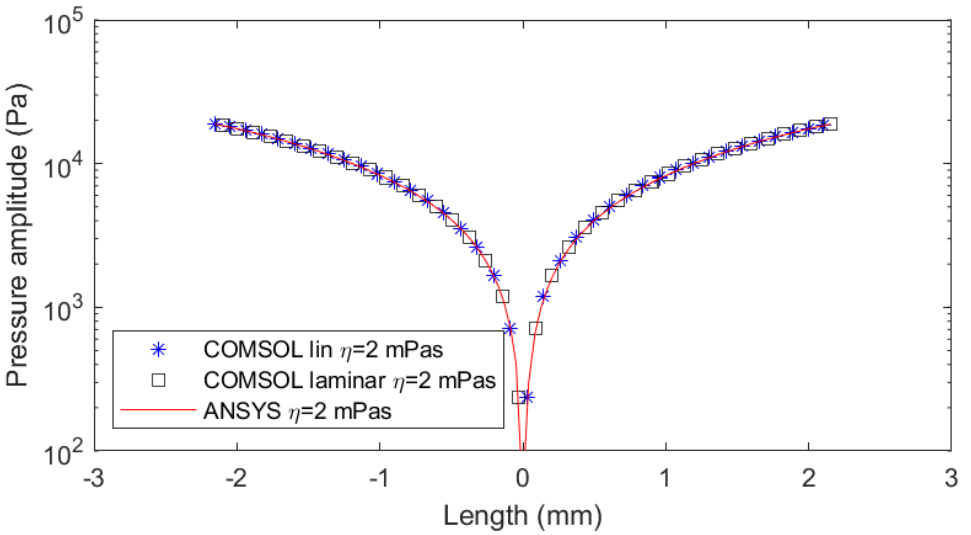

Figure 7: Comparison of the pressure amplitude over the radial section between COMSOL Multiphysics (full and linearized version of the Navier-Stokes equation) and ANSYS CFX.

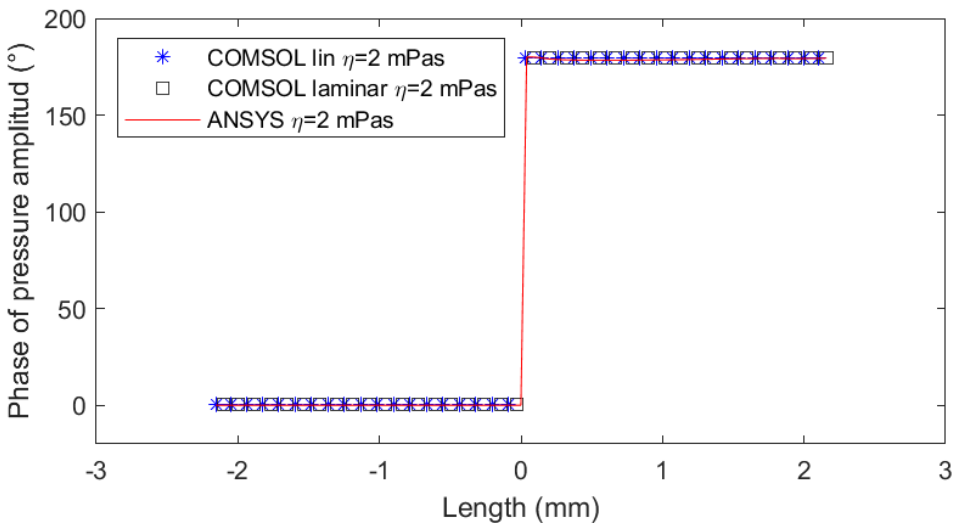

Figure 8: Comparison of the phase of the pressure over the radial section between COMSOL Multiphysics (full and linearized version of the Navier-Stokes equation) and ANSYS CFX.

4. CONCLUSION

The flow field around a torsional oscillating structure was computed with COMSOL Multiphysics and ANSYS CFX. Three different methodologies were adopted. In ANSYS CFX, a change in the frame of reference induced motion within the bulk of the fluid whereas in COMSOL Multiphysics, a moving wall approach was used to induce the motion. In COSMOL Multiphysics, both the full Navier-Stokes equation as well as the linearized form were solved. Pressure and shear stresses at the boundary are purely harmonic oscillations once a quasi-steady state has been reached. The pressures and shear rate amplitudes at the different geometrical sections of the structure were compared between the different numerical approaches and found to be in good agreement.

In COMSOL Multiphysics, the linearized version of the Navier Stokes equations was compared to the full equation. At low viscosities (2mPas), there were small differences between the linearized and nonlinear solution in COMSOL. These differences diminished as the viscosity increased towards 20mPas. Overall, the agreement between the models were sufficient.

The good agreement between the different numerical methods and different models shows a potential for predicting the forces on micro vibrating structures immersed in fluid. Based on these results, more complex models can be developed to study the effects of fluid-structure interactions.

REFERENCES

[1] M. Papi, G. Maulucci, G. Arcovito, P. Paoletti, M. Vassalli, and M. De Spirito, "Detection of microviscosity by using uncalibrated atomic force microscopy cantilevers," Appl. Phys. Lett., vol. 93, no. 12, 2008.

[2] M. K. Ghatkesar et al., "Resonating modes of vibrating microcantilevers in liquid," Appl. Phys. Lett., vol. 92, no. 4, pp. 10–13, 2008.

[3] M. Papi, G. Arcovito, M. De Spirito, M. Vassalli, and B. Tiribilli, "Fluid viscosity determination by means of uncalibrated atomic force microscopy cantilevers," Appl. Phys. Lett., vol. 88, no. 19, 2006.

[4] W. Y. Shih, X. Li, H. Gu, W. H. Shih, and I. A. Aksay, "Simultaneous liquid viscosity and density determination with piezoelectric unimorph cantilevers," J. Appl. Phys., vol. 89, no. 2, pp. 1497–1505, 2001.

[5] N. McLoughlin, S. L. Lee, and G. Hähner, "Simultaneous determination of density and viscosity of liquids based on resonance curves of uncalibrated microcantilevers," Appl. Phys. Lett., vol. 89, no. 18, pp. 1–4, 2006.

[6] M. K. Ghatkesar, E. Rakhmatullina, H. P. Lang, C. Gerber, M. Hegner, and T. Braun, "Multi-parameter microcantilever sensor for comprehensive characterization of Newtonian fluids," Sensors Actuators, B Chem., vol. 135, no. 1, pp. 133–138, 2008.

[7] M. Thompson, A. L. Kiplingt, and W. C. Duncan-hewitts, "Thickness-shear-mode Acoustic Wave Sensors in the Liquid Phase A Review," vol. 116, no. September, 1991.

[8] L. Tessler, F. Patat, N. Schmitt, G. Feuillard, and M. Thompson, "Effect of the Generation of Compressional Waves on the Response of the Thickness-Shear Mode Acoustic Wave Sensor in Liquids," Anal. Chem., vol. 66, no. 21, pp. 3569–3574, 1994.

[9] K. Keiji Kanazawa and J. G. Gordon, "The oscillation frequency of a quartz resonator in contact with liquid," Anal. Chim. Acta, vol. 175, no. C, pp. 99–105, 1985.

[10] L. Huang, J. Chen, T. Cao, H. Cong, and W. Cao, “Investigation of microtribological properties of C60-containing polymer thin films using AFM/FFM,” Wear, vol. 255, no. 7–12, pp. 826–831, 2003.

[11] S. Kim, D. Lee, M. Yun, N. Jung, S. Jeon, and T. Thundat, “Multi-modal characterization of nanogram amounts of a photosensitive polymer,” Appl. Phys. Lett., vol. 102, no. 2, pp. 2–6, 2013.

[12] S. Bistac, M. Schmitt, A. Ghorbal, E. Gnecco, and E. Meyer, “Nano-scale friction of polystyrene in air and in vacuum,” Polymer (Guildf)., vol. 49, no. 17, pp. 3780–3784, 2008.

[13] F. Martin, M. I. Newton, G. McHale, K. A. Melzak, and E. Gizeli, “Pulse mode shear horizontal-surface acoustic wave (SH-SAW) system for liquid based sensing applications,” Biosens. Bioelectron., vol. 19, no. 6, pp. 627–632, 2004.

[14] M. V. Voinova, M. Rodahl, M. Jonson, and B. Kasemo, “Viscoelastic acoustic response of layered polymer films at fluid-solid interfaces: Continuum mechanics approach,” 1998.

[15] R. Lucklum, C. Behling, R. W. Cernosek, and S. J. Martin, “Determination of complex shear modulus with thickness shear mode resonators,” J. Phys. D. Appl. Phys., vol. 30, no. 3, pp. 346–356, 1997.

[16] J. Xie and Y. Hu, “A two-dimensional model on the coupling thickness-shear vibrations of a quartz crystal resonator loaded by an array spherical-cap viscoelastic material unit”, Ultrasonics, vol. 71, pp. 194–198, 2016.

[17] S. Dohn, O. Hansen, and A. Boisen, “Cantilever based mass sensor with hard contact readout,” Appl. Phys. Lett., vol. 88, no. 26, pp. 1–4, 2006.

[18] H. P. Lang, M. Hegner, and C. Gerber, “Cantilever Array Sensors for Bioanalysis and Diagnostics,” Nanobiotechnology II More Concepts Appl., vol. 8, no. 4, pp. 175–195, 2007.

[19] R. Datar, A. Passian, R. Desikan, and T. Thundat, “Microcantilever biosensors,” Proc. IEEE Sensors, vol. 37, no. 2005, p. 5, 2007.

[20] A. I. Fedorchenko, I. Stachiv, and W.-C. Wang, “Method of the viscosity measurement by means of the vibrating micro-/nano-mechanical resonators,” Flow Meas. Instrum., vol. 32, pp. 84–89, 2013.

[21] L. Qin, H. Cheng, J. M. Li, and Q. M. Wang, “Characterization of polymer nanocomposite films using quartz thickness shear mode (TSM) acoustic wave sensor,” Sensors Actuators, A Phys., vol. 136, no. 1, pp. 111–117, 2007.

Paper IV

Analysis of a Tubular Torsionally Resonating Viscosity Sensor

D. Brunner[1,2], J. Goodbread[3], K. Häusler[3], S. Kumar[3], G. Boiger[1], H. Khawaja[2],
MDPI Sensors, Submitted manuscript, 2020
1. ZHAW, Zurich University of Applied Sciences, Switzerland
2. UIT, The Arctic University of Norway
3. Rheoncis GmbH, Switzerland

Author contributions:

- D. Brunner, K. Häusler and J. Goodbread conceptualized the study
- D. Brunner, J. Goodbread and H. Khawaja did the methodology
- D. Brunner did all numerical work
- D. Brunner and J. Goodbread did the experimental validation
- D. Brunner and H. Khawaja did the numerical validation
- S. Kumar and G. Boiger provided the resources
- D. Brunner prepared the draft
- D. Brunner, J. Goodbread, S. Kumar and H. Khawaja did review and editing
- D. Brunner did the visualization
- H. Khawaja, J. Goodbread and G. Boiger did the supervision
- G. Boiger and S. Kumar did the project administration
- G. Boiger and S. Kumar did the funding acquisition
-

Organizations contributions:

- MATLAB® license was provided by ZHAW
- Experimental equipment was provided by Rheonics GmbH

Funding:

- This research was partially funded by Innosuisse, grant number 27254.1

sensors

MDPI

Article

Analysis of a Tubular Torsionally Resonating Viscosity–Density Sensor

Daniel Brunner [1,2,*], Joe Goodbread [3,*], Klaus Häusler [3], Sunil Kumar [3], Gernot Boiger [1] and Hassan A. Khawaja [2]

[1] Institute of Computational Physics, Zurich University of Applied Sciences, ZHAW, 8400 Winterthur, Switzerland; boig@zhaw.ch

[2] Faculty of Engineering Science and Technology, Department of Automation and Process Engineering, The Arctic University of Norway, UiT, P.O. Box 6050 Langnes, 9037 Tromsø, Norway; hassan.a.khawaja@uit.no

[3] Rheonics GmbH, 8406 Winterthur, Switzerland; klaus.haeusler@rheonics.com (K.H.); sunil.kumar@rheonics.com (S.K.)

* Correspondence: brni@zhaw.ch (D.B.); joe.goodbread@rheonics.com (J.G.)

Received: 9 April 2020; Accepted: 25 May 2020; Published: 27 May 2020

Abstract: This paper discusses a state-of-the-art inline tubular sensor that can measure the viscosity–density ($\rho\eta$) of a passing fluid. In this study, experiments and numerical modelling were performed to develop a deeper understanding of the tubular sensor. Experimental results were compared with an analytical model of the torsional resonator. Good agreement was found at low viscosities, although the numerical model deviated slightly at higher viscosities. The sensor was used to measure viscosities in the range of 0.3–1000 mPa·s at a density of 1000 kg/m^3. Above 50 mPa·s, numerical models predicted viscosity within ±5% of actual measurement. However, for lower viscosities, there was a higher deviation between model and experimental results up to a maximum of ±21% deviation at 0.3 mPa·s. The sensor was tested in a flow loop to determine the impact of both laminar and turbulent flow conditions. No significant deviations from the static case were found in either of the flow regimes. The numerical model developed for the tubular torsional sensor was shown to predict the sensor behavior over a wide range, enabling model-based design scaling.

Keywords: viscometer; viscosity–density sensor; viscosity measurement; torsional resonator; fluid–structure interaction

1. Introduction

Traditionally, viscosity is measured by sampling and analyzing fluids with common laboratory viscometers or rheometers. These instruments are time consuming, error prone, expensive, and prohibit a fast and automated system response. Sensors based on mechanical resonance, however, are a promising alternative to conventional laboratory equipment. These sensors are robust, have no moving parts, and are, therefore, suited to real-time measurements. Using sensors based on resonance, various materials can be investigated for different purposes, such as studying the viscoelastic behavior of polymers, determining fluid density and viscosity [1–8], characterizing the mechanical properties of polymer membranes and thin films [9–14], and detecting biomolecule or nanoparticle masses [15–20]. Sensors using torsional vibration are a subgroup of mechanical resonators. If purely cylindrical, these sensors create pure shear stresses and do not increase mass displacement, such as tuning forks or cantilevers. This makes them more robust, and measurement less sensitive towards, e.g., wall effects.

Sensors based on torsional vibration have been investigated to measure viscous and viscoelastic effects [21–24]. Probe-style sensors are already commercially available (e.g., Rheonics, Hydramotion,

Sofraser, Brookfield, and Emerson). Experimental and numerical studies have been conducted on how to measure viscosity [25–29]. Furthermore, they have been used to characterize viscoelastic fluids [21].

It is advantageous to have a nonintrusive viscosity sensor to monitor industrial processes. Thereby, the sensor should neither create an obstruction in the piping system nor influence the flow field inside the tube.

Häusler and Reinhart et al. [26,30] designed a tubular sensor on the basis of a small tube to measure blood viscosity. The sensor consisted of a small tube with an inner diameter of 2 mm that was excited in a torsional mode. The damping of the mode was measured and correlated to fluid viscosity within the tube. This system was used to measure blood viscosity at different hematocrits.

Fuchs and Drahm et al. [31] built a tubular sensor to measure the mass flow rate, fluid density and viscosity. The sensor was based on a straight tube with an attached eccentric mass. The system oscillated in a superposition of torsional and transverse modes, which allowed the Coriolis effect to be measured. In addition, due to fluid displacement, the resonance frequency of the excited mode could be correlated with fluid density. The novelty in this design was that the sensor could measure the damping of the mode. Damping is caused by the shear stresses within the fluid due to torsional vibration. Thus, the sensor was capable of measuring the mass flow rate, viscosity, and density.

This study presents a tubular sensor that could measure the viscosity (at a known density) under the conditions of internal flow. The design is based on the tubular sensor introduced by Häusler [26,30]. It was adapted to measure a wide range of viscosities. Additionally, the sensor was designed as a flow-through device, which can be integrated into piping systems and does not obstruct the flow. The resonator of the sensor oscillates in a purely torsional mode; thus, it cannot measure flow rate or fluid density like the tubular sensor designed by Fuchs and Drahm [31]. However, because no eccentric mass is needed, the overall inertia of the resonator is smaller than that with eccentric mass. Thus, the ratio between fluid-induced damping and inertia is higher, and the sensor is more sensitive towards damping. This enables greater accuracy, especially for low viscosities. Therefore, the benefit of the new tubular sensor is higher accuracy at low viscosities in comparison to the tubular sensor presented by Fuchs and Drahm [31].

To gain deeper insight into the working principle of the sensor, the sensor was numerically modelled using a weak fluid–structure interaction. This model will provide the means for dimensional scaling of the sensor while meeting sensor's measuring range and accuracy specifications. For validation, the predicted damping values were verified by comparing them with measurements under static conditions, meaning no internal flow and thermally uniform conditions. However, the sensor eventually operated under conditions where internal flow is present. Thus, it was crucial to investigate the sensitivity of measurement to internal flow to reliably and accurately conduct measurements to reflect actual industrial use case. Therefore, the sensor was inserted into a flow loop, and tested with different fluids and in the laminar and turbulent flow regime.

2. Sensor Design and Experiments

The tubular sensor uses a thin-walled, straight, stainless-steel tube as the sensor body. The fluid flows through the tubular sensor without any interruption. This allows the tubular sensor to be directly integrated into a process line.

The working principle of the tubular sensor is based on torsional resonance. The first torsional mode of the tubular resonator is excited at a frequency similar to its natural frequency. The excited resonance creates motion in the fluid. The shear stresses caused by the fluid motion induce a torque on the sensor, which damps oscillation. Oscillation damping is measured and related to fluid properties.

2.1. Tubular Sensor Design

The schematic of the tubular sensor is shown in Figure 1. The resonator was comprised of a thin-walled, stainless-steel (316 L) tube with an inner diameter of 5.25 mm and with two large disks mounted onto the outer diameter. The two disks are spaced 100 mm apart. The section between these disks is the measurement section, where the first torsional mode was excited via two permanent magnets that are mounted onto the tube. These magnets were driven by electromagnets, which

produced an oscillating torque near the natural frequency of the first torsional mode. This driving torque was turned off after sufficient energy has been provided to the resonator. Then, the decay in torsional oscillation was measured using electromagnets. On the basis of the measured signal, the logarithmic decrement and the resonance frequency f_0 of the resonator were computed. Damping was expressed as bandwidth Γ, which was computed on the basis of the logarithmic decrement. Additionally, temperature was measured by a PT1000 RTD (Honeywell, Berkshire, UK) mounted on the tube.

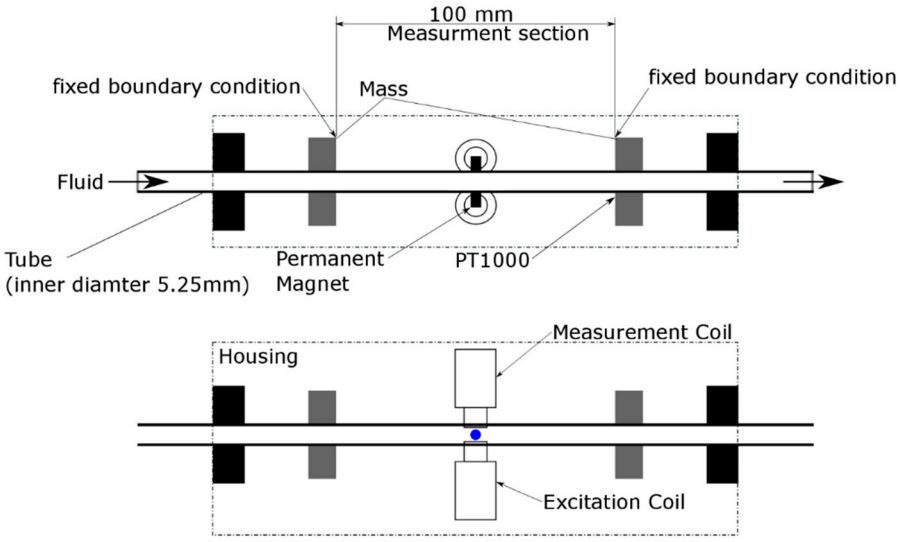

Figure 1. Experimental setup of tubular sensor.

2.2. Static Experiment Procedure

Experiments were conducted under static conditions (tube filled with fluid with no internal flow) to determine damping at different well-defined viscosities and densities of the fluid. These experiments were used to determine whether the numerical model described in Section 2.4 agrees with the measurement as well as to check consistency for different fluids. To conduct the experimental measurements, the tube was filled with different NIST (National Institute of Standards and Technology) traceable viscosity reference fluids (N2, S6, S20, S60, N100, S200, and S600, from Cannon Instrument Company (State College, PA 16803, USA)). These fluids have a well-known viscosity and density as a function of temperature; thus, they are well suited for calibration and validation purposes. During calibration, the temperature varied between 20 and 100 °C. Once a target temperature was reached, it was held constant for long enough so that the sensor and fluid were under thermally uniform conditions.

The damping caused by the fluid is related to the product of viscosity and density, later denoted as $\rho\eta$ value, where ρ is the fluid density and η the dynamic viscosity. Each fluid covers a certain range of $\rho\eta$ values. However, all fluids are of similar density, and therefore, the driving change in damping is related to the fluid's viscosity. These ranges overlap; thus, two fluids are capable of producing the same damping ($\rho\eta$ value) at different temperatures.

This investigation was conducted in two different steps. In the first step, four fluids were used to create a baseline for the sensor. These first sets of fluids are marked in Figure 2 with full lines. They covered the entire operating range of the sensor and had some overlap of their temperature-dependent $\rho\eta$ value. In the second step, baseline validity was tested with additional fluids S20 and S200, marked with dashed lines in Figure 2.

During measurement, sensor damping and resonance frequency were determined. The measured damping of the sensor was the superposition of intrinsic material damping and fluid-induced damping. To determine fluid-induced damping, intrinsic damping was subtracted from the measured damping value. The intrinsic damping of the sensor was temperature dependent and measured prior to fluid

measurements. Therefore, the clean sensor with no fluid inside the tube was measured with the same protocol as the filled sensor in the climate chamber.

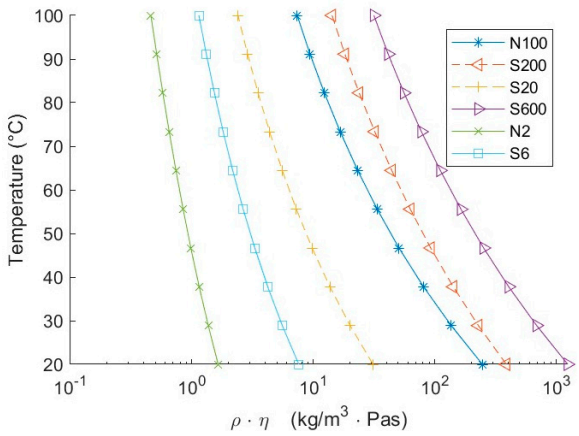

Figure 2. Product of viscosity and density (ρη) of fluids as a function of temperature. Solid lines are fluids used to create a baseline, and dashed lines are fluids used for validation.

For all measurements, sensor bandwidth was measured in intervals of approximately 1 s. One hundred measurements were used to calculate an averaged value of bandwidth, temperature, and resonance frequency. To estimate measurement uncertainty, error estimation was performed. There were two main contributions to the error: (1) intrinsic damping and (2) measuring damping value.

(1) An absolute error in the measured damping was caused by the intrinsic damping of the sensor. This error was independent of the damping value.
(2) Measurement of the damping value was more accurate at low damping due to higher signal-to-noise ratio. The relative error was 0.3% in air and increased to 30% for viscosities of 1000 mPas at a density of 1000 kg/m^3. This error could be reduced by averaging multiple measurements. Thus, by averaging 100 measurements, its contribution was reduced by ten-fold.

To determine the absolute viscosity (at a given density), the exact fluid properties at a given temperature during measurements were required. Temperature measurement was subject to its own error, creating uncertainty around the fluid properties during measurements. For the fluids used in this study, this error was approximately 3%.

2.3. Flow Loop Experiment

The tubular sensor was integrated into a flow loop to investigate the sensor sensitivity towards internal flow under realistic industrial conditions (as shown in Figure 3). Flow rate could be varied in the flow loop, allowing variation in the averaged flow velocity through the sensor from 2.3 to 10 m/s. A membrane pump (ZIP-80, Wagner (Altstätten, Switzerland)) was used to circulate the fluid, creating a pulsating flow. The flow rate was measured after the tubular sensor. Experiments were conducted at room temperature (27–32 °C) with a water–glycerol solution at 10 different concentrations (83%–8.3% W-G). Viscosities varied between 1 and 45 mPas at a density of approx. 1000 kg/m^3. At each concentration, five measurements at different flow rates were taken. These five measurements were compared to the static measurements (flow rate = 0).

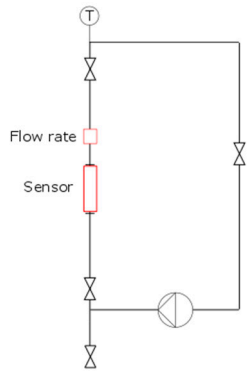

Figure 3. Flow loop schematic used for internal flow experiments (Reynolds number range of 500–50,000).

2.4. Resonator Modeling

The sensor could be modeled as a classic harmonic resonator, where temporal and structural parts are independently considered. To compute the shape of the torsional mode, the equation for torsional waves in nonhomogeneous cylindrical structures is solved, with the contribution of the attached magnets considered in a simplified manner. The inertial mass of the magnets was modelled by a larger cylindrical section. This larger cylindrical section increases the internal mass to account for the additional inertial mass of the attached magnets and stiffens the section of the larger cylinder. This larger cylindrical section is shown in Figure 4 (top) by the "magnet mass". The equation for torsional waves is shown as Equation (1),

$$\frac{\partial}{\partial x}\left(GI_p\right)\cdot\frac{\partial \Psi}{\partial x} - 2\pi R^2\tau + F = I_p\frac{\partial^2}{\partial t^2}\Psi \tag{1}$$

where Ψ, angular deflection; I_p, second moment area; x, axial direction; G, shear modulus; R, inner tube radius; F, excitation force; τ; viscous shear stress on the structure; and t, time.

We assumed that the solution of Equation (1) could be written by a space- and time-dependent function (see Equation (2)). Therefore, the temporal and structural parts could be solved independently.

$$\Psi(x,t) = \varphi(t)\cdot\hat{\Phi}(x) \tag{2}$$

To compute the shape of the structural mode, excitation and fluid forces were neglected. This weakly coupled fluid–structure interaction approach holds true for fluids with a low viscosity, where fluid-induced forces are much smaller than structural forces. At higher viscosities, the fluid may influence the shape of the structural mode. To compute the shape of the mode, we assumed that the angular deflection at the masses was zero because the moment of inertia was much higher than that of the tube. This defined the boundary conditions at the end of the measuring section ($\pm l/2$); see Equation (4).

$$G\frac{\partial}{\partial x}\left(I_p\cdot\frac{\partial\hat{\Phi}}{\partial x}\right) = -\omega^2 I_p\rho\hat{\Phi} \tag{3}$$

$$\hat{\Phi}\left(-\frac{l}{2}\right) = 0,\quad \hat{\Phi}\left(+\frac{l}{2}\right) = 0,\qquad \max\left(\hat{\phi}\right) = 1 \tag{4}$$

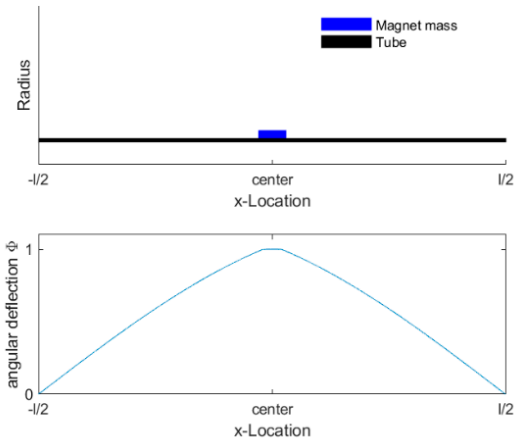

Figure 4. (top) Schematic cross-section of the tubular sensor, including the tube and magnet mass; (bottom) normalized solution of the excited torsional mode over measurement length $\pm l/2$.

Equation (3) is a boundary value problem that could be solved numerically in MATLAB by using the bvp4c (fourth-order method for boundary value problems) function [32]. Thereby, only the solution of the first torsional mode was computed with its corresponding natural frequency, as shown in Figure 4. Due to the inertial load caused by the magnets (blue, Figure 4), the mode was distorted in the central section. This created large local bending of the modal function at the edge where magnets are attached to the tube and results in a slight straightening of the rest of the tube. The time-dependent component of the oscillation is represented by an ordinary differential equation. The representative viscous torque, the moment of inertia, and spring constant were obtained by integration over the length l, see Equations (6) and (7).

The excitation term F was neglected because it was not present when the measurement took place. Thus, the resonator could be modeled by an ordinary differential (Equation (5)) under the assumption of a time-harmonic solution of $(t) = \Re(\hat{X}e^{i\omega t})$:

$$\frac{\partial^2 \varphi}{\partial t^2} J_0 + \varphi \cdot c + \hat{M}_v \hat{X} e^{i\omega t} = 0 \tag{5}$$

$$J_0 = \int_{-l/2}^{l/2} [\rho |\hat{\phi}(x)| \cdot I_p(x)] dx \tag{6}$$

$$\hat{M}_v = \int_{-l/2}^{l/2} \frac{\hat{\tau}(x) 2\pi R^2}{\hat{X}} dx \tag{7}$$

where $\hat{\phi}$, angular deflection; c, mode spring constant; $\hat{X}$, amplitude; $i = \sqrt{-1}$; ω, the angular frequency; and $\hat{M}_v$, fluid-induced torque. Using the time-harmonic assumption, we get Equation (8):

$$-\omega^2 J_0 + c + \hat{M}_v = 0 \tag{8}$$

Equation (8) can be solved as an eigenvalue problem, where the eigenvalue $\lambda = i\omega$. On the basis of the solution, the bandwidth Γ of the resonator can be determined from the logarithmic decrement of the oscillation, which is the real part of the eigenvalue λ. Similarly, the angular resonance frequency ω_0 is the imaginary part of λ.

$$\Gamma = \Re(\lambda) \tag{9}$$

Fluid Forces

The torsional oscillation of the tube created fluid motion, and thus shear stresses at the inner wall of the tube where the fluid is in contact with the solid. These shear stresses τ created a torque, which damped the oscillation. To compute the shear stresses, a simplified set of the linearized Navier–Stokes equation was solved. Flow within the tube was approximated under the assumption of no axial flow, no azimuthal change, and no radial flow. On the basis of these assumptions, a simplified version of the Navier–Stokes equation could be written in cylindrical coordinates, where u, azimuthal velocity; η, dynamic viscosity; ρ, fluid density; r, radius; and p, pressure—see Equations (10) and (11). This approach was already used by Fuchs and Drahm [31] for cylindrical geometries.

$$\frac{\partial u}{\partial t} = \frac{\eta}{\rho}\left(\frac{1}{r}\frac{\partial u}{\partial r} + \frac{\partial^2 u}{\partial r^2} + \frac{u}{r}\right) \tag{10}$$

$$\frac{u^2}{r} = \frac{\partial p}{\partial r} \tag{11}$$

Then, we assumed a time-harmonic solution (Equation (12)).

$$\hat{u}i\omega = \frac{\eta}{\rho}\left(\frac{1}{r}\frac{\partial \hat{u}}{\partial r} + \frac{\partial^2 \hat{u}}{\partial r^2} + \frac{\hat{u}}{r}\right) \tag{12}$$

A solution to Equation (12) could be found (see Equation (14)), where J_1 was the Bessel function of the first kind,Y_1 the Bessel function of the second kind and c_1, c_2 coefficients.

$$\hat{u}(r) = c_1 \cdot \mathrm{J}_1\left((-1)^{\frac{3}{4}} r\sqrt{\frac{\omega\rho}{\eta}}\right) + c_2 \cdot \mathrm{Y}_1\left(-(-1)^{3/4} r\sqrt{\frac{\omega\rho}{\eta}}\right) \tag{13}$$

Boundary conditions were $\hat{u}(r=0) = 0$ and $\hat{u}(r=R) = \hat{v}_0$, where R is the tube inner radius and $\hat{v}_0$ the wall velocity. The wall velocity depended on the axial location, as well as the rate of angular deflection; see Equation (14).

$$\hat{v}_0 = \hat{X} r\omega|\hat{\phi}(x)| \tag{14}$$

The flow field can then be described by Equation (15).

$$\hat{u}(r) = \hat{v}_0 \cdot \frac{\mathrm{J}_1\left((-1)^{\frac{3}{4}} r\sqrt{\frac{\omega\rho}{\eta}}\right)}{\mathrm{J}_1\left((-1)^{\frac{3}{4}} R\sqrt{\frac{\omega\rho}{\eta}}\right)} \tag{15}$$

Figure 5 shows the real part of the azimuthal velocity u for three different viscosities at a constant density of 1000 kg/m^3. For all solutions, flow velocity was near zero within the first 30% of the radius; thus, any flow effects occur in the vicinity of the wall.

On the basis of Equation (15), shear rates and thus the viscous-induced damping could be determined. Viscous-induced torque $\hat{M}_v$ was computed by integrating shear stress $\hat{\tau}$ over the wall of the tube; see Equation (7). Shear stress was defined by Equation (16) at the radius of the inner wall R.

$$\hat{\tau}(x) = \eta\left(\frac{\partial \hat{u}\left(\hat{v}_0(x)\right)}{\partial r} - \frac{\hat{u}\left(\hat{v}_0(x)\right)}{r}\right) \tag{16}$$

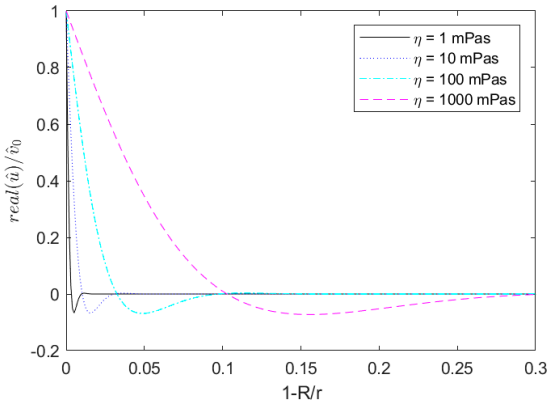

Figure 5. Velocity profile for different fluids in a tubular sensor with a frequency of 10,800 Hz and density of 1000 kg/m^3.

3. Discussion

The sensor was tested in two different stages. In the first stage, static experiments were conducted under well-defined conditions where the fluid properties were well known. These experiments were used to create a baseline for the sensor and validate the numerical model. The numerical model was then fitted to the experiments to account for any systematic deviation. The fitting was carried out by multiplying the prediction with an empirical correction function. This corrected prediction was then used to predict the fluid's viscosity based on the measured properties. In the second stage, sensor sensitivity towards internal flow was evaluated by comparing the measured damping for the same fluids with and without internal flow.

3.1. Static Flow Conditions

Experiments were conducted under static, thermally uniform conditions using fluids with a well-known property. The measured fluid-induced damping versus the product of fluid denisty and viscosity (ρη) is shown in Figure 6. The colormap shows the temperature at which the measurement was conducted. To mitigate any temperature effects, the measured bandwidth was divided by the resonance frequency. This was carried out because the shear modulus of the resonator was temperature dependent. The resonance frequency and bandwidth of the sensor decreases with increasing temperature. By dividing the bandwidth by the resonance frequency, the temperature dependence of the damping could be compensated, and the measurements collapsed to a single line. Thus, the sensor measures the same Γ/f_0 value independent of fluid temperature, as can be seen in Figure 6.

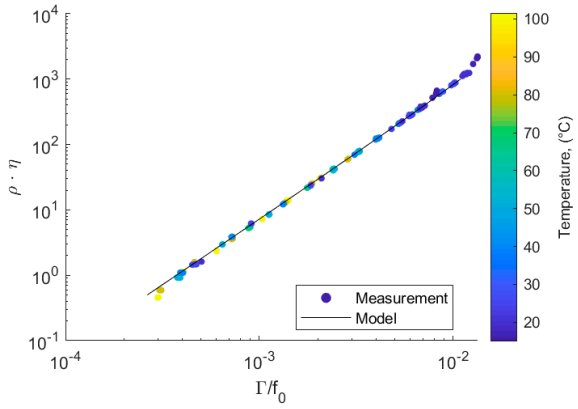

Figure 6. Numerical prediction and experimental measurements of the ρη value at different temperatures, where ρ is the density and η the viscosity.

The model described in Section 2.4 enables the prediction of the $\rho\eta$ value, where ρ is the fluid density and η the dynamic viscosity. This prediction of the $\rho\eta$ value for a given damping is shown as a black line in Figure 6 (black line). The predictions were within the same order of magnitude and show the same trend as the experimental measurements. This indicates that the model captured the primary effects of the resonator. For small viscosities, the model predicted that damping increases proportionally to the square root of $\rho\eta$, which is a typical property of sensors based on torsional resonators. This is the case, as long as the penetration depth $\delta = \sqrt{2\eta/(\rho)}$ is much smaller than the inner radius from the tube (2.625 mm). The penetration depth δ ranges from 0.054 mm at a dynamic viscosity of 1 mPas up to 0.171 mm for a viscosity of 1000 mPas. Thus, at higher viscosities, the curvature of the tube becomes relevant and the predicted damping relatively decreases. This effect is present in both simulation and experiment, but more predominant in the experiments.

The deviation between measurement and model is more evident in Figure 7. Despite the overall trend being in good agreement, predictions systematically differed for high $\rho\eta$ values. At low $\rho\eta$ values, there was a constant offset between numerical predictions and experiments, which could be explained by manufacturing tolerances. However, at high $\rho\eta$ values, i.e., high damping, there was systematic deviation in the trend. This systematic deviation was statistically significant and could be caused by an effect that was neglected in the model. Potential sources of the deviation include

(1) Bias in the damping measurement: At high damping, the signal-to-noise ratio (SNR) decreased due to the smaller amplitude of the resonator. The algorithm used to determine the damping was sensitive to the noise in the signal. As the SNR decreased, the error in the evaluation of the damping value increased. The error is not normally distributed but had a bias towards smaller damping values. Hence, the evaluated averaged value of the damping tended to be underpredicted as the SNR decreased. This behavior could be qualitatively simulated and showed a similar trend, as was experimentally observed.

(2) Distortion of modal function: Another potential source of the systematic deviation is the fluid–structure interactions. At high $\rho\eta$ values, the fluid exerts forces on the tube that are much higher than those exerted at low $\rho\eta$ values; thus, the balance between structural and fluid forces changes. In the model, the modal shape was computed under the assumption that the fluid forces did not impact the shape of the mode. Hence, this assumption may no longer be valid for fluids with high $\rho\eta$ values. To account for and verify this effect, the fluid–structure interaction (strong coupling) will be incorporated into the numerical model in future studies. This would allow specific investigation of the impact of fluid properties on the structural mode and its implications at $\rho\eta$ values.

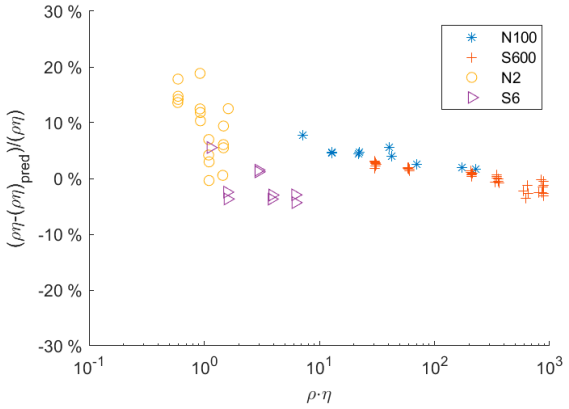

Figure 7. Relative deviation of the predicted and actual $\rho\eta$ value, where ρ is the density and η the dynamic viscosity.

To account for those effects which were not accounted for in the numerical prediction, an empirical polynomial model was used to correct the deviation between the predicted and measured values; see Equation (17). This polynomial was multiplied by the numerical prediction to correct the

small deviations between the numerical prediction and experimental data. The multiplier function was a polynomial based on the log of the $\rho\eta$ value. Coefficients were determined by the least squares method on the relative deviation from prediction to measurement (Equation (18)).

$$\frac{\Gamma}{f_0} \approx \frac{\Gamma_{num}(\rho\eta)}{f_{0,num}} \cdot \sum_{i=0}^{4} a_i \log(\rho\eta)^i \tag{17}$$

$$a_i := \min\left(\sum \left[\frac{\frac{\Gamma_{num}(\rho\eta)}{f_{0,num}} \cdot \sum_{i=0}^{4} a_i \, log(\rho\eta)^i - \frac{\Gamma}{f_0}}{\frac{\Gamma_{num}(\rho\eta)}{f_{0,num}} \cdot \sum_{i=0}^{4} a_i \, log(\rho\eta)^i} \right]^2 \right) \tag{18}$$

To validate the baseline model, we tested it against two other viscosity reference fluids from Cannon, S20 and S200, which were not used to create a baseline for the sensor, i.e., to determine coefficient a_i. Therefore, the measured damping was used to determine the ρη value of the fluid (using Equation (17)). This predicted ρη value was then compared to the actual ρη value of the fluid used in the measurement. Figure 8 shows the relative deviation between the predicted (Equation (17)) and actual ρη value of the fluid. Deviation from the predicted to the actual ρη value was within the confidence interval. The black line indicates the 95% confidence interval in terms of repeatability, whereas the red line shows the respective 95% confidence level for predicting the absolute ρη value. The uncertainty of predicting the absolute ρη value was higher because it also contained the uncertainty of the basic calibration conducted in this study.

Overall, confidence intervals become smaller at higher ρη values and reach a minimum of ±4% for repeatability.

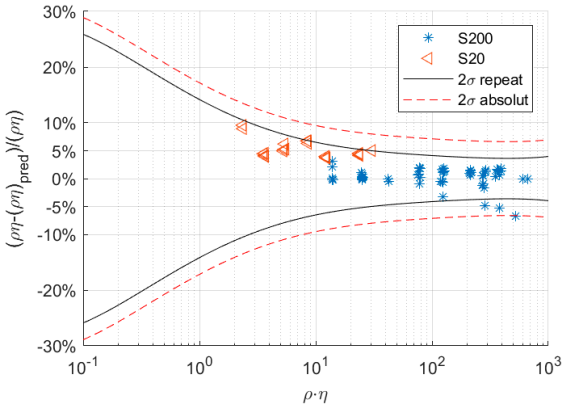

Figure 8. Relative deviation of the predicted and actual ρη value for the fluids S20 and S200, where ρ is the density and η is the dynamic viscosity. The full and dashed lines show the 95% confidence interval (2σ) for repeatability and absolute value, respectively.

3.2. Flow Loop

The sensor was tested in a flow loop to account for flow effects such as turbulent or laminar flow. This experiment was necessary to investigate the interaction between internal flow and flow induced by torsional vibration. This is important under turbulent conditions, where turbulences may interact and disturb the flow caused by the torsional vibration of the sensor and thus impact the measurement. This would create a flow or Reynolds dependence on the measurement. Experiments were conducted over a wide range of Reynolds numbers from 500 (laminar flow) up to fully turbulent conditions at 50,000. The variation in the Reynolds number was achieved by varying both flow rate and the fluid's viscosity (by changing the glycerol concentration in water).

Figure 9 shows the relative deviation of the predicted ρη value between static flow measurement and measurements with the internal flow. All deviations were below ±1%. This deviation was below

the confidence interval of repeatability, and data were randomly spread. Hence, flow conditions shown in Figure 9 exhibited no significant influence on measurements of Reynolds numbers up to 50,000. Any variations were within the uncertainty of repeatability.

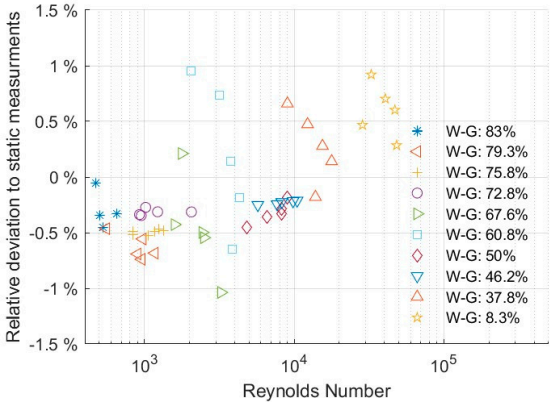

Figure 9. Relative deviation between static and flow measurements in a flow loop for different water–glycerol (W-G) concentrations.

4. Conclusions

We presented an experimentally validated numerical model for a nonintrusive, real-time, tubular sensor and tested for different viscosities and densities. The sensor was comprised of a straight tube and could be directly integrated into a piping system. The numerical model describing the sensor was derived on the basis of the torsional vibration of the tube and the interaction with the fluid inside the tube. The fluid interaction with the resonator was computed using an analytical fluid model. The modelled predictions were compared with four different fluids at temperatures between 20 and 100 °C and were found to be in good agreement at low viscosities. However, at high viscosities, there was systematic deviation between numerical prediction and experimental data. This deviation was likely caused by fluid-induced modal distortion or bias in the measurement error.

In order to account for the systematic deviation between prediction and measurement, the numerical prediction was multiplied with an empirical model. After this correction, the model was tested against two additional fluids. Measurements were in good agreement with the prediction and within the confidence interval.

Additionally, the tubular sensor was tested in a flow loop with different water–glycerol solutions, simulating industrial conditions, in a Reynolds number range of 500–50,000. The sensor did not exhibit any Reynolds dependence. Overall, the tubular sensor showed good potential for application in industrial processes. However, further studies are needed to elucidate the departure of the model prediction from real sensor behavior at high viscosities.

Author Contributions: Sensor conceptualization, K.H. and J.G.; design and build methodology, D.B. and J.G.; numerical modeling, D.B.; model validation, D.B. and J.G.; data analysis, D.B.; analysis, D.B., J.G. and K.H.; resources, S.K. and G.B.; writing—original draft preparation, D.B.; writing—review and editing, D.B., H.K., J.G., and S.K.; visualization, D.B.; supervision, G.B. and H.A.K.; project administration, G.B. and S.K.; funding acquisition, G.B. and S.K. All authors have read and agreed to the published version of the manuscript.

Funding: This research was partially funded by Innosuisse, grant number 27254.1.

Acknowledgments: The authors would like to thank Josquin Rosset and Patrick Vogler for their support with the electronics of the sensor and Vijoya Sa and Patrick Vogler for their support with the experiments.

Conflicts of Interest: The authors declare no conflict of interest.

References

1. Papi, M.; Maulucci, G.; Arcovito, G.; Paoletti, P.; Vassalli, M.; De Spirito, M. Detection of Microviscosity by Using Uncalibrated Atomic Force Microscopy Cantilevers. *Appl. Phys. Lett.* **2008**, *93*, 4102. doi: 10.1063/1.2970963.
2. Ghatkesar, M.K.; Braun, T.; Barwich, V.; Ramseyer, J. P.; Gerber, C.; Hegner, M.; Lang, H. P. Resonating Modes of Vibrating Microcantilevers in Liquid. *Appl. Phys. Lett.* **2008**, *92*, 10–13, doi:10.1063/1.2838295.
3. Papi, M.; Arcovito, G.; De Spirito, M.; Vassalli, M.; Tiribilli, B. Fluid viscosity determination by means of uncalibrated atomic force microscopy cantilevers. *Appl. Phys. Lett.* **2006**, *88*, 194102, doi:10.1063/1.2200588.
4. Shih, W.Y.; Li, X.; Gu, H.; Shih, W.-H.; Aksay, I.A. Simultaneous liquid viscosity and density determination with piezoelectric unimorph cantilevers. *J. Appl. Phys.* **2001**, *89*, 1497–1505, doi:10.1063/1.1287606.
5. McLoughlin, N.; Lee, S.; HaḥnerG. Simultaneous determination of density and viscosity of liquids based on resonance curves of uncalibrated microcantilevers. *Appl. Phys. Lett.* **2006**, *89*, 184106, doi:10.1063/1.2374867.
6. Thompson, M.; Kipling, A.L.; Duncan-Hewitt, W.C.; Rajakovi?, L.V.; Avi-Vlasak, B.A.; Rajaković, L.V.; Cavic-Vlasak, B.A. Thickness-shear-mode acoustic wave sensors in the liquid phase. A review. *Analyst* **1991**, *116*, 881–890, doi:10.1039/an9911600881.
7. Tessier, L.; Patat, F.; Schmitt, N.; Feuillard, G.; Thompson, M. Effect of the Generation of Compressional Waves on the Response of the Thickness-Shear Mode Acoustic Wave Sensor in Liquids. *Anal. Chem.* **1994**, *66*, 3569–3574, doi:10.1021/ac00093a006
8. Keiji Kanazawa, K.; Gordon, J.G. The Oscillation Frequency of a Quartz Resonator in Contact with Liquid. *Anal. Chim. Acta* **1985**, *175*, 99–105, doi:10.1016/S0003-2670(00)82721-X.
9. Huang, L.; Chen, J.; Cao, T.; Cong, H.; Cao, W. Investigation of Microtribological Properties of C60-Containing Polymer Thin Films Using AFM/FFM. *Wear* **2003**, *255*, 826–831, doi:10.1016/S0043-1648(03)00359-4.
10. Kim, S.; Lee, D.; Yun, M.; Jung, N.; Jeon, S.; Thundat, T. Multi-Modal Characterization of Nanogram Amounts of a Photosensitive Polymer. *Appl. Phys. Lett.* **2013**, *102*, 2–6, doi:10.1063/1.4788740.
11. Bistac, S.; Schmitt, M.; Ghorbal, A.; Gnecco, E.; Meyer, E. Nano-Scale Friction of Polystyrene in Air and in Vacuum. *Polymer* **2008**, *49*, 3780–3784, doi:10.1016/j.polymer.2008.06.032.
12. Martin, F.; Newton, M.I.; McHale, G.; Melzak, K.A.; Gizeli, E. Pulse Mode Shear Horizontal-Surface Acoustic Wave (SH-SAW) System for Liquid Based Sensing Applications. *Biosens. Bioelectron* **2004**, *19*, 627–632, doi:10.1016/S0956-5663(03)00257-4.
13. Voinova, M.V.; Rodahl, M.; Jonson, M.; Kasemo, B. Viscoelastic Acoustic Response of Layered Polymer Films at Fluid-Solid Interfaces: Continuum Mechanics Approach. *Phys. Scripta.* **1998**, *59*, 391–396, doi:10.1238/Physica.Regular.059a00391.
14. Lucklum, R.; Behling, C.; Cernosek, R.W.; Martin, S.J. Determination of Complex Shear Modulus with Thickness Shear Mode Resonators. *J. Phys. D. Appl. Phys.*, **1997**, *30*, 346–356, doi:10.1088/0022-3727/30/3/006.
15. Xie, J.; Hu, Y. A Two-Dimensional Model on the Coupling Thickness-Shear Vibrations of a Quartz Crystal Resonator Loaded by an Array Spherical-Cap Viscoelastic Material Units. *Ultrasonics* **2016**, *71*, 194–198, doi: 10.1016/j.ultras.2016.05.026.
16. Dohn, S.; Hansen, O.; Boisen, A. Cantilever Based Mass Sensor with Hard Contact Readout. *Appl. Phys. Lett.* **2006**, *88*, 1–4, doi:10.1063/1.2217161.
17. Lang, H.P.; Hegner, M.; Gerber, C. Cantilever Array Sensors. *Nanobiotechnology II More Concepts Appl.* **2007**, *8*, 175–195, doi:10.1002/9783527610389.ch10.
18. Datar, R.; Passian, A.; Desikan, R.; Thundat, T. Microcantilever Biosensors. *Proc. IEEE Sens.* **2007**, *37*, 5, doi:10.1109/ICSENS.2007.4388320.
19. Stachiv, I.; Fedorchenko, A.I.; Chen, Y.-L. Mass Detection by Means of the Vibrating Nanomechanical Resonators. *Appl. Phys. Lett.* **2012**, *100*, 093110, doi:10.1063/1.3691195.
20. Qin, L.; Cheng, H.; Li, J.M.; Wang, Q.M. Characterization of Polymer Nanocomposite Films Using Quartz Thickness Shear Mode (TSM) Acoustic Wave Sensor. *Sens. Actuators A Phys.* **2007**, *136*, 111–117, doi:10.1016/j.sna.2006.12.027.
21. Brack, T. Multi-Frequency Phase Control of a Torsional Oscillator for Applications in Dynamic Fluid Sensing. ETH Zurich, PhD. Thesis, Zurich, Swizerland, 2017.
22. Brack, T.; Dual, J. Multimodal torsional vibrations for the characterization of complex fluids. In *WIT Transactions on the Built Environment*; Computational Mechanics WIT Press, Southampton, UK: 2013; Volume 129, pp. 191–199, doi:10.2495/FSI130171.

23. Brack, T.; Bolisetty, S.; Dual, J. Simultaneous and Continuous Measurement of Shear Elasticity and Viscosity of Liquids at Multiple Discrete Frequencies. *Rheol. Acta* **2018**, *57*, 415–428, doi:10.1007/s00397-018-1083-y.
24. Valtorta, D.; Mazza, E. Dynamic Measurement of Soft Tissue Viscoelastic Properties with a Torsional Resonator Device. *Med. Image Anal.* **2005**, *9*, 481–490, doi:10.1016/j.media.2005.05.002.
25. Dual, J. Experimental Methods in Wave Propagationin Solids and Dynamic Viscometry. ETH Zurich, PhD. Thesis, Zurich, Swizerland, 1989.
26. Reinhart, W.H.; Hausler, K.; Schaller, P.; Erhart, S.; Stetter, M.; Dual, J.; Sayir, M. Rheological Properties of Blood as Assessed with a Newly Designed Oscillating Viscometer. *Clin. Hemorheol Microcirc*. **1998**, *18*, 59–65.
27. Brunner, D.; Khawaja, H.; Moatamedi, M.; Boiger, G. CFD modelling of pressure and shear rate in torsionally vibrating structures using ANSYS CFX and COMSOL multiphysics. *Int. J. Multiphysics* **2018**, *12*, 349–358.
28. Clara, S.; Feichtinger, F.; Voglhuber-Brunnmaier, T.; Niedermayer, A. O.; Tröls, A.; Jakoby, B. Balanced Torsionally Oscillating Pipe Used as a Viscosity Sensor. *Meas. Sci. Technol.* **2019**, *30*, doi:10.1088/1361-6501/aae755.
29. Clara, S.; Antlinger, H.; Feichtinger, F.; Niedermayer, A.O.; Voglhuber-Brunnmaier, T.; Jakoby, B. A balanced flow-through viscosity sensor based on a torsionally resonating pipe. *Proc. IEEE Sens.* **2017**, 1–3, doi:10.1109/ICSENS.2017.8234137.
30. Häusler, K.; Reinhart, W.H.; Schaller, P.; Dual, J.; Goodbread, J.; Sayir, M. A newly designed oscillating viscometer for blood viscosity measurements. *Biorheology* **1996**, *33*, 397–404, doi:10.1016/0006-355X(96)00030-3.
31. Fuchs, M.; Drahm, W.; Matt, C.; Wenger, A. A coriolis meter with direct viscosity measurement. *Comput. Control. Eng. J.* **2003**, *14*, 42–43.
32. Kierzenka, J.; Shampine, L.F. A BVP solver based on residual control and the maltab PSE. *ACM Trans. Math. Softw.* **2001**, *27*, 299–316. doi:10.1145/502800.502801.